

63 3. 3

ASD-TDR-62-411

Part II

403369

ASTIA

CATWING
A-1

ELECTRODELESS MHD GENERATOR RESEARCH

Part II: Laboratory Facility and Experimental Results

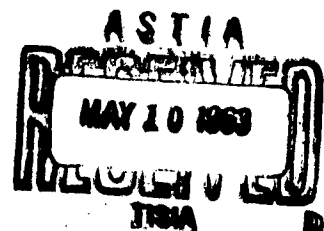
TECHNICAL DOCUMENTARY REPORT NO. ASD-TDR-62-411, Pt. II

March 1963

Directorate of Aeromechanics
Aeronautical Systems Division
Air Force Systems Command
Wright-Patterson Air Force Base, Ohio

Project 8173, Task 817306-7

(Prepared under Contract No. AF 33(616)-7913
by the Radio Corporation of America
Defense Electronic Products,
Missile and Surface Radar
Division, Moorestown, N.J.)



~~CONFIDENTIAL~~

NOTICES

When Government drawings, specifications, or other data are used for any purpose other than in connection with a definitely related Government procurement operation, the United States Government thereby incurs no responsibility nor any obligation whatsoever; and the fact that the Government may have formulated, furnished, or in any way supplied the said drawings, specifications, or other data, is not to be regarded by implication or otherwise as in any manner licensing the holder or any other person or corporation, or conveying any rights or permission to manufacture, use, or sell any patented invention that may in any way be related thereto.

ASTIA release to OTS not authorized.

Qualified requesters may obtain copies of this report from the Armed Services Technical Information Agency, (ASTIA), Arlington Hall Station, Arlington 12, Virginia.

Copies of this report should not be returned to the Aeronautical Systems Division unless return is required by security considerations, contractual obligations, or notice on a specific document.

FOREWORD

This report contains a description of the experimental laboratory facility developed for this program and results of the experimental model testing performed under this investigation. This work was performed during the period April 26, 1961 through January 31, 1963 by the Missile and Surface Radar Division of the Radio Corporation of America under Air Force Contract AF 33(616)-7913. Technical direction of this project was administered by the Directorate of Aeromechanics, Deputy for Technology, Aeronautical Systems Division (ASD), under the supervision of Mr. D. Warnock of the Flight Vehicle Power Branch, Flight Accessories Laboratory, ASD.

The following personnel of RCA participated in this work: J. F. Delany, J. B. Fanucci, C. A. Nittrouer, H. C. Petty and N. Sands.

The authors wish to acknowledge the contributions made to this program in the development of equipment for the experimental laboratory facilities by E. M. Groman, W. C. Prenskey, P. Pressel, and H. Zimmerman for engineering design and development; A. R. Acerbo, J. B. Powell and D. T. Zadorozny for technical assistance in experimental equipment development and test operations.

A very major contribution was made during the important final phase of the testing program by Dr. K. Fischbeck of RCA, Princeton, N.J. and Dr. W. Jackson, a consultant from the Massachusetts Institute of Technology.

ABSTRACT

PART II

Problem - To experimentally determine the feasibility of A. C. Electrodeless Magnetohydrodynamic Power Generation, utilizing a model generator.

Scope of Investigation - The analysis, development and test model operation involved the design, construction and testing of the component units which comprise the plasma arc laboratory facility. This report includes the following areas: The laboratory facilities provided for the conduction of the experimental investigation included Plasma Arc Torch, Vacuum System, Cooling System, Gas Supply System, Power Supply for Plasma Arc Torch, and Primary Power Requirements including Substation; and the design of the generator test model involved Plenum and Mixing Chamber, Seeder, Supersonic Nozzle, Test Section, Diffuser, Power Extraction Coils, Coil Power Supply, Phase Nulling Network, and other instrumentation. The design of the experimental generator was a result of the theoretical studies described in Part I.

Results of the Experimental Investigation - Electrodeless A. C. MHD power generation has been experimentally observed, and extracted power from the plasma has been recorded during the test operation of the model.

PUBLICATION REVIEW

The publication of this report does not constitute approval by the Air Force of the findings or conclusions contained herein. It is published for the exchange and stimulation of ideas.

TABLE OF CONTENTS

	<u>Page</u>
1. <u>INTRODUCTION</u>	1.
1.1 Objective of Experimental Investigation.....	1.
1.2 Problem Background.....	1.
1.3 Scope of Experimental Facility and Investigation.....	2.
2. <u>MHD EXPERIMENTAL LABORATORY FACILITY</u>	4.
2.1 Introduction.....	4.
2.2 Plasma Arc Torch System.....	4.
2.2.1 Arc Torch.....	4.
2.2.2 Plasma Arc Starter.....	8.
2.2.3 Control Console.....	9.
2.3 Power Supply.....	11.
2.4 Power Substation.....	11.
2.5 Vacuum System.....	14.
2.6 Cooling System.....	14.
2.7 Generator-Torch and Components.....	14.
2.7.1 Plenum and Mixing Chamber.....	19.
2.7.2 Supersonic Nozzle.....	19.
2.7.3 Test Section.....	19.
2.7.4 Diffuser.....	19.
2.7.5 Power Extraction Coils.....	19.
2.7.6 Coil Power Supply.....	20.
2.7.7 Power Monitoring Matrix.....	20.
2.7.8 Positive Feed Seeder.....	20.

	<u>Page</u>
2.7.9 Instrumentation.....	20.
3. <u>AERODYNAMIC DESIGN OF GENERATOR</u>	23.
3.1 Introduction.....	23.
3.2 Nozzle Design and Performance.....	24.
3.2.1 Design of Supersonic Nozzle by Method of Characteristics.....	24.
3.2.2 Allowance for Boundary Layer Growth.....	28.
3.2.3 Flow Parameters in the "Plenum Chamber", Throat and Nozzle Exit, Including Considerations of Real Gas Effects.....	30.
3.2.4 Perturbation of Nozzle Exit Parameters.....	32.
3.2.5 Power Requirements (Ideal Case).....	35.
3.2.6 Subsonic Part of Nozzle.....	40.
3.3 Test Section.....	40.
3.4 Supersonic Diffuser.....	47.
4. <u>ELECTRICAL DESIGN OF GENERATOR</u>	51.
4.1 Introduction.....	51.
4.2 Transistorized Exciter.....	52.
4.2.1 General Discussion.....	52.
4.2.2 Clock Pulse Generator.....	52.
4.2.3 Square Wave Generator.....	55.
4.2.4 Control of Power Output - Guard Bands.....	56.
4.2.5 Final Power Output Stage.....	57.
4.2.6 Circuit Performance.....	57.
4.2.7 System Problem.....	57.

	<u>Page</u>
4.3 Alternator Power Supply.....	58
4.3.1 General Requirements.....	58
4.3.2 Motor.....	58
4.3.3 Alternators.....	58
4.4 Interaction Coil System.....	59
4.4.1 General Remarks.....	59
4.4.2 Construction.....	60
4.4.3 Cooling.....	60
4.4.4 Operation.....	62
4.4.5 Instrumentation Facilities.....	62
5. <u>MECHANICAL DESIGN OF GENERATOR</u>	63
5.1 Introduction.....	63
5.2 Motor/Alternator Set for Three Phase Coil Power.....	63
5.3 Cooling Water System.....	64
5.4 Vacuum Dump System.....	65
5.5 Gas Supply System.....	65
5.6 Test Section.....	66
6. <u>INSTRUMENTATION</u>	67
6.1 Introduction.....	67
6.2 Recorded Test Data.....	67
6.2.1 Electrical Measurements.....	67
6.2.2 Manometric Measurements.....	68
6.3 Stagnation Enthalpy Measurements.....	68
6.3.1 Introduction.....	68
6.3.2 Theoretical Heat Transfer Rate to Calorimeter.....	69

	<u>Page</u>
6.3.3 Stagnation Enthalpy Probe.....	70
6.3.4 Sample Computation of Stagnation Enthalpy.....	73
6.3.5 Total Enthalpy of a Perfect Gas in Isentropic Flow.....	76
6.4 Pressure Measurements.....	77
6.5 Power Monitoring Matrix.....	78
6.5.1 General Discussion.....	78
6.5.2 Theoretical Considerations.....	78
6.5.3 Construction.....	81
6.5.4 Adjustment.....	81
6.6 Field Strength Measurements.....	81
7. <u>EXPERIMENTAL RESULTS</u>	84
7.1 Introduction.....	84
7.2 Modification of Electrical Instrumentation.....	84
7.3 Electrical Results.....	87
7.4 Aerodynamic Results.....	92
8. <u>CONCLUDING REMARKS</u>	98
9. <u>RECOMMENDATIONS</u>	98
<u>APPENDIX I</u>	100
<u>REFERENCES</u>	101
<u>SYMBOLS</u>	103
TABLE I.....	108
TABLE II.....	109

LIST OF FIGURES

<u>NUMBER</u>	<u>TITLE</u>
1	Schematic Diagram of Plasma Arc Facility.
2	Plasma Arc Torch System.
3	Plasma Arc Torch and Components.
4	View of Control Console, Cooling Water Flow Meters, and N ₂ Gas Surge Cylinders.
5	1 Megawatt DC Power Supply - View of Saturable Reactors, Magnetic Amplifier, and Power Transformers.
6	26/4 KV Power Substation.
7	Vacuum Dump Tank.
8	Cooling Water Surge Tank & Pump, and Vacuum Pump.
9	Schematic Diagram of Equipment Cooling System.
10	Power Extraction Coils Installed on Test Section.
11	Three-Phase Motor/Alternator, Coil Supply Set.
12	Derivation of Nozzle's Contour by Method of Characteristics.
13	Velocity at Exit of Nozzle as Affected by Stagnation Pressure and Enthalpy.
14	Static Temperature at Exit of Nozzle as Affected by Stagnation Pressure and Enthalpy.
15	Static Pressure at Exit of Nozzle as Affected by Stagnation Pressure and Enthalpy.
16	Static Density at Exit of Nozzle as Affected by Stagnation Pressure and Enthalpy.
17	Mass Flow Rate as Affected by Stagnation Pressure and Enthalpy.

18	Power Required to Increase Enthalpy from 127 BTU/LB (Standard Atmospheric Air) to Stagnation Value ---
19	Perspective View - Plenum Chamber Blending into Diverging Nozzle.
20	Contouring of Subsonic Part of Nozzle.
21	Transite "Test Sections" Used in Experiments.
22	Temperature Distribution in a Semi-Infinite Slab of Quartz.
23	Inside Dimensions of Diffuser.
24	Block Diagram - Transistorized 3-Phase Generator.
25	Block Diagram - Typical Transistorized Power Amplifier and Waveforms.
26	Schematic Diagram of Interaction Coil System.
27	Perspective Cut-Away View of Stagnation Enthalpy Probe Assembly.
28	Calorimeter-Type Stagnation Enthalpy Probe.
29	Phasor Diagram - Phase I of Power Monitor Matrix.
30	Field Strength Measurements Along Interaction Channel.
31	Circuit Diagram - Final Instrumentation System.
32	Vector Diagrams - Voltage and Current.
33	Electrical Measurements from Motion Picture Film Data - Run #13.
34	Electrical Measurements from Motion Picture Film Data - Run #15.
35	Typical 16 mm Motion Picture - Recorded Test Data.
36	Aerodynamic Measurements from Motion Picture Film Data-Run #13.
37	Aerodynamic Measurements from Motion Picture Film Data-Run #14.

1. INTRODUCTION

1.1 Objective of the Experimental Investigation

The purpose of this laboratory program was to investigate the parameters involved in the generation of A.C. magnetohydrodynamic (MHD) power, by means of an experimental model facility. The model itself is a traveling wave type A.C. MHD induction generator. The facility design and subsequent experimental testing program are discussed in this report. Among the major items considered are extraction of power from an ionized plasma, the effects on extracted power from the plasma resulting from variations in plasma conductivity with and without alkali metal "seeding", experimental determination of extracted power by pressure differential measurements across the interaction channel, and other similar investigations.

1.2 Problem Background

Direct conversion of the thermal and kinetic energy of a hot, electrically conductive gas into electrical energy has been discussed in Part I of this report. In principle, the experimental model configuration developed for this program follows that previously described (Reference 1). Since this is a model generator, certain inherent problems must be emphasized since they are peculiar to model operation and are a direct result of necessary scalar restraints. Detection of the comparatively small amount of extracted power in the presence of an excitation power which is larger by several orders of magnitude, presented a rather formidable detection and instrumentation problem.

The physical design parameters involved in the interaction coil system represented, along with its associated equipment, a considerable problem area.

Manuscript released by the authors 31 January 1963 for publication as an ASD Technical Documentary Report.

Aerodynamic considerations leading to the mechanical design relative to electrical requirements of the plasma arc torch, plenum chamber, supersonic nozzle, test section and diffuser, in a like manner are presented in this report representing some of the major problem areas associated with the design and testing of this model generator.

1.3 Scope of Experimental Facility and Investigation

Areas representing major design and experimental investigative effort are presented in individual sections. The contents of each section and their interdependence are briefly discussed in the paragraphs which follow.

In Section 2, the major items which were developed for this program are described relative to their performance capabilities required for the experimental investigations conducted under this project. It has been determined that the equipment has provided the means to demonstrate the feasibility of electrodeless A.C. MHD power from this model generator.

The theoretical analysis and aerodynamic design considerations, involving the various parameters investigated for the generator nozzle design and performance characteristics are discussed in Section 3. The design of the supersonic and subsonic portion of the nozzle, test section, diffuser and idealized power requirements are considered in relation to performance requirements.

In Section 4, the areas of major electrical design effort are discussed relative to the requirements of the interaction coil system.

The area of major mechanical equipment design effort is discussed in Section 5. This includes the description of the motor/alternator set for the coil power supply, cooling and vacuum systems, and various test sectional configuration designs.

Instrumentation developed or provided for experimental test operation of the

model generator are discussed in Section 6. A power monitoring matrix (phase nulling network) has been constructed to eliminate the large power component incident upon the coils in order to present only that power which is extracted from the plasma. The stagnation enthalpy probe and general experimental instrumentation are also described in this section. Heat balance as well as pressure measurements and the special total enthalpy probe which was developed for this program are also described in Section 6.

The experimental results obtained are described from the standpoints of aerodynamic and electrical values in Section 7.

2. MHD EXPERIMENTAL LABORATORY FACILITY

2.1 Introduction

In order to perform the experimental portion of this investigation, an extensive company-sponsored laboratory facility was implemented for this project, which is shown in schematic form by Figure 1. The laboratory is physically located in the Advanced Techniques Development building at the Moorestown, New Jersey plant. The major components which constitute this facility are described in the following sub-sections.

2.2 Plasma Arc Torch System

The one megawatt D.C. arc torch and its associated components (Figure 2) are the means used to produce the plasma from which power is extracted by the model electrodeless A.C. MHD generator. In this experiment, the plasma is a high temperature (8800°R), partially ionized gas, constituted to simulate air heated by the combustion of fossil fuels under atmospheric conditions.

2.2.1 Arc Torch

The arc torch is sufficiently flexible in operation to permit the use of several combinations of gases at variable flow rates and pressures, and to produce plasmas of selectable enthalpies (Figure 3). The torch is constructed of non-ferrous material (brass and copper with exterior housings of fiberglass). All expendable portions of this unit (anodes, cathodes, gas and water seals) which are gradually destroyed by continued use are field replaceable. The plasma arc is stabilized by an internal cathode/anode gas sheath. The torch is water cooled.

The torch is operable at a power level of 1000 KW continuously on nitrogen, at one atmosphere chamber pressure (15 psia) with a variable exit enthalpy between 2000 and 8000 BTU per pound. The power level is variable between 50 and 1000 KW. Plasma contamination by heavy metal vapor under those conditions is less than

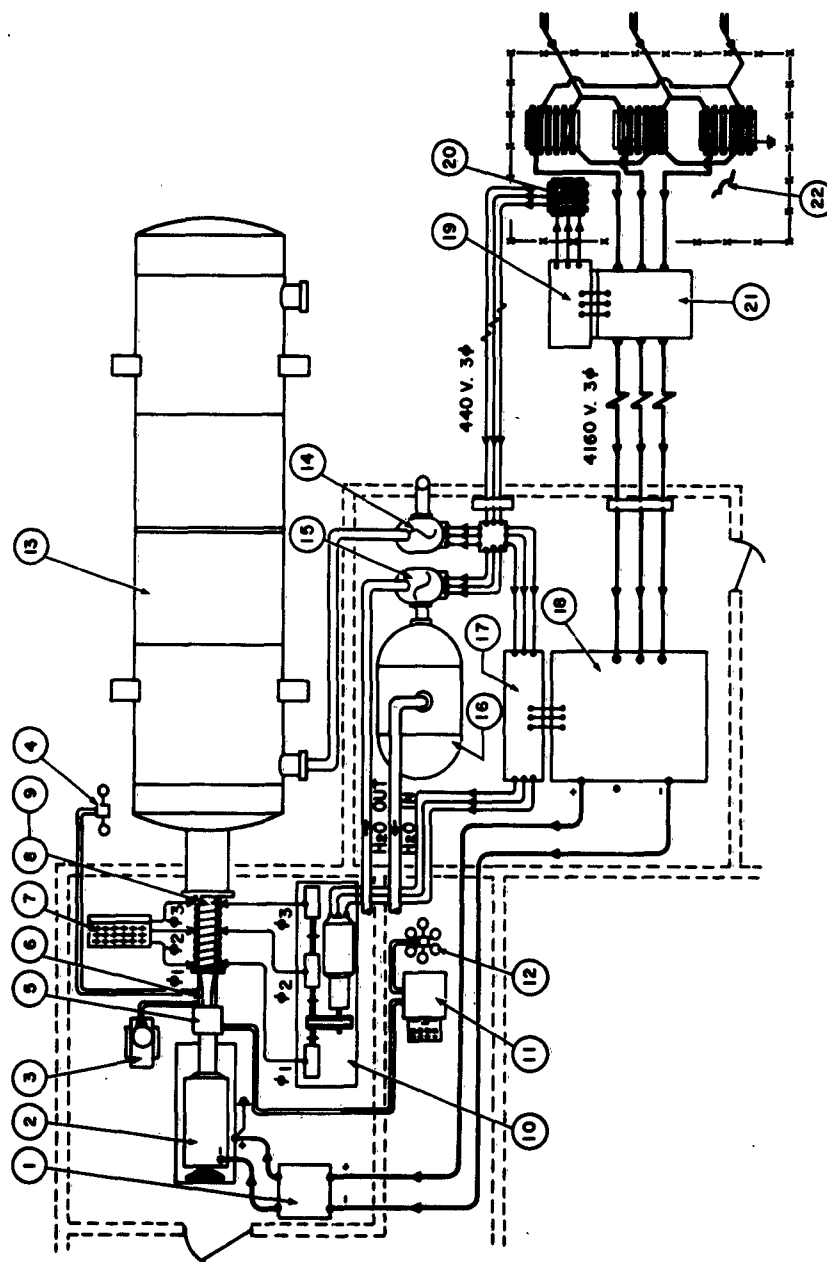


Figure 1. Schematic Diagram of Plasma ARC Facility



Figure 2. Plasma ARC Torch System



Figure 3. Plasma ARC Torch and Components

0.3% by weight. It is capable of operation for two minutes in any four-hour period in air, under the same conditions, except that contamination by heavy metal vapor may rise by a factor of three. The operating efficiency of the torch under the conditions described (2000 amps and 500 volts) is no less than 60%.

By changing electrodes, the torch is capable of operation on the gases listed below, with gas supply pressures at 300 psia, to produce maximum operating conditions as follows:

<u>GAS</u>	<u>PRESSURE</u>	<u>ENTHALPY</u>
<u>Helium</u>	1 atmosphere	- 40,000 BTU/lb.
	20 atmospheres	- 3,000 BTU/lb.
<u>Argon</u>	1 atmosphere	- 10,000 BTU/lb.
	20 atmospheres	- 1,000 BTU/lb.
<u>Nitrogen or Air</u>	1 atmosphere	- variable 2000 to 8000 BTU/lb.
	20 atmospheres	- 4,000 BTU/lb.

An integral mounting base on the torch provides simple, single connections for the electrical service, with power handling capabilities up to 2000 volts and 8000 amperes. Connections are provided for plasma gas, cooling water inlets and outlets, and plasma mixing gas. Water-cooling service is provided for the plenum chamber and supersonic nozzle. The assembly is semi-portable.

2.2.2 Plasma Arc Starter

An arc ignitor or starter was constructed and is of basically a standard welding-type spark gap machine design (Figure 3). It has a series connection to the D.C. power line, through a high current induction coil, and is energized from the control console.

2.2.3 Control Console

The control console houses all control and monitoring functions of the torch as well as those for the one megawatt power supply (Figure 4). Calibrated orifice type high pressure flowmeters are provided for both nitrogen (or air), oxygen, and carrier gas for the powder seeder. The nitrogen (or air) flow is adjustable by means of a centrally located control valve from 0 to 200 scfm, while oxygen is similarly adjustable from 0 to 50 scfm. Electrically operated valves provide remote on-off control of the gas flow.

A four range voltmeter indicates actual torch voltage in selectable scales of 0-500, 1000, 2000, and 5000 volts. The meter is accurate to 2% and is on a linear scale. A separate 100:1 voltage divider provides an indication of torch voltage to the remote recording instrument. The accuracy at this output jack is 1.0%, with a recorder D.C. resistance of 1.0 megohm or greater. A similar arrangement provides torch current indication with selectable ranges of 0-1000, 2000, 5000 and 10,000 amperes. This meter is provided with a front panel adjustment to provide current limiting at a preset value. Start of torch current is sensed by an "on" switch. A high current meter shunt is provided in the arc igniter for instrumentation of this unit. An output jack provides the arc current level for remote readout and recording, at a level of 5.0 millivolts per kiloampere torch current, with an accuracy of 1.0% at a recorder D.C. resistance of 1.0 megohm or greater.

An internally mounted rheostat controls the output power of the power supply through a magnetic amplifier/saturable reactor system. This combination provides power adjustment from no load to full load in 4.0 seconds, by means of a constant speed motor drive. A zero limit switch is provided in the rheostat drive to insure that the arc is not started at elevated supply voltages which would be



Figure 4. View of Control Console, Cooling Water Flow Meter, and N₂ Gas Surge Cylinders

injurious to its anode/cathode assembly. Push-button controls are furnished in the console for centralized operator control which provide in the manual mode of operation, the following on-off functions: Console power, gas flow, water pump, power supply, vacuum pump, and seeder. The torch current control, which is "up"- "down", may be operated either automatically or manually by means of a selector button. The water pump, power supply, and vacuum pump controls provide a relay switched voltage in order to operate the remotely located pump motor starters, and the power supply contactor. Interlocking of power supply controls with air and water controls are provided in order to preclude an improper sequencing of operation which could result in damage to the torch or its components. Either fully or semi-automatic as well as fully manual modes of equipment operation are selectable by the operator. Test operations for this experimental investigation have been performed exclusively in the manual mode, in order to introduce variations in selected functions to determine the side or end effects produced relative to power generated. Such variations include adjustments in seeding rates, slight incident frequency changes in the 3000 cycle coil power supply, and others described in subsequent sections.

2.3 Power Supply

The one megawatt, single unit A.C. power supply and rectifier bank utilizes a saturable core reactor for current control. This supply is housed in a special building, designed for this purpose. This unit is remotely controlled from the torch console and will operate from no load to full load in approximately five seconds. The unit is shown in Figure 5.

2.4 Power Substation

A separate power substation operating from a 26/4KV utility company supply, was constructed for this facility (Figure 6). It contains the three power

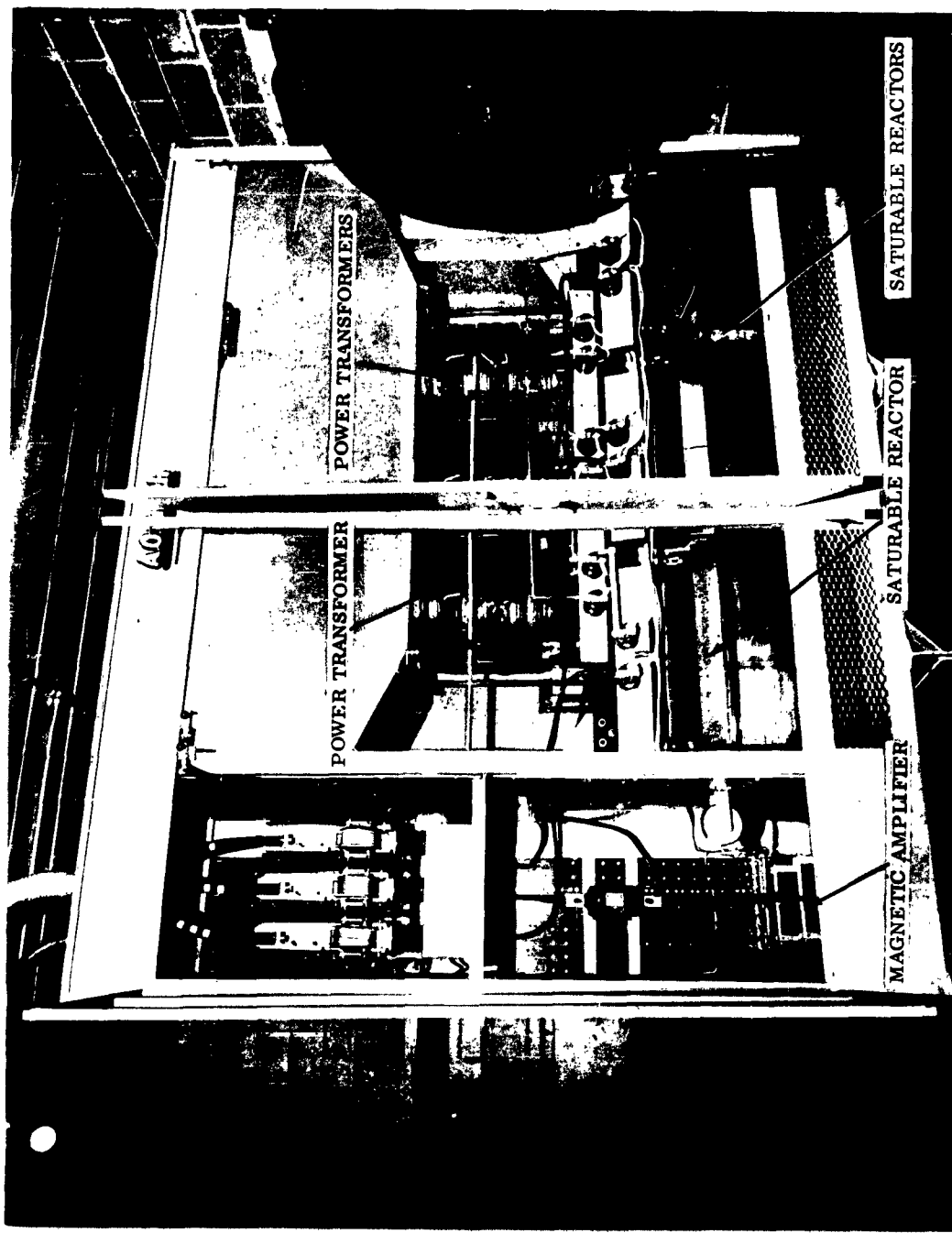


Figure 5. 1 Megawatt DC Power Supply, View of Saturable Reactors, Magnetic Amplifier, and Power Transformers

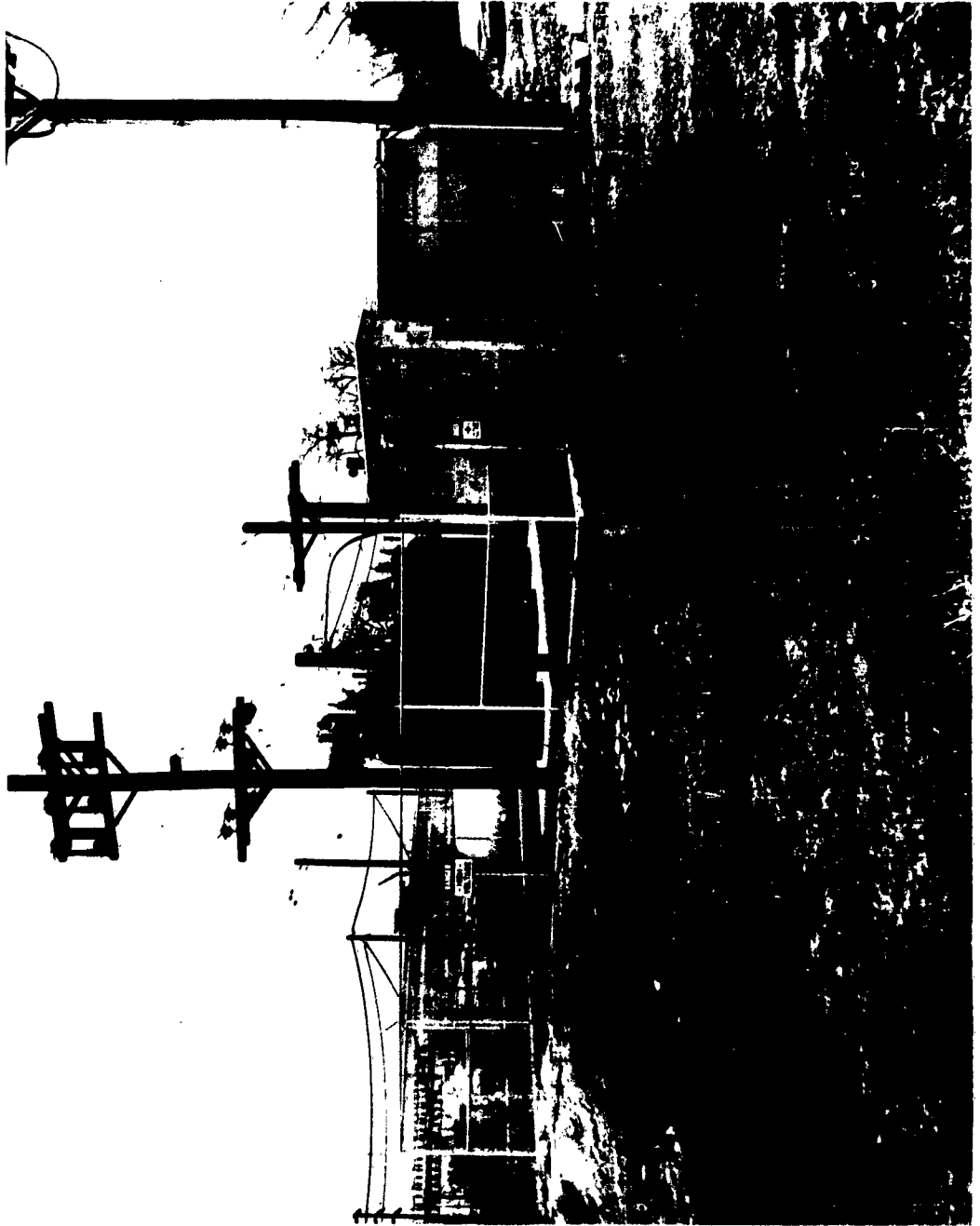


Figure 6. 26/4KV. Power Substation

transformers, an auxiliary 440V transformer and a main power line switch-gear unit.

2.5 Vacuum System

In order to permit extended supersonic plasma flow during experimental operation, a vacuum blow down or "dump" system was constructed, and the design is discussed in Section 5. This system was required to prevent the formation of a shock wave at the test section exit which occurs at 0.6 atmospheres for the test generator configuration designed for this program. This and other associated requirements are extensively discussed in Section 3. The tank and vacuum pump are shown in Figures 7 and 8.

2.6 Cooling System

A closed water cooling system was designed to meet the plasma arc torch and generator component cooling requirements (Figures 4 and 8). The design as well as performance characteristics are described in Section 5 and a schematic diagram of this system is shown in Figure 9.

2.7 Generator-Torch and Components

The "heart" of the MHD generator may be categorized into three basic groupings. The plenum chamber and supersonic nozzle, with its test section (Figures 2 and 3) constitute the first group and are covered in Section 3. Also covered, but not necessarily required for the present finalized configuration, was a supersonic diffuser unit. The second grouping includes the power extraction coils (shown installed on the test section in Figure 10), coil power supply, and power monitoring matrix (Figure 2), which are comprehensively discussed in Section 4. The Powder Injection Seeder (Figure 2) is described in this section and is an adjunct to the generator. The final group, which falls under the classification of instrumentation, is described herein, in Paragraph 2.7.7, and discussed more fully in Section 4.



Figure 7. Vacuum Dump Tank

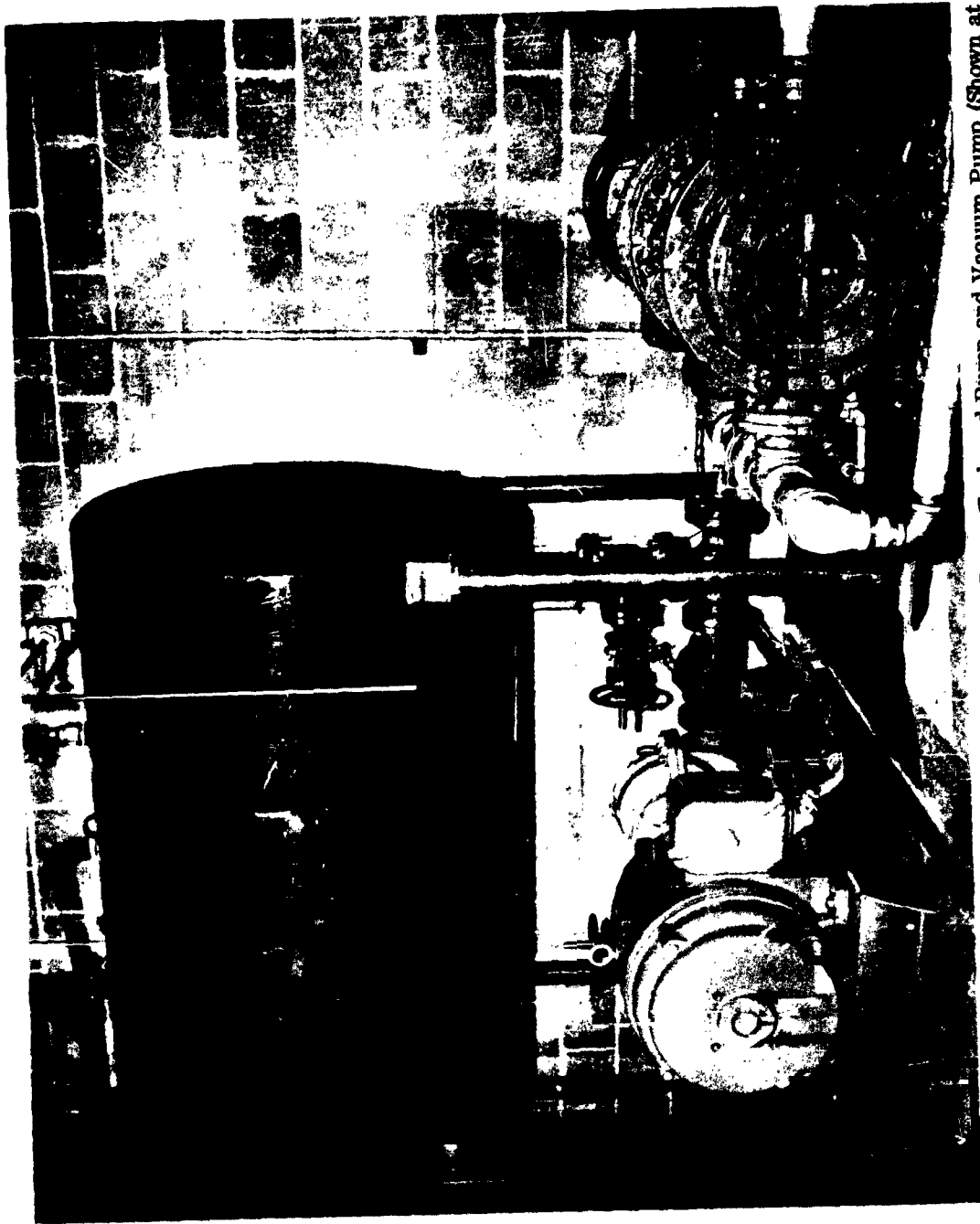


Figure 8. Cooling Water Surge Tank and Pump and Vacuum Pump (Shown at Right)

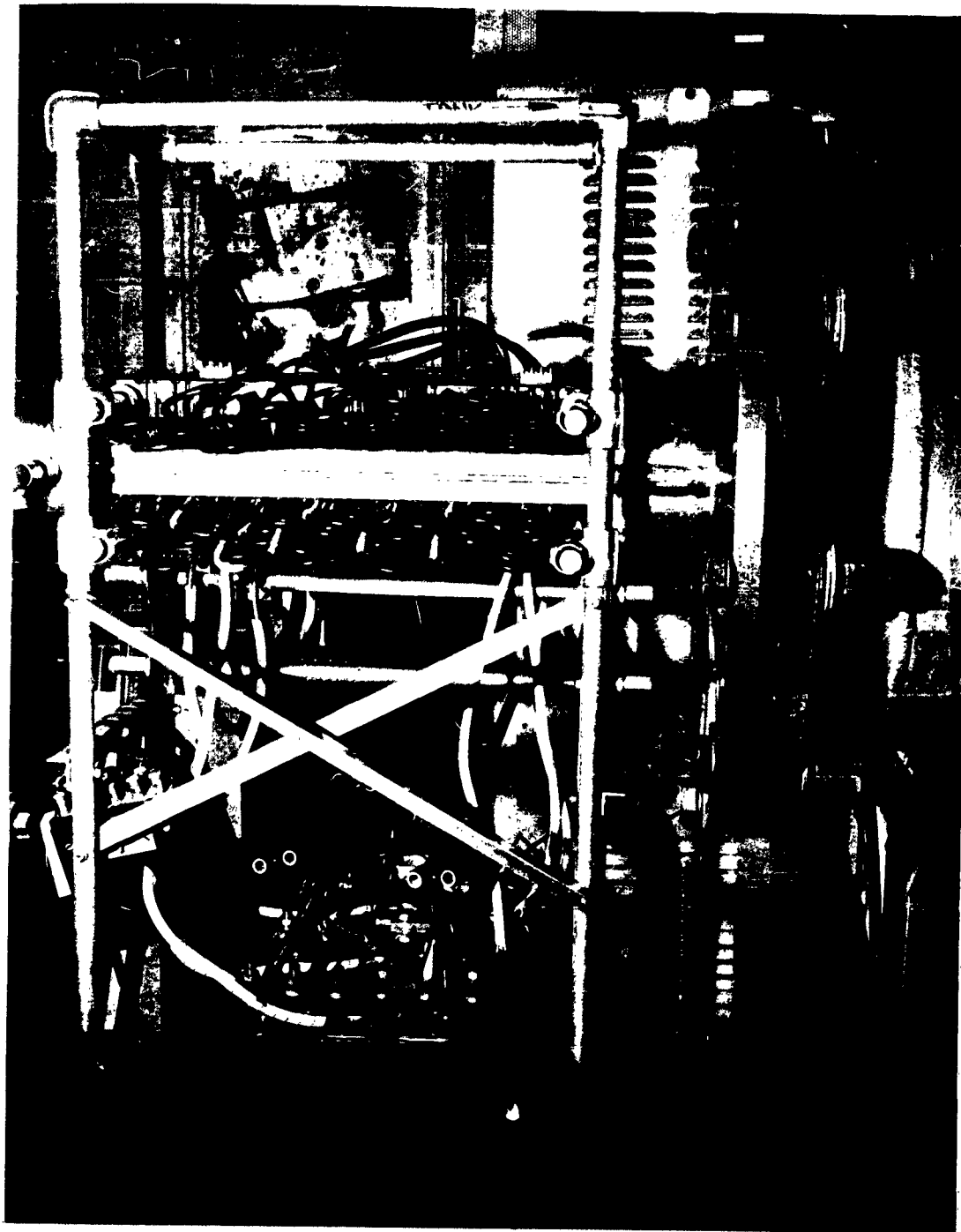


Figure 10. Power Extraction Coils Installed on Test Section

2.7.1 Plenum and Mixing Chamber

This cylindrical unit is a water-cooled component of the plasma arc torch and is attached to its exit nozzle. Oxygen and seeding materials are introduced to the plasma through this unit. This unit is shown in Figure 2 and discussed in Section 3.

2.7.2 Supersonic Nozzle

A two-dimensional supersonic venturi nozzle (which is cooled in a manner similar to the plenum chamber) was designed and built to provide the means of transition from circular plasma flow in the plenum chamber, to rectangular flow in the experimental test section. This converging-diverging nozzle was designed to accelerate the plasma to Mach 1.54.

2.7.3 Test Section

Two similar types of dielectric test sections were designed for this program. The first of which utilized a constant rectangular cross-sectional area. The present, or second type, maintained a constant vertical height, along an expanding straight-tapered horizontal width.

2.7.4 Diffuser

A rectangular to circular diffuser section was designed and built for use in conjunction with the constant cross-sectional area section previously mentioned. Operation of the equipment using the tapered test section appears to be satisfactory without the use of a diffuser.

2.7.5 Power Extraction Coils

The power extraction coils consist of an upper and lower three-phase coil section, bonded to a laminated, rectangular core. Both water-cooled sections are virtually identical. Cooling is accomplished by means of a tubular coil manifold. A tertiary winding utilized for the power monitoring matrix is bonded to the upper coil section. The three-phase coils provide the traveling wave field which

is used to extract power from the plasma. In Figure 10 they are shown attached to the test section.

2.7.6 Coil Power Supply

Two types of three-phase coil power supplies were built for this program with output frequencies of three thousand cycles at 5 KW per phase. The present rotating machine system utilizes three mechanically coupled Alexandersson type alternators, driven by a twenty-five horsepower variable speed motor, as shown by Figure 11. The control and regulator equipment for the rotating machine are each housed in a separate equipment chassis. The original unit which employed a power transistor supply system, was discarded due to unreliable operation experienced during test operation. It may be seen in Figure 2.

2.7.7 Power Monitoring Matrix

This network separates each of the three-phase traveling wave power components extracted from the ionized plasma by the coil system. It is shown in Figure 2. Phase nulling techniques are employed to cancel out the incident power from the alternator supply in order to directly record the power extracted from the plasma.

2.7.8 Positive Feed Seeder

Additional ionization of the plasma is obtained by the introduction of potassium carbonate (K_2CO_3) seeding compound into the plenum and mixing chamber. A standard positive feed, powder injection unit was modified to use nitrogen from the console controlled supply as the carrier gas for this purpose, and is shown in Figure 2. The readily dissociated alkali metal is introduced from this unit into the plenum and mixing chamber, immediately forward of the plasma arc orifice.

2.7.9 Instrumentation

In order to obtain and record the test data needed to perform the experi-

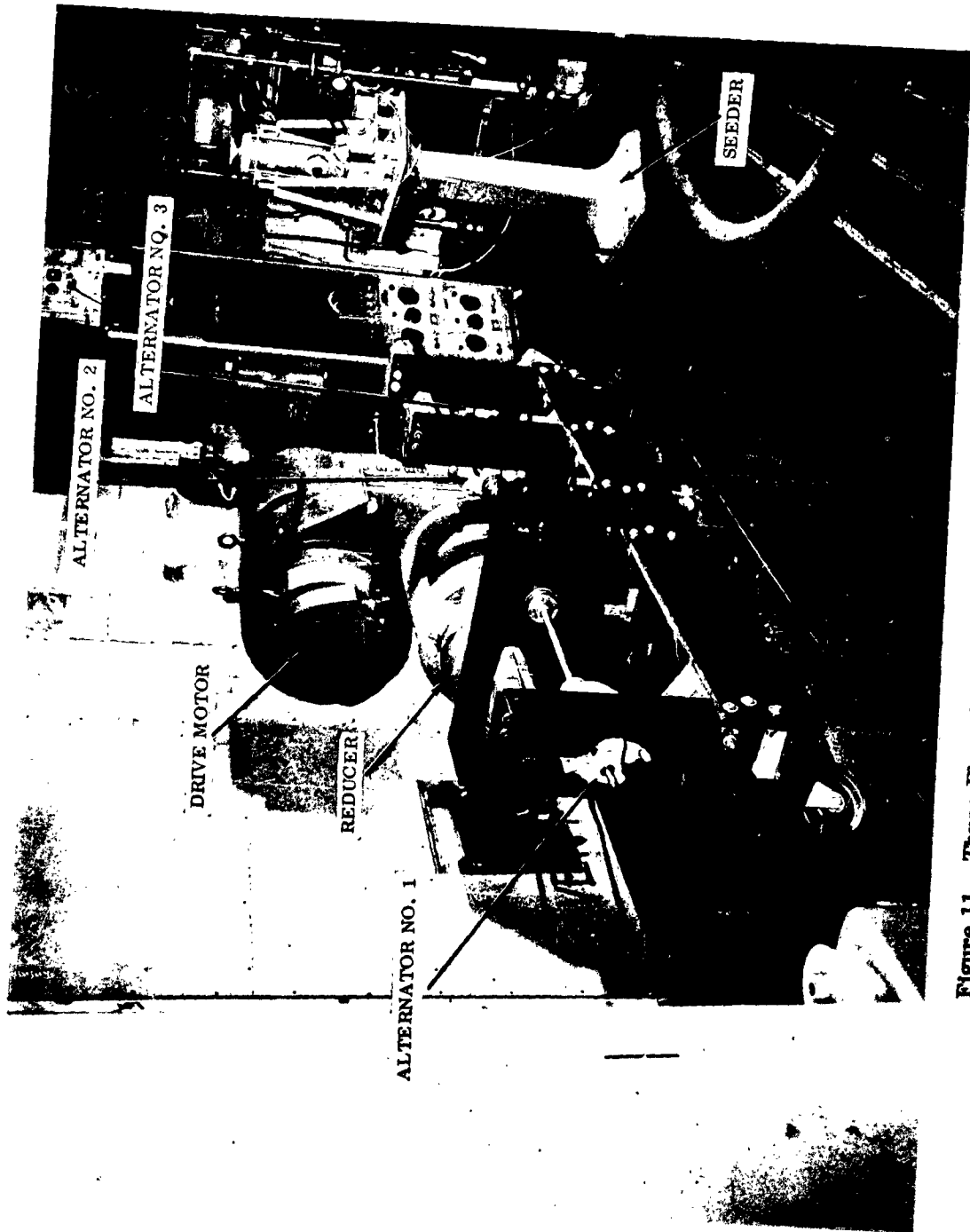


Figure 11. Three Phase Motor/Alternator, Coil Power Supply Set

mental portion of this investigation, several items of apparatus were designed and built. Pressure measurements are obtained at four stations during experimental test runs. These locations are the plenum chamber/supersonic nozzle, test section entrance and exit, and the vacuum dump tank orifice. The readings are displayed on a mercury manometer board. Timing sequences are displayed on a master clock. All of the previously mentioned readings, the nitrogen and oxygen mass flow rates, and an oscillograph trace of the nulled output signal level are recorded on film with a 35 mm Robot camera. The master clock is triggered at the start of the test run in conjunction with a multi-channel Sanborn recorder. Traces of differential cooling water temperature, extracted or generated voltage and current, arc current and voltage, and phase angle are recorded on the Sanborn unit. Exciting frequency of the excitation power supplied to the three-phase coils (in this case 3000 cycles) is displayed on a digital frequency counter.

3. AERODYNAMIC DESIGN OF GENERATOR

3.1 Introduction

From the aerodynamics point of view, the present A.C. MHD power generator can be regarded as just an ordinary blow-down tunnel with its usual components, viz., a plenum chamber serving as a high-pressure reservoir into which is connected a nozzle. This is followed by a "test-section" and supersonic diffuser, the latter leading into a vacuum tank which serves as the low-pressure reservoir as well as a "sink" or dump tank.

It was shown in Part I of this work (p. 86, ref. 1) that more electrical energy is extracted from the plasma, for the same initial total enthalpy and pressure, in supersonic as compared to subsonic flow. It was therefore, decided to have supersonic flow in the "test-section"; this, of course, meant that the nozzle mentioned above had to be of the converging-diverging type.

The procedure adapted for the design and analysis of the plenum-nozzle combination was as follows:

- a) Design the supersonic part of the nozzle by the Method of Characteristics as applied to steady, two-dimensional, irrotational, isentropic flow of an ideal gas, neglecting skin friction and heat transfer.
- b) Regarding the gently curving wall of the nozzle as a flat plate with leading edge at the throat, compute laminar boundary layer displacement thickness along the nozzle walls. Add these displacement thicknesses to the four walls to obtain the final internal dimensions of the supersonic part of the nozzle.

- c) Having thus fixed the exit-to-throat area ratio of the nozzle, determine flow parameters in the plenum chamber and nozzle, taking into account real gas effects but neglecting skin friction and heat transfer to the walls. In addition to the above area ratio, three additional imposed conditions are necessary to uniquely determine the flow. The three conditions selected were
- (i) isentropic flow throughout,
 - (ii) a stagnation pressure of one atmosphere, and
 - (iii) a static temperature of 5850°R at the exit of the nozzle, to assure an electrical conductivity of approximately 200 mho/m at the entrance to the "test-section" when the air is seeded with 1% (by weight) of Potassium Carbonate (K_2CO_3), ref. 2.
- d) Evaluate how sensitive the parameters at the nozzle exit are to variations in stagnation conditions. Specifically, determine the mass and energy flow rate as a function of stagnation pressure and enthalpy, and also how these affect the velocity and state properties at the exit of the nozzle.

The procedure used in designing the remaining components of the "blow-down" tunnel are discussed under their respective headings.

3.2 Nozzle Design and Performance

3.2.1 Design of Supersonic Nozzle by Method of Characteristics

The supersonic nozzle was designed by the method of characteristics as applied to two-dimensional, irrotational, isentropic flow of an ideal gas under steady-state conditions, neglecting all surface and body forces other than the driving pressure gradient (see, for example, Chapter 15 of reference 3).

For the reason stated in the introduction, it was decided to accelerate the flow to some supersonic velocity before introducing it into the "test-section". Since the static temperature, and hence also the electrical conductivity, decreases with increasing Mach number, a low supersonic Mach number had to be selected. A Mach number of 1.600 was somewhat arbitrarily chosen as a compromise between keeping the static temperature as high as possible while at the same time staying sufficiently away from a Mach number of unity to avoid choking and other undesirable transonic properties. The Mach number for the uniform and parallel flow at the exit of the nozzle was thus taken as

$$\begin{aligned}
 &\text{Exit Mach Number} && M_{\text{exit}} = 1.600 \\
 &\text{With corresponding} \\
 &\text{Prandtl-Meyer angle} && \gamma_{\text{exit}} = 14.8596^\circ && (3.1) \\
 &\text{And corresponding} \\
 &\text{Mach angle} && \mu_{\text{exit}} = 38.68^\circ
 \end{aligned}$$

This was to be produced from assumed sonic velocity at the throat, viz.,

$$\begin{aligned}
 &\text{Throat Mach Number} && M^* = 1.000 \\
 &\text{With corresponding} \\
 &\text{Prandtl-Meyer angle} && \gamma^* = 0.0000^\circ && (3.2) \\
 &\text{And corresponding Mach} \\
 &\text{angle} && \mu^* = 90.00^\circ
 \end{aligned}$$

Flow acceleration from $M^* = 1.000$ to $M_{\text{exit}} = 1.600$ was assumed to be produced by 14 (an arbitrarily chosen number) discrete jumps or "expansion waves". Since the flow is symmetric about the centerline of the nozzle, the centerline can be regarded as a solid plane boundary, with its associated property that waves reflect

off it in same sense (that is, compression waves reflect as compression waves and expansion waves reflect as expansion waves). The above-mentioned 14 expansion waves consisted actually of seven right-running waves originating from the expansion zone of the nozzle (see Figure 12), and seven left-running waves representing the former seven waves after having been reflected by the solid plane boundary.

The nozzle's expansion-zone length is so chosen as to avoid any of the reflected left-running waves from impinging on that zone. The reflected left-running waves, when impinging on the nozzle contour past the expansion zone, are purposely cancelled, in order to produce a wave-free flow at the nozzle exit. This is accomplished in the "compression-zone" of the nozzle by contouring the nozzle back to parallel the centerline.

The above scheme was carried out using seven centered simple waves along the expansion zone of the nozzle, each representing the same turning angle ($\Delta \theta$). Since the same turning angle is also required to cancel each of the seven waves, it is immediately seen that the entire nozzle contour is composed of 14 turning points. Also, since these 14 turning points accomplish the same flow acceleration as would be obtained with a Prandtl-Meyer deflection of 14.8596° , it is clear that the angular deflection at each of the 14 turning points on the nozzle wall must be equal to

$$(\Delta \theta) = \frac{14.8596^\circ}{14} = 1.0614^\circ \quad (3.3)$$

Having thus determined the turning angle at each of the 14 straight-line segments that comprise the contour of the entire nozzle, the slopes of the expansion waves (ϕ), (also referred to as characteristic lines or Mach waves) are obtained as follows (p. 467, reference 3)

ROMAN NUMERALS INDICATE REGIONS OF UNIFORM FLOW, THE VELOCITY VECTOR OF WHICH IS INCLINED TO THE ζ BY MULTIPLE ANGLES OF 1.0614 DEGREES
 [VIZ., $\bar{0} \equiv (\theta = 0^\circ)$, $\bar{I} \equiv (\theta = 1.0614^\circ)$, $\bar{II} \equiv (\theta = 2.1228^\circ)$, ETC.]

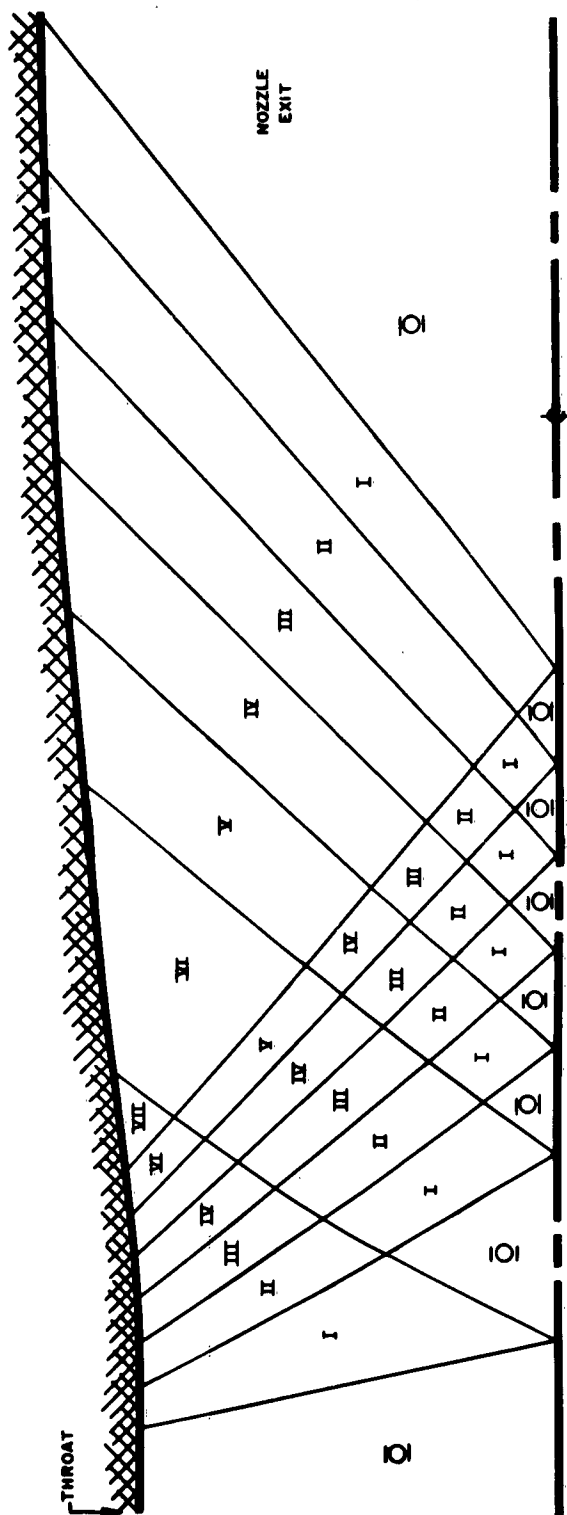


Figure 12. Derivation of Nozzle's Contour by Method of Characteristics

$$\text{for right-running} \quad \left\{ \begin{array}{l} \theta_2 - \nu_2 = \theta_1 - \nu_1 \end{array} \right. \quad (3.4)$$

$$\text{Mach waves} \quad \left\{ \begin{array}{l} \phi = \frac{1}{2} [(\theta_1 + \theta_2) - (\mu_1 + \mu_2)] \end{array} \right. \quad (3.5)$$

$$\text{For left-running} \quad \left\{ \begin{array}{l} \theta_2 + \nu_2 = \theta_1 + \nu_1 \end{array} \right. \quad (3.6)$$

$$\text{Mach waves} \quad \left\{ \begin{array}{l} \phi = \frac{1}{2} [(\theta_1 + \theta_2) + (\mu_1 + \mu_2)] \end{array} \right. \quad (3.7)$$

where μ and ν are uniquely related (see, for example, reference 4). An additional imposed boundary condition, required to construct the entire characteristic network, is that the flow be parallel to the centerline (e.g., $\theta = 0$) in all regions bordering the centerline.

The characteristic network and nozzle contour obtained in the manner described above is shown in Figure 12. The resulting exit-to-throat area ratio was 1.246, compared to the theoretical value of 1.250 (ref. 4). The .32 percent discrepancy is attributed mainly to the limited number of expansion waves employed in constructing the characteristic network.

3.2.2 Allowance for Boundary Layer Growth

The gently curved wall of the nozzle was regarded, as far as evaluating boundary layer growth is concerned, as a flat plate. Displacement thickness was obtained from the following relation pertaining to compressible laminar boundary layers over flat plates (reference 5)

$$\delta^* = 1.75 \sqrt{\frac{\nu_e x C}{\nu_e}} \left[1 + 1.392 \left(\frac{\gamma - 1}{2} \right) M_e^2 \right] \quad (3.8)$$

where the kinematic viscosity (ν_e), velocity (U_e), and Mach number (M_e) refer to conditions at the outer edge of the boundary layer, and were evaluated from the known solution of the inviscid flow in the nozzle, as previously obtained by

tions mentioned in the introduction (see also Equation (3.10)). The distance (x) was reckoned from the throat, and the ratio of specific heats (γ) was evaluated from references 6 and 7 for the above conditions and was found to be essentially constant throughout the nozzle and equal to 1.17. The quantity (c) in Equation (3.8) is the proportionality factor in Sutherland's formula relating viscosity to temperature, viz.,

$$C = \sqrt{\frac{\bar{T}_w}{T_e}} \left(\frac{T_e + S}{\bar{T}_w + S} \right) \quad (3.9)$$

where \bar{T}_w = average wall temperature, assumed in the numerical computation to be constant and equal to 1000°R

T_e = static temperature at the outer edge of the boundary layer. This was computed along the nozzle contour from the known flow field.

S = Sutherland's constant, S = 198.6°R

See, for example, reference 8.

Displacement thicknesses computed as described above were added to the ordinates of the nozzle obtained by the Method of Characteristics. Final nozzle coordinates, given in Table I, represent faired values of the compounded ordinates.

The width of the two dimensional nozzle was arbitrarily chosen as one inch. As seen in Table I, the axial distance between throat and nozzle exit came out (by the Method of Characteristics) to be 3.418 inches. At this distance away from the leading edge of a flat plate, boundary layer displacement thickness based on flow parameters at the nozzle exit is equal to .0476 inches. To allow for this boundary layer growth, the side walls of the supersonic part of the nozzle were tapered linearly from 1.0000 inches at the throat to 1.0952 inches

at the nozzle exit.

3.2.3 Flow Parameters in the "Plenum Chamber", Throat and

Nozzle Exit, Including Considerations of Real Gas Effects

Caution must be exercised in trying to evaluate flow parameters in the above nozzle when a plasma rather than an ideal gas is being accelerated. Only features which remain unaffected by replacing the ideal gas by a plasma can be regarded as still valid; these include (1) the inviscid exit-to-throat area ratio previously determined (viz., $\frac{A_{\text{exit}}}{A^*} = 1.246$), and (2) the assumption that the entire flow process remains isentropic. Exit Mach number can, of course, no longer be assumed equal to 1.600, but rather must be evaluated subject to additional imposed parameters (see below).

The test facility is regarded in the following analysis as a blow-down tunnel, with atmospheric air serving as the high pressure reservoir. This immediately establishes one of the imposed parameters, namely, that the stagnation pressure be atmospheric. Static temperature at the exit of the nozzle was chosen as the second imposed parameter, and was somewhat arbitrarily set equal to 5850°R. The four conditions necessary to uniquely determine (for an adequate pressure gradient) the flow in the nozzle, are thus:

- (a) $\frac{A_{\text{exit}}}{A^*} = 1.246$
 - (b) isentropic flow throughout
 - (c) $P_{\text{total}} = 1 \text{ atm.}$
 - (d) $T_{\text{exit}} = 5850^\circ\text{R}$
- (3.10)

It should be noted that (P_{total}) and (T_{exit}) are not the only parameters which, when added to conditions (3.10(a)) and (3.10(b)), will uniquely determine the flow. Any other two flow parameters, either in the "plenum chamber", throat,

Determining flow parameters in the "plenum chamber", throat, and nozzle exit for "initial conditions" (3.10) involves the following steps:

1. Select a value for the total enthalpy (h_{total}).
2. From the Mollier charts for air in thermodynamic equilibrium (reference 6), obtain the isentrope ($\frac{S}{R}$) corresponding to the selected value of (h_{total}) and to (P_{total}) = 1 atm., which will then remain constant everywhere in the nozzle.
3. With ($\frac{S}{R}$) and $T_{exit} = 5850^{\circ}R$, find nozzle exit state properties h_{exit} , P_{exit} , and Z_{exit} .
4. Assume several values of throat enthalpy (h^*) and, with ($\frac{S}{R}$), find corresponding throat state properties P^* , Z^* , and T^* .

To determine which of the several values selected for (h^*) in (4) truly represents the enthalpy at the throat, reference is made to the principle of continuity, viz.,

$$\rho u A = \text{const.} \quad (3.11)$$

Since the throat represents the minimum cross-sectional area of the nozzle, it follows that the product

$$\rho^* u^* = \frac{P^*}{Z^* R T^*} \sqrt{2 g_j (h_{TOTAL} - h^*)} \quad (3.12)$$

is maximum at the throat. Relation (3.12) must next be evaluated for the several selected values of (h^*), and the results plotted versus (h^*). The resulting curve has a maximum which corresponds to the true value of (h^*) for the total enthalpy value selected in (1).

Having thus established the true properties at the throat, exit-to-throat

area ratio is then obtained from

$$\frac{A_{EXIT}}{A^*} = \frac{\rho^* u^*}{\rho_{EXIT} u_{EXIT}} = \left(\frac{P^*}{P_{EXIT}} \right) \left(\frac{Z_{EXIT}}{Z^*} \right) \left(\frac{T_{EXIT}}{T^*} \right) \sqrt{\frac{h_{TOTAL} - h^*}{h_{TOTAL} - h_{EXIT}}} \quad (3.13)$$

If this ratio does not turn out equal numerically to the specified value of 1.246 [see relation (3.10(a))], the entire procedure has to be repeated again and again for different assumed values of (h_{TOTAL}) , until relation (3.13) yields the desired numerical value.

State properties and flow parameters in the "plenum chamber" throat and nozzle exit, obtained in the manner described above, are given in Table II.

Throat dimensions were arbitrarily selected as

$$\begin{aligned} \text{height of throat} &= 2.020 \text{ inches} \\ \text{width of throat} &= 1.000 \text{ inch} \end{aligned} \quad (3.14)$$

From (3.11), (3.14) and the data contained in Table II, there is obtained

$$\text{mass flow rate} = .174 \text{ lb}_m/\text{sec} \quad (3.15)$$

It should be noted that the exit Mach number, taking into account real gas effects $\bar{M}_{EXIT} = 1.53$, see Table II, differs only slightly from the value $M_{EXIT} = 1.60$ for which the nozzle was initially designed by the method of characteristics. This slight change in Mach number was considered insignificant as far as having to re-evaluate boundary layer displacement thickness is concerned.

3.2.4 Perturbation of Nozzle Exit Parameters

The nozzle, as was mentioned earlier, can be regarded as supplying supersonic flow to a test section of a blow-down wind tunnel. In this respect, it is of interest to find the range of flow parameters at the nozzle exit that can be obtained by perturbing the two quantities which, in practice, lend themselves most

readily to variations, namely, stagnation pressure and enthalpy.

Retaining conditions (3.10 (a)) and (3.10(b)) and selecting several values of (P_{total}) and (h_{total}) , flow parameters at the nozzle exit are obtained as follows:

- a. For each selected pair of (P_{total}) and (h_{total}) obtain the corresponding isentrope (S/R) from reference 6.
- b. Select several values of h^* and, with the aid of reference 6, obtain corresponding values of Z^* , T^* , and P^* .
- c. Compute $u^* = \sqrt{2 g_j (h_{total} - h^*)}$ and evaluate a^* with the aid of Figure 6 of reference 9.
- d. Plot u^* and a^* versus h^* ; the point of intersection of the two curves gives the correct value of h^* , thus yielding all flow parameters at the throat.
- e. Find the mass flow rate with the aid of Equation (3.11) as evaluated at the throat.
- f. Select a value for h_{exit} and, with the aid of reference 6, obtain corresponding values of Z_{exit} , T_{exit} , and P_{exit} . Compute the corresponding mass flow rate with the aid of Equation (3.11) as evaluated at the nozzle exit. Should the mass flow rate thus obtained differ from that established in step (e) for the throat, repeat step (f) for different values of h_{exit} until agreement is reached.

Flow velocity at the exit of the nozzle, obtained for several selected values of stagnation pressure and enthalpy in the manner described above, is shown in Figure 13. As seen from this figure, changes in velocity are primarily due to enthalpy variations and to a much smaller extent to variations in

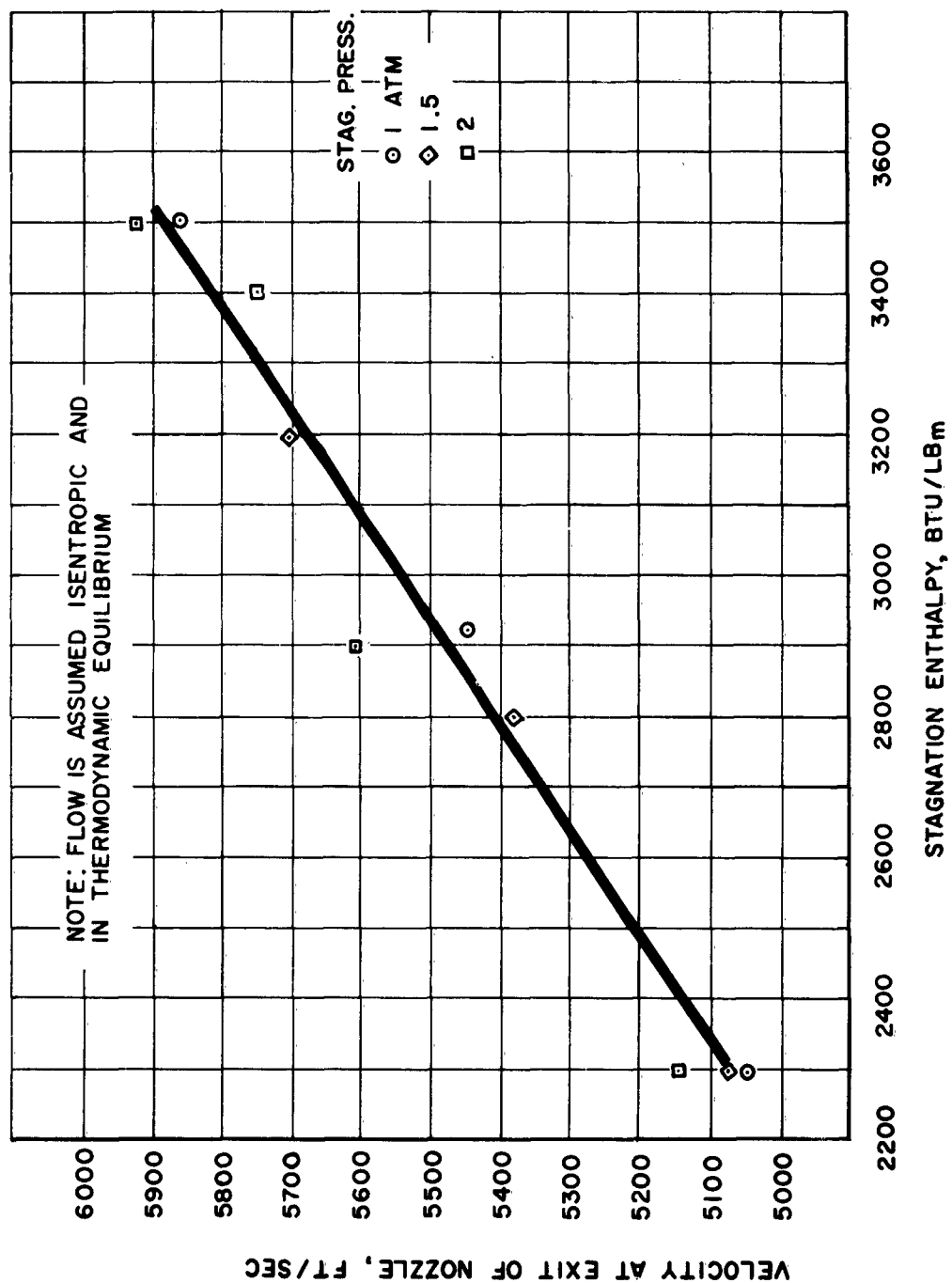


Figure 13. Velocity at Exit of Nozzle as Affected by Stagnation Pressure and Enthalpy

stagnation pressure. Slight inconsistencies in the scattering of the computed data points in Figure 13 are attributed to difficulties involved in reading the Mollier charts.

For the pressure and enthalpy range of Figure 13 exit Mach number remained essentially constant and equal to 1.53 (see Table II), with deviations amounting to less than $\pm 2\%$ of this value.

Static temperature, pressure and density at the exit of the nozzle, for the same stagnation pressures and enthalpies used in Figure 13, are shown in Figures 14, 15, and 16, respectively. Static temperature at the exit to the nozzle, like exit velocity, is seen from Figure 14 to be much more sensitive to changes in stagnation enthalpy than to stagnation pressure. On the other hand, changes in static pressure at the exit to the nozzle are due almost entirely to variations in stagnation pressure (see Figure 15). Static density at the nozzle exit and mass flow rate are shown in Figures 16 and 17, respectively, as functions of stagnation pressure and enthalpy.

3.2.5 Power Requirements (Ideal Case)

Total energy flow rate through the nozzle is given, for isentropic flow, by

$$(\text{total energy flow rate}) = \dot{m} h_{\text{total}} \quad (3.16)$$

where (\dot{m}) is the mass flow rate and (h_{total}) is the stagnation enthalpy. Now, assume there exists an ideal power converter which transforms electrical power input to increased enthalpy of onflowing air, and that this is accomplished with 100% efficiency. If the air whose enthalpy is to be increased to (h_{total}) is initially at an enthalpy level corresponding to standard atmospheric conditions $(h_{\text{atm}} = 127 \text{ BTU/lb}_m)$, the power required by such a machine is

$$P_{\text{ideal}} = \dot{m} (h_{\text{total}} - h_{\text{atm}}) \quad (3.17)$$

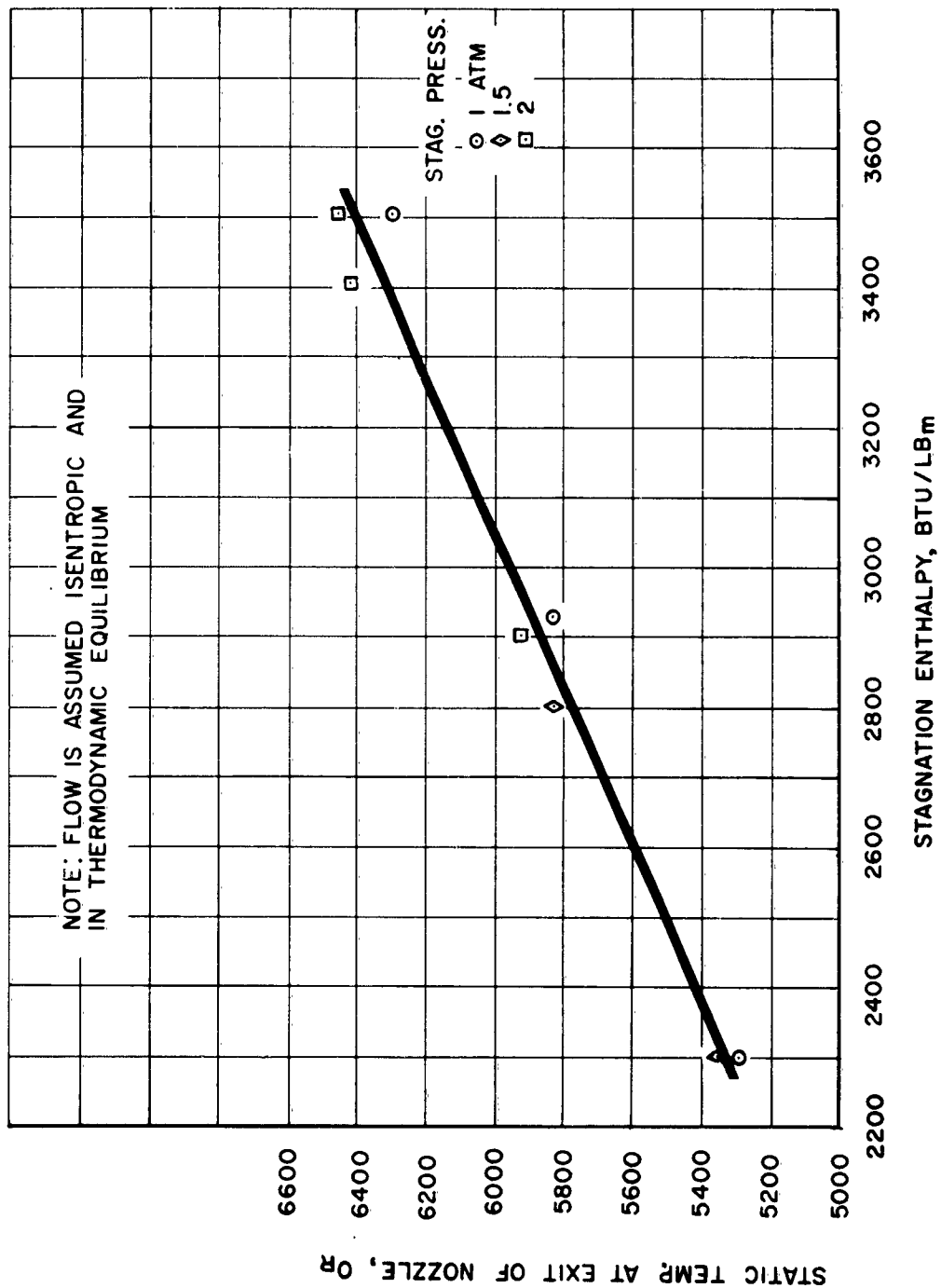


Figure 14. Static Temperature at Exit of Nozzle as Affected by Stagnation Pressure and Enthalpy

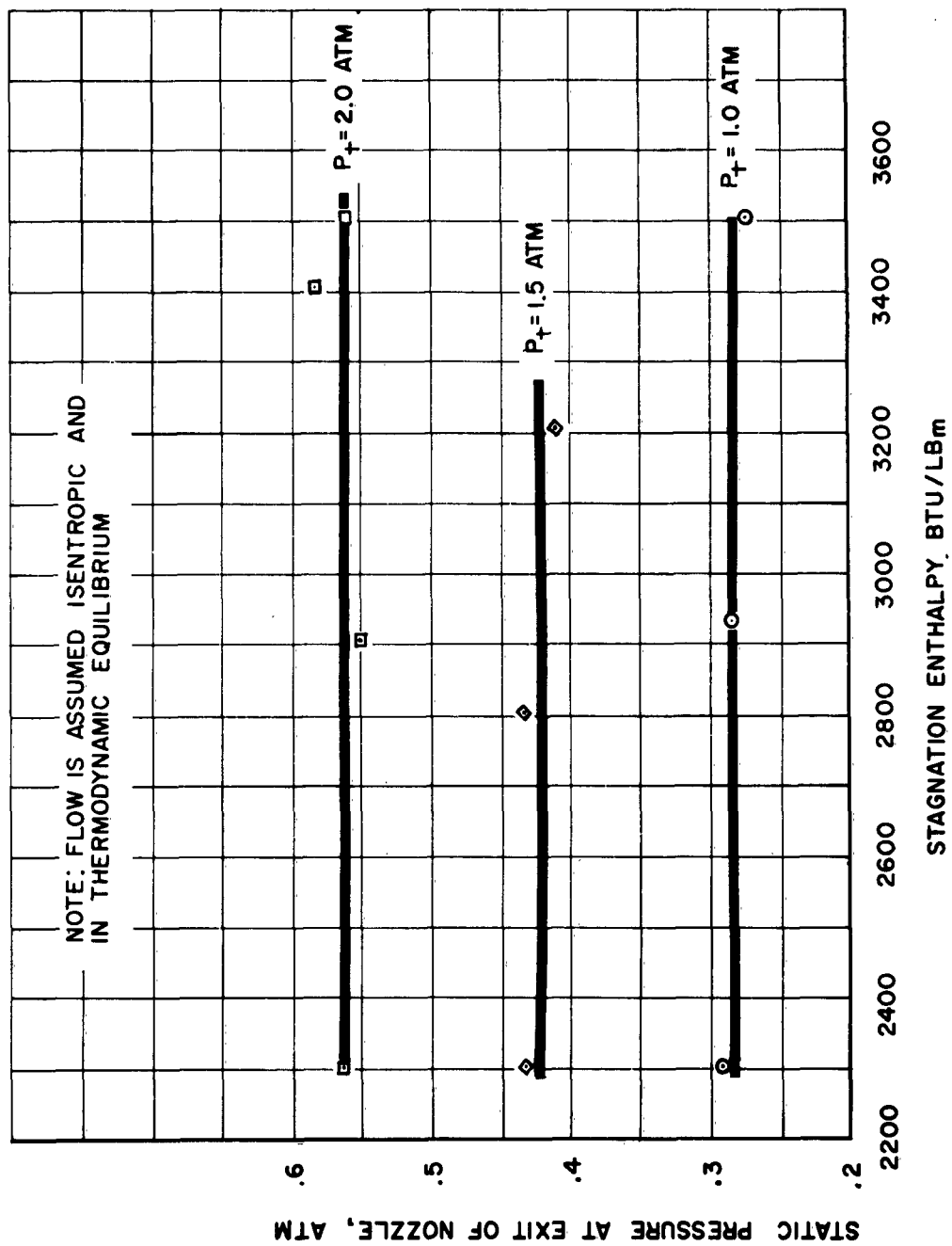


Figure 15. Static Pressure at Exit of Nozzle as Affected by Stagnation Pressure and Enthalpy

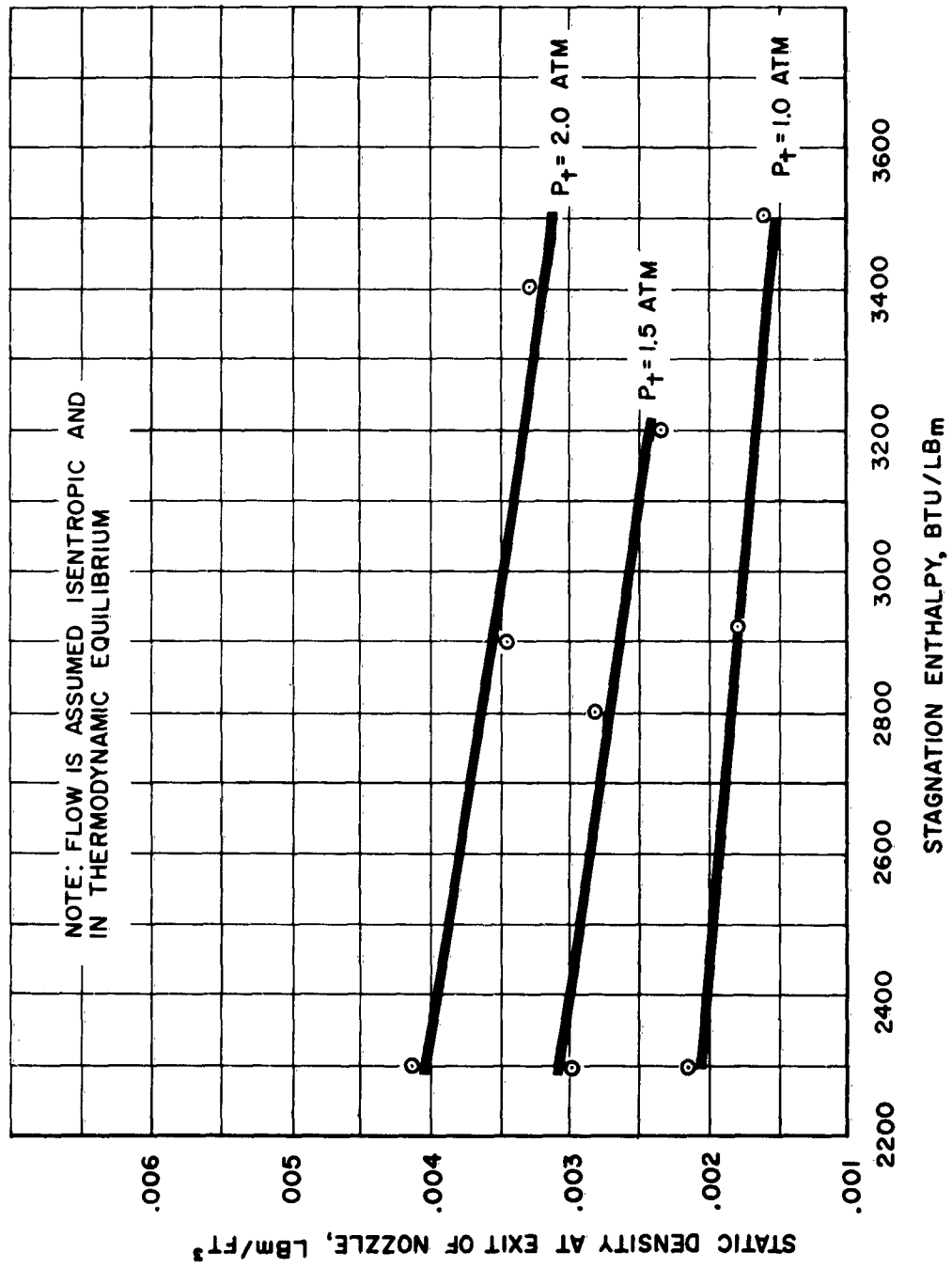


Figure 16. Static Density at Exit of Nozzle as Affected by Stagnation Pressure and Enthalpy

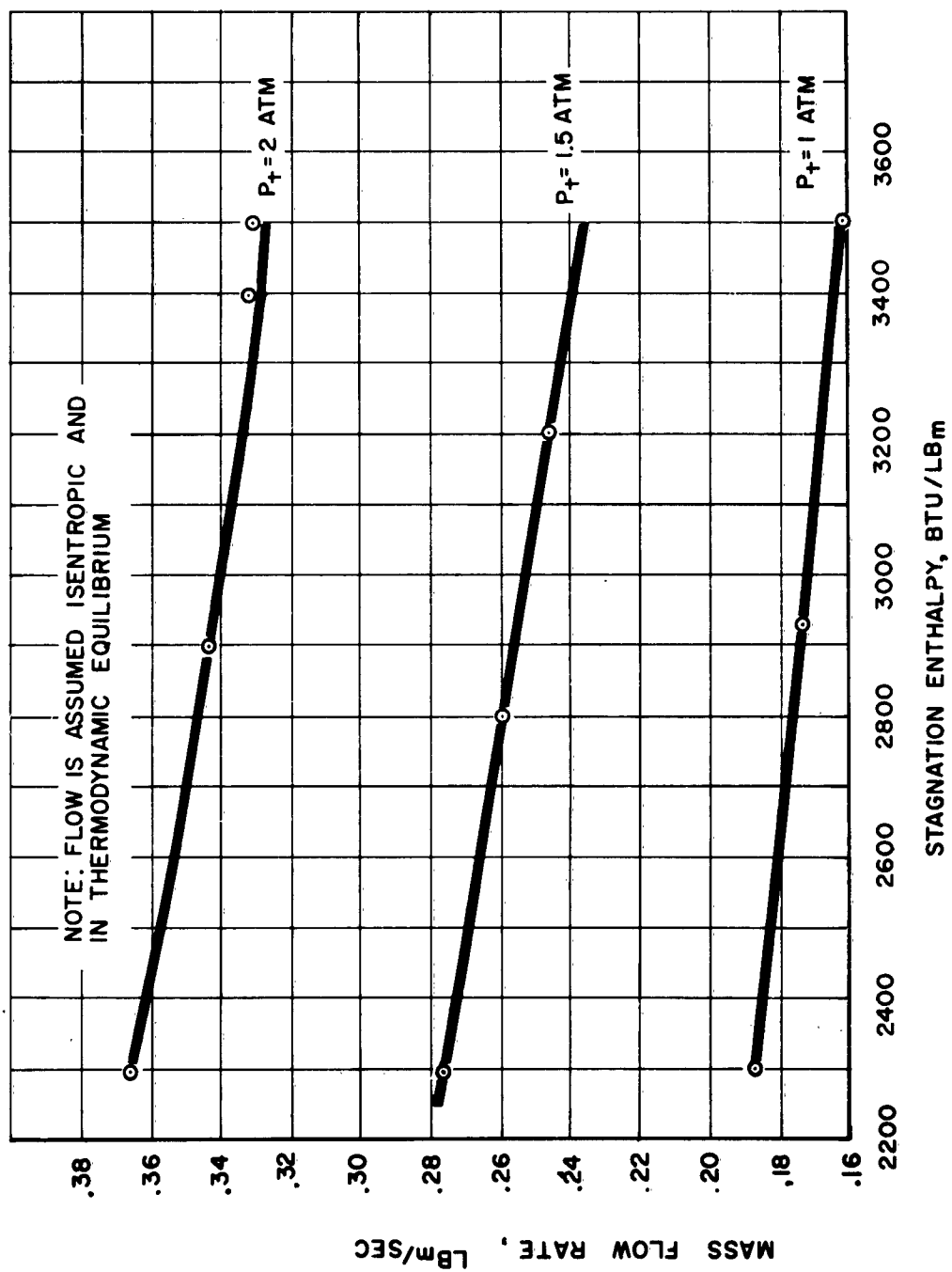


Figure 17. Mass Flow Rate as Affected by Stagnation Pressure and Enthalpy

Relation (3.17), evaluated for conditions of Figure 7, is shown in Figure 18.

3.2.6 Subsonic Part of Nozzle

Ideally, the subsonic part of the nozzle should be made sufficiently long and have such gentle curvature as to insure that the sonic surface is almost exactly a plane normal to the centerline of the nozzle at the throat (p. 516 reference 3).

To keep heat losses to the walls as low as possible, it was necessary to limit the length of the subsonic inlet to a bare minimum still commensurate with the above criterion. The subsonic part of the nozzle was designed, in addition, to convert the axi-symmetric low subsonic flow in the plenum chamber to two-dimensional uniform flow at the throat. A perspective view of the plenum chamber and converging-diverging nozzle is shown in Figure 19. Additional details concerning the subsonic inlet are shown in Figure 20.

3.3 Test Section

Variation in cross-sectional area required to maintain constant velocity flow in the test section was previously computed and is given in Section 7 of reference 1. The walls were assumed in those computations to be isothermal, and due consideration was given to skin friction and heat-transfer effects as applied to compressible turbulent boundary layer flow. Real gas effects were also included in those computations.

An overall length of 24 inches was somewhat arbitrarily selected for the "test section", which also includes two end flanges, see Figure 21. The cross-sectional area at the entrance to the test section was, of course, made equal to the nozzle's exit area, viz., 1.0952 inches x 2.612 inches, see Section 3.2.2 and Table I. The 1.0952 inch width was kept constant along the test section, with the required increase in cross-sectional area being applied exclusively to

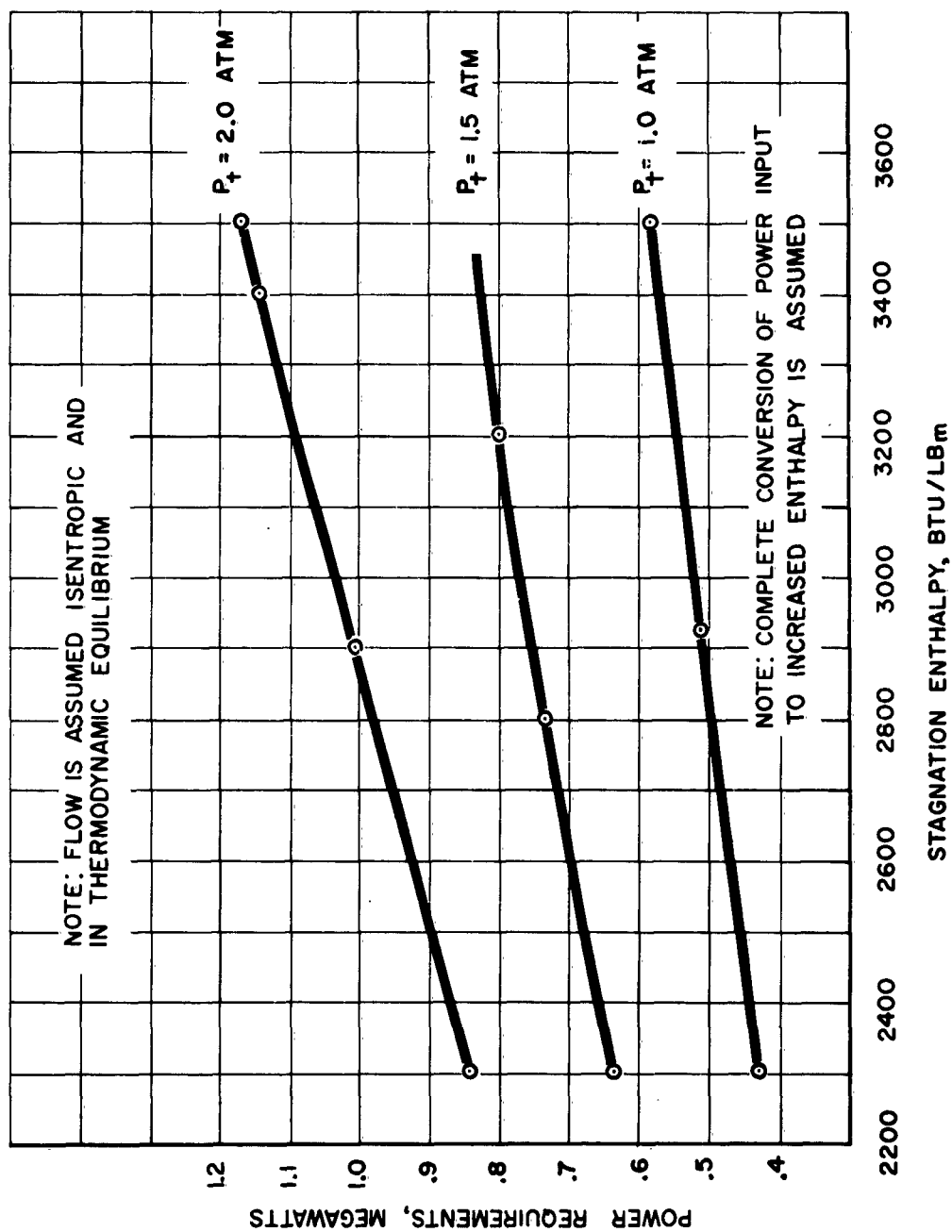


Figure 18. Power Required to Increase Enthalpy from 127 BTU/LB (Standard Atmospheric Air) to Stagnation Value ----

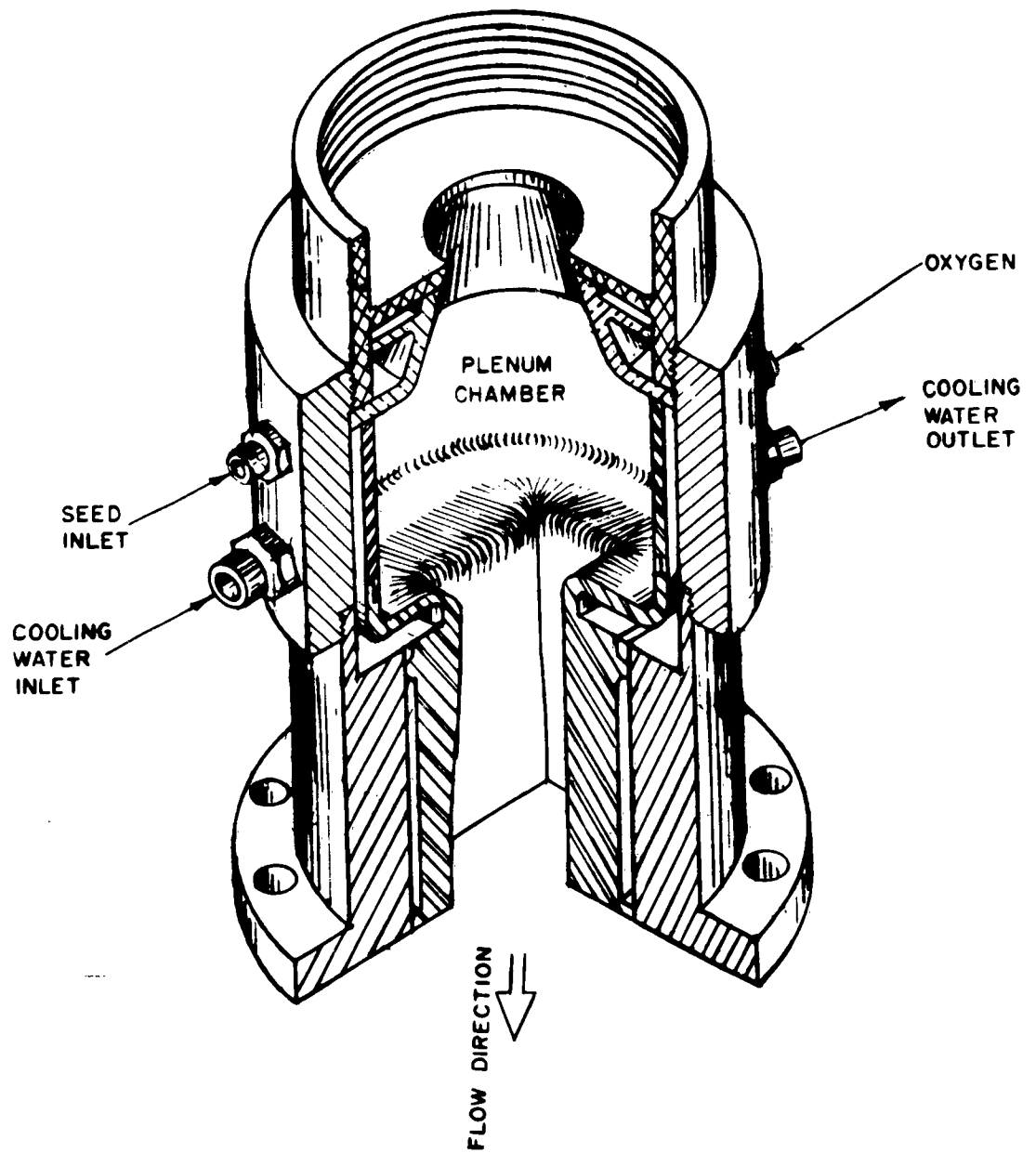


Figure 19. Perspective View - Plenum Chamber Blending into Diverging Nozzle

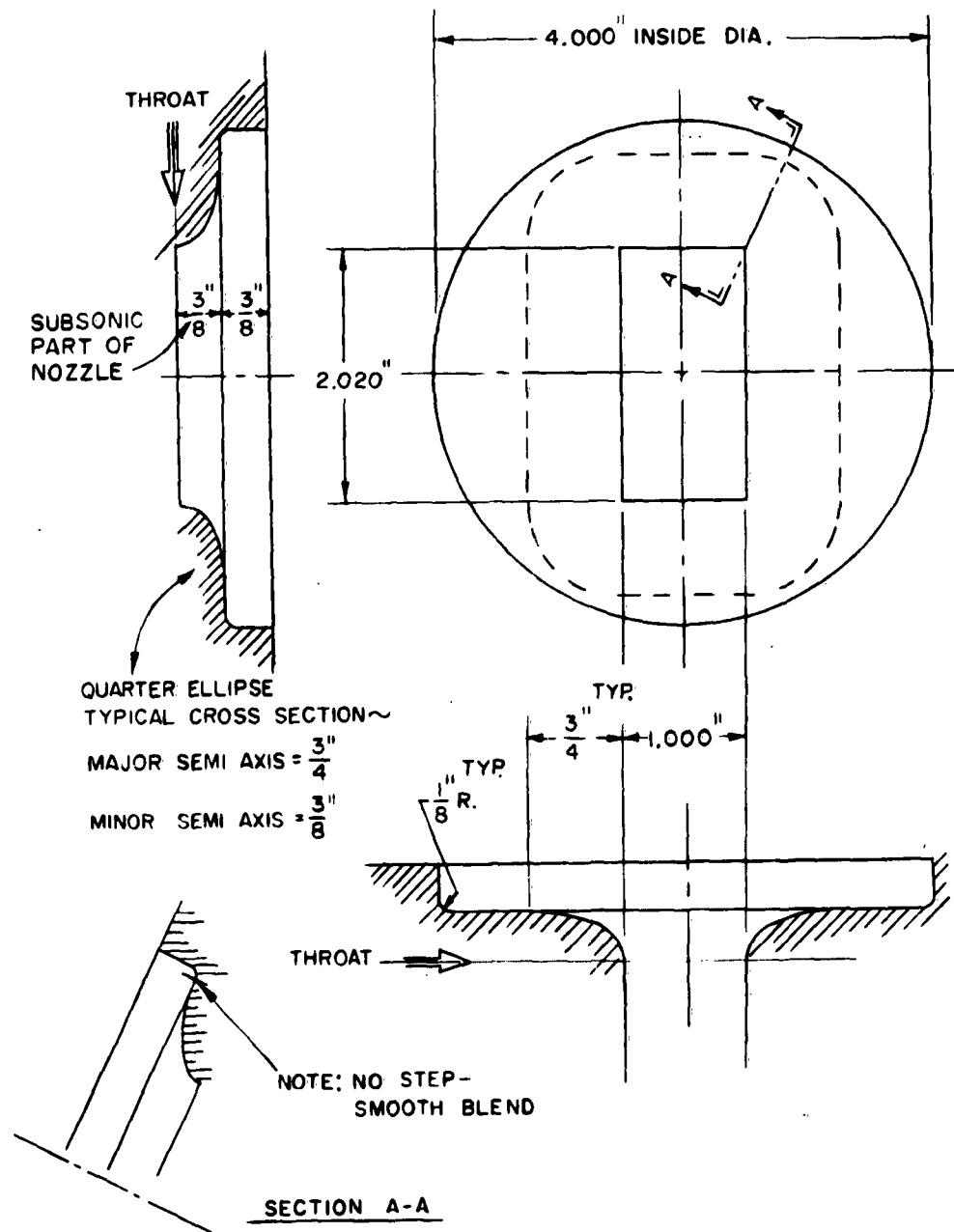


Figure 20. Contouring of Subsonic Part of Nozzle

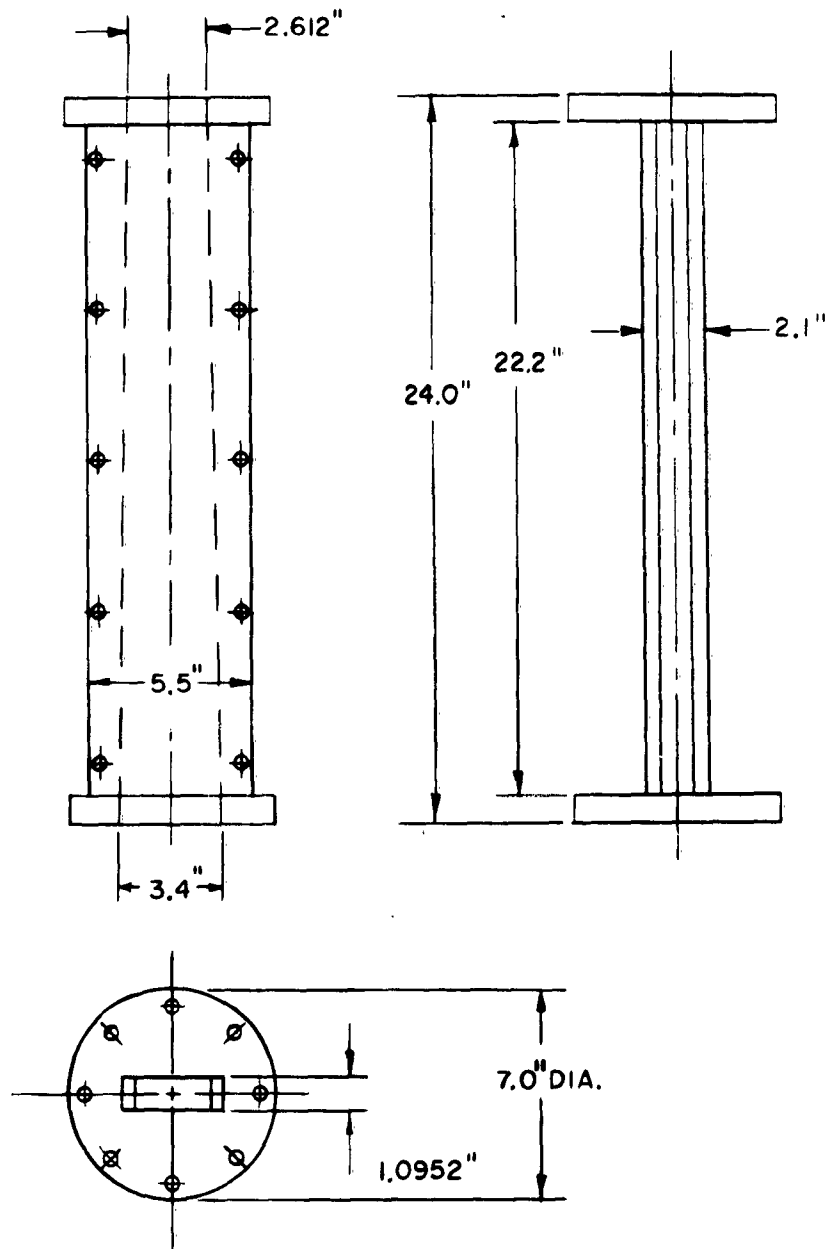


Figure 21. Transite "Test Sections" Used in Experiments

the height of the channel. From the general trend suggested by Figure 39 of reference 1, a value of 1.3 was chosen for the ratio of exit-to-entrance cross-section area of the test section, thus establishing the exit height as 3.4 inches. A straight line taper was used in diverging the height of the channel from 2.612 inches to 3.4 inches, see Figure 21.

To avert a possible choking condition that might develop towards the exit end of the test section as a result of not tapering two of the channel walls, a separate analysis was made to determine the extent to which the boundary layer displacement thickness will grow above its initial value of .0476 inches at the entrance to the test section (see Section 3.2.2). A 1/7th power law of velocity distribution in the turbulent boundary layer was employed in the analysis, which then yields a displacement thickness

$$\delta^* = \frac{1}{8} \delta \quad (3.18)$$

(p. 432 reference 10). Boundary layer thickness was computed from the relation (reference 11)

$$\delta^{5/4} = \frac{.302}{u_e^{5/2} (r^\beta \rho_e)^{5/4}} \int_0^x \left(\frac{u_e}{u_e} \right)^{1/4} u_e^{5/2} (r^\beta \rho_e)^{5/4} dx \quad (3.19)$$

where

$$\beta = \begin{cases} 0 & \text{for 2-dimensional flow} \\ 1 & \text{for 3-dimensional flow} \end{cases}$$

Since these relations apply to purely turbulent flow, it was necessary to first determine a fictitious distance ahead of the test section inlet, which will have a turbulent displacement thickness at the inlet equal to the previously computed laminar displacement thickness of .0476 inches. Integration of Equation (3.19)

was then continued past this fictitious distance to obtain the displacement thickness at the exit end of the test section. In this manner a value of

$$\delta^*_{T.S. \text{ exit}} = .12 \text{ inches}$$

was found for the turbulent boundary layer displacement thickness at the exit of the test section. Since this value is considerably less than half the width of the channel (.5476), it was not considered likely that the flow will be choked; this was later also confirmed experimentally.

An additional item of interest was the evaluation of the channel's wall temperature as a function of "running-time". The wall was considered a semi-infinite solid exposed to the flow of air whose static and total temperatures are 5850°R and 6750°, respectively (see Table II). Assuming a Prandtl number of .75, the recovery temperature is then

$$[T(x,t)]_{\text{recovery}} \quad T(0,\infty) = 6640^\circ\text{R}$$

With this boundary condition and the following assumed value of the heat transfer coefficient

$$h = .0225 \frac{\text{BTU}}{\text{ft}^2 \text{sec } ^\circ\text{R}}$$

wall temperatures were computed from the relation (p. 216, reference 12)

$$T(x,t) = T(0,\infty) \left[\text{erfc}\left(\frac{x}{2\sqrt{kt}}\right) - e^{\epsilon x} e^{\epsilon^2 kt} \text{erfc}\left(\frac{x}{2\sqrt{kt}} + \frac{\epsilon x}{\sqrt{kt}}\right) \right] \quad (3.20)$$

where it is assumed that $T(x,0) = 0$. In this relation

$$k = \text{diffusivity of solid material} = \frac{\lambda}{\rho c_p}$$

$$\lambda = \text{thermal conductivity, } \frac{\text{BTU}}{\text{ft sec } ^\circ\text{R}}$$

$$\rho = \text{density, lb}_m/\text{ft}^3$$

$$C_p = \text{specific heat, } \frac{\text{BTU}}{\text{lb}_m \text{ } ^\circ\text{R}}$$

and

$$\epsilon = \frac{h}{\rho C_p k}$$

Equation (3.20) was evaluated assuming the material of the semi-infinite slab to be quartz, for which (p. 5, reference 13)

$$\lambda = .221 \times 10^{-3} \frac{\text{BTU}}{\text{ft sec } ^\circ\text{R}}$$

$$C_p = .18 \frac{\text{BTU}}{\text{lb}_m \text{ } ^\circ\text{R}}$$

$$\rho = 137 \frac{\text{lb}_m}{\text{ft}^3}$$

The results obtained are shown in Figure 22. As is seen from this figure, a running time of about eight seconds is available before reaching the softening temperature of the wetted surface. Beyond this time interval the temperature is not expected to follow the curves shown in Figure 22 because of the surface effects that will take place (such as ablation, chemical reactions, etc.).

3.4 Supersonic Diffuser

Although not an essential component, supersonic diffusers are employed to (1) fix the location of the shock, and (2) reduce the total pressure loss.

The minimum ratio of diffuser throat-area to nozzle throat-area is given, for isentropic flow of an ideal gas, by [Equation (5.48), reference 3]

$$\left[\frac{A_{\text{diffuser}}^*}{A_{\text{nozzle}}^*} \right]_{\text{min.}} = \frac{1}{(P_{t2}/P_{t1})} \quad (3.21)$$

where P_{t1} and P_{t2} are stagnation pressures ahead and behind a normal shock

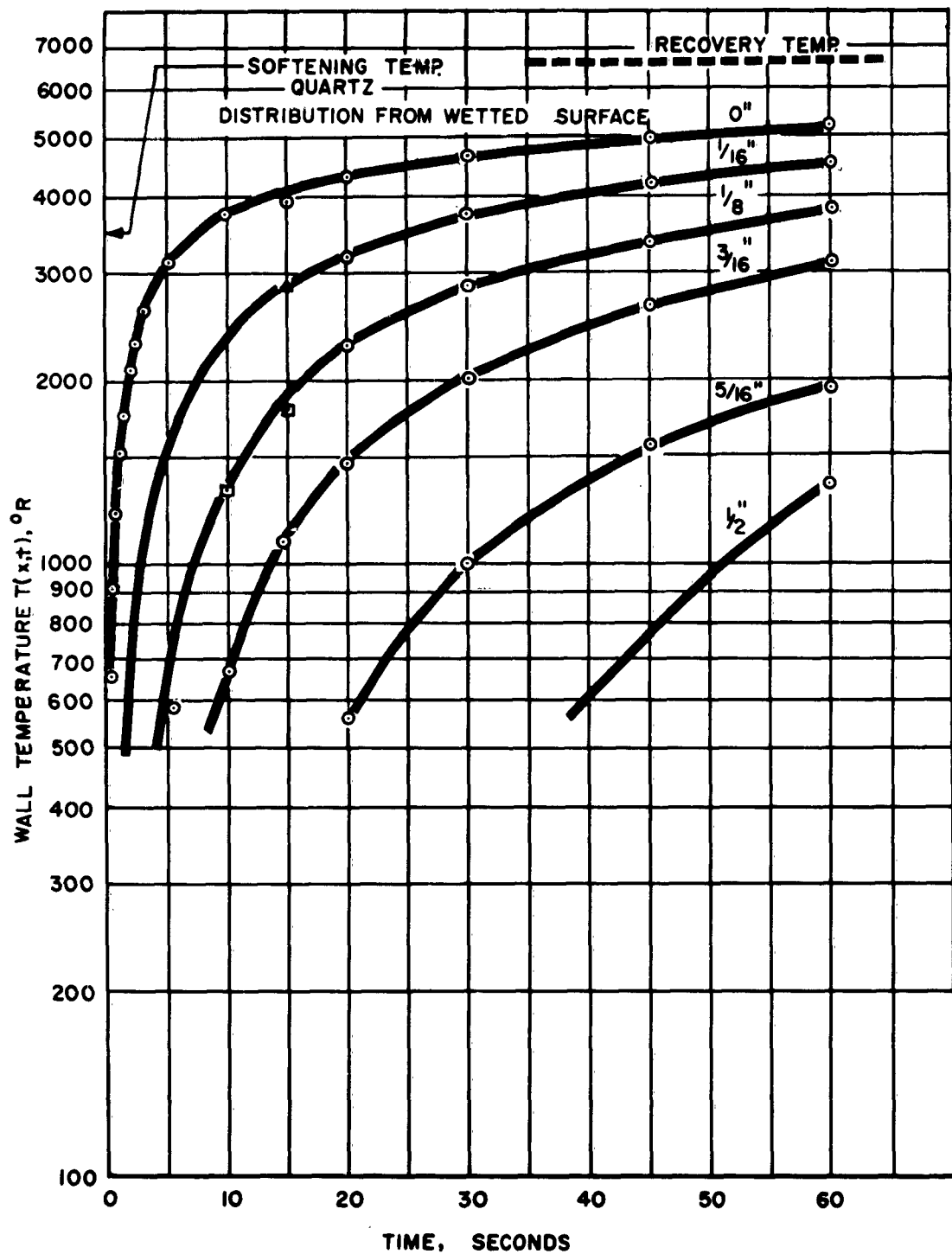


Figure 22. Temperature Distribution in a Semi-Infinite Slab of Quartz

corresponding to test section Mach number. Since the ratio (P_{t2}/P_{t1}) is a function of Mach number only (see, for example, reference 4), it is of great importance to establish the proper Mach number on which to base this ratio.

Now, the converging-diverging nozzle was designed to deliver a Mach 1.53 flow at the entrance to the test section (see Table II). Because of the diverging geometry of the test section (required for maintaining constant velocity flow), and also because of heat losses to the walls of the channel, the Mach number will increase towards the exit end of the test section, as both of these factors contribute toward reducing the local speed of sound. An analysis of these effects revealed that the exit Mach number would reach a value of about 1.67, thus calling for a minimum diffuser-throat to nozzle-throat area ratio of 1.15. A natural upper bound for this ratio would, of course, be

$$\left[\frac{A_{\text{diffuser}}^*}{A_{\text{nozzle}}^*} \right]_{\text{max}} = \frac{A_{\text{T.S. exit}}}{A_{\text{nozzle}}^*} = \frac{3.4 \times 1.0952}{2.02} = 1.84$$

A value of $\frac{A_{\text{diffuser}}^*}{A_{\text{nozzle}}^*} = 1.29$ was finally chosen as the "truer" minimum ratio, since the value 1.15 does not take into account boundary layer build-up along the walls. A value closer to the theoretical minimum (1.15) rather than the theoretical maximum (1.84) was chosen, as it would be much easier to enlarge the "second throat", rather than reduce its area, in case of a misjudgement.

Figure 23 shows the inside dimensions of the diffuser, where the height of the "second throat" is obtained as

$$\text{height of "second throat"} = 1.29 \frac{A_{\text{nozzle}}^*}{\text{width of T.S. (or diffuser)}} = 1.29 \times \frac{2.02}{1.0952} = 2.38 \text{ inches}$$

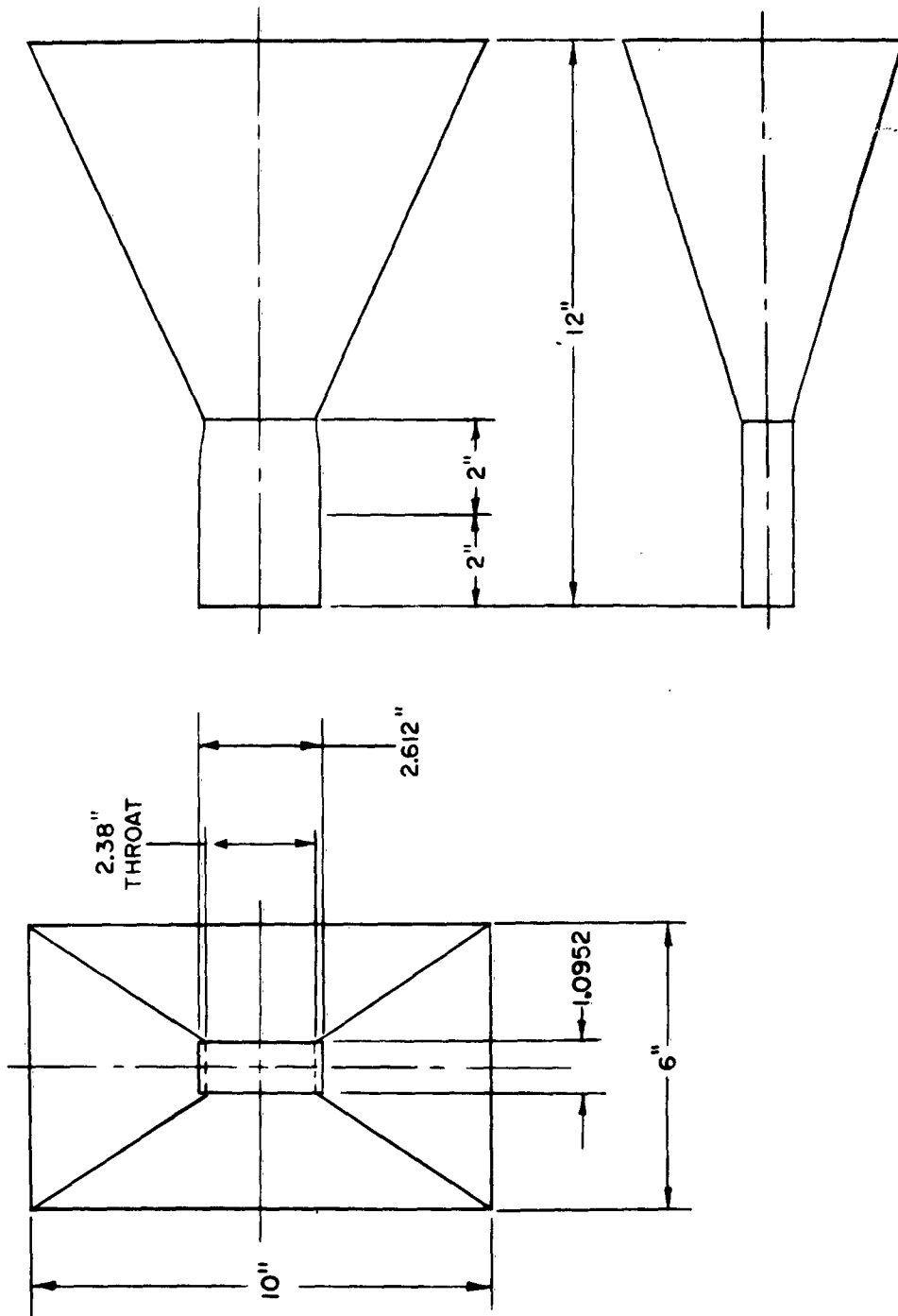


Figure 23. Inside Dimensions of Diffuser

4. ELECTRICAL DESIGN OF GENERATOR

4.1 Introduction

The basic requirement of the generator is the production of a linear traveling magnetic field to provide inductive interaction with the moving plasma. Theoretical considerations showed that the optimum velocity of the magnetic field for maximum power extraction would be one-half the plasma velocity and traveling in the same direction for an electrical slip of -1.

The method used to provide the linear traveling wave was a polyphase A.C. coil and generator combination. A three-phase device, rather than two-phase was chosen in this case since standing wave effects due to incomplete coil sections at the ends of the total coil would be minimized, and better utilization of the interaction length could thus be achieved.

Early in the development of the generator system, consideration had been given to the use of an excitation system using triggered switches and resonant circuits to produce slowly changed oscillation; however, this was soon discarded when it became obvious that the timing and synchronization precision required for proper polyphase operation would be totally unobtainable with the circuits contemplated.

The final method selected was continuous operation of the generator using a CW exciter. Since it was desired to obtain as large a magnetic field as practicable, consideration was given to the use of water-cooled copper coils placed on the face of a ferromagnetic substrate absorbing an input power of 13.5 KW, and delivering a calculated field strength of about 1000 gauss (see para. 4.4).

4.2 Transistorized Exciter

4.2.1 General Discussion

Because of the relatively high power level contemplated for the coil excitation, the high frequency (3 to 6 KC), the polyphase feature and finally, the low load impedance of the coil system, a high power precision three-phase generator using switching techniques was evolved.

As indicated, the power supply was composed entirely of semi-conductors in switching type circuits, as shown in Figure 24. All circuits operated at relatively low power levels up to the final output stage. The output stage was a half bridge with a split power supply, as shown in Figure 25. Because switching techniques were used, it was possible to incorporate a number of "one knob" controls and other features which offered highly flexible operation.

The output of the generator was, strictly speaking, three modified square waves into tuned circuit loads which eliminated the higher order harmonics. These were so related that the resultant current in the load was equivalent to a three-phase sinusoid. The portion of the circuit which created the three basic square waves and their relationship was termed a "three-phase square wave generator"*.

4.2.2 Clock Pulse Generator

One knob frequency control was obtained from a free running multi-vibrator circuit. The clock frequency was equal to $\frac{1}{t}$ where t is the total period of the multivibrator. Stability of the period was obtained by isolation diodes in series with the individual cross coupling RC timing networks and the opposite bases. When the diode was back-biased, stray leakages did not affect the time constant. A second diode across the base to emitter junction limited the reverse bias to a constant level and permitted more consistent turn-on characteristic of

* As used here, this denotes three individual square waves with a time relationship of 120° between their fundamental components.

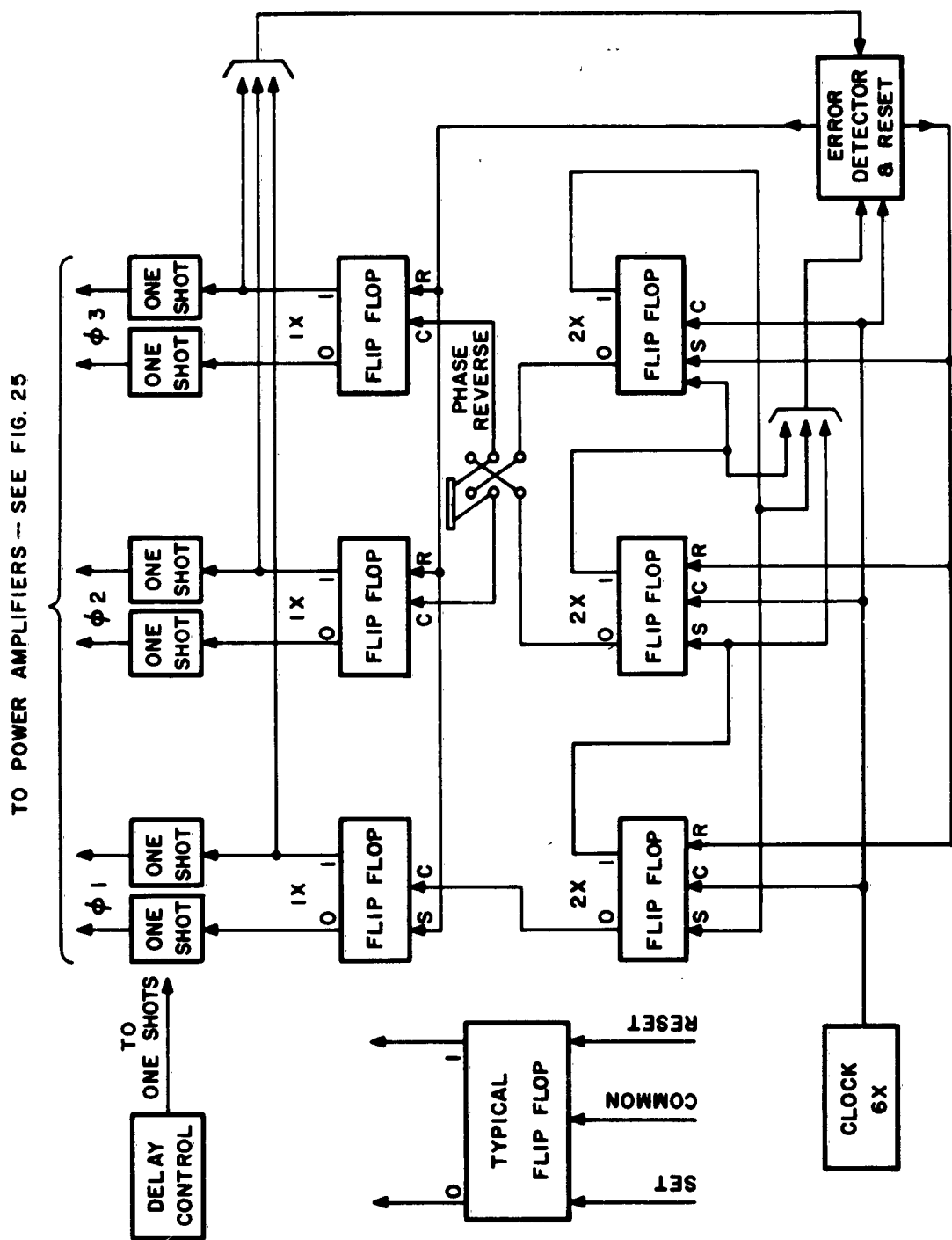


Figure 24. Block Diagram - Transistorized 3-Phase Generator

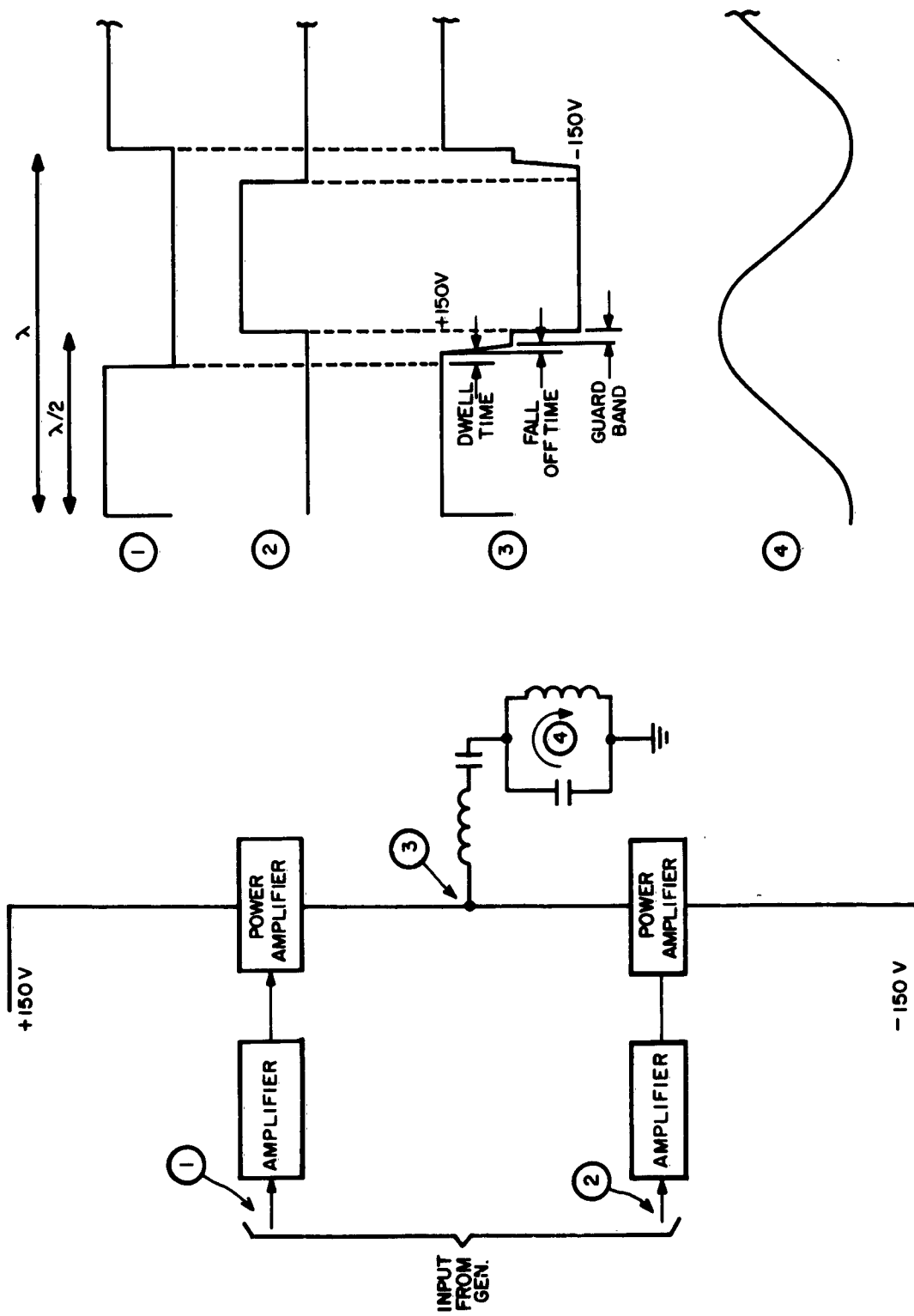


Figure 25. Block Diagram - Typical Transistorized Power Amplifier and Waveforms

the transistor. Once set, the frequency held constant for relatively long periods without constant monitoring. Short term stability (1 hour) was measured at better than 0.2%.

Isolation of the clock and its load was provided by wave-shaping amplifiers which converted the clock output to a rectangular pulse. The load received a constant signal whose frequency was set by the multivibrator. Changes in frequency, when desired, were easily obtained and did not upset the system by necessitating multiple frequency adjustment and checks.

NOTE: The clock frequency was six times the output frequency. This will become evident as the discussion progresses.

4.2.3 Square Wave Generator

Generation of the "three-phase square wave" was accomplished by use of flip-flops. Three of these flip-flops were connected as a ring of three counter, such that "A" drives "B", "B" drives "C", and "C" drives "A". Timing pulses from the clock were fed in parallel to all three flip-flops to establish timing control. By means of appropriate gating, the timing pulses and the drive of the ring flip-flops were arranged so that each of the flip-flops had an output every third timing pulse, equally displaced in time. With reference to any one flip-flop, an output was obtained at a frequency which was one-third of the clock frequency.

The square wave itself was created by placing each of the outputs of the ring counter into a binary divider. As the ring counter outputs were spaced in time, the square waves produced were also spaced in time. When the three square waves were observed in strict time relationship, a 120° relationship was evident, and its frequency was $1/6$ that of the clock frequency. Because of its digital nature, the phase relationship was explicitly defined.

Early in the design, the need for consistent phase sequencing and manual

control of phase reversal was recognized. It was also recognized that inherently, the flip-flops could "lock up" and the circuit become inoperative due to noise transients, or when power was initially applied. To prevent this condition, a circuit was incorporated to recognize a condition of "lock-up" or other phase malfunction and generated a signal which was gated into all six of the flip-flops, forcing them to return to the predetermined phase sequence. This action took place in the period between two clock pulses. Manual phase reversal was simply accomplished by use of a DPDT switch to switch the inputs to two of the binary dividers.

4.2.4 Control of Power Output - Guard Bands

The half bridge output stage shown in Figure 25 consisted of two transistors which were switched on and off which caused the output voltage to alternate between the plus and minus supplies. Since the power transistors were not perfect switches, when their base was switched off, considerable dwell and fall-off time could occur, which could result in a short circuit condition if the other transistor base were turned on at the same time. A guard band in time was provided, which allowed the transistor to be turned off a short time before the other was turned on. The resultant waveshape is shown in Figure 25.

Each of the binary outputs and its complement was fed to a one-shot multivibrator. The output was a rectangular wave, the width of which was adjusted to be less than that of the square wave. If the D.C. returns of the RC timing networks are brought to a common point, simultaneous control of the width of the rectangular output results. The fractional decrease in width provided the necessary guard band for the final amplifiers. Phase reference remained unchanged. Further reduction in the width of the rectangular pulse had the effect of reducing the power in the load because of the shorter period of conduction for each half-

cycle. Since the output load was a resonant circuit tuned to the fundamental frequency, phase and amplitude variations of the harmonic components were immaterial.

4.2.5 Final Power Output Stage

The complementary portions of the modified square wave were amplified separately for proper drive of the power output stage. Algebraic summation of the complementary square waves took place in the tuned circuit loads, and the resultant was the required three-phase sinusoid at the fundamental frequency. The transistors used for this application had ratings of 300 VDC breakdown, and 25 ampere current capability. Two of these units provided a switching capability up to 4.5 KW per phase at the fundamental frequency.

4.2.6 Circuit Performance

Experimental data on the completed generator showed that performance met or exceeded the initial design criteria. Operating at full rated load at room ambient temperature frequency stability measurements showed a total excursion of less than 5 CPS/hr. at 3 KC, or better than 0.16%. In this same period the total phase error was measured at less than 30 minutes of arc. No attempts were made to test under extreme temperature or environmental conditions.

4.2.7 System Problem

It was experimentally determined that the transistorized three-phase generator suffered a failure in its high power output transistors, due to high voltage transients which were apparently introduced by the plasma arc starter. Modifications were made to this supply which cut out all power to the unit during the arc starting period. Failures continued to occur, at a reduced rate, which were apparently caused by reactive coupling of RF transients from the arc starter. Because of these failures and the obvious non-reliability of the high power

transistor, the entire transistorized supply was eliminated and a rotating machine supply (motor/alternator system) was designed and built as described in Section 4.3.

4.3 Alternator Power Supply

4.3.1 General Requirements

A motor alternator power supply capable of delivering up to 15 KW at 3 to 6 KC power - three-phase, was designed and built to replace the transistorized equipment previously described. The design obviated the possibility of voltage transient breakdown in this equipment since moving contacts or semiconductors were not used in its design. The mechanical details of the system are described in Section 5.2.

4.3.2 Motor

The prime mover for the alternator was a 25 HP Reeves variable speed induction motor/pulley system, which provided electrically remote speed control. An automatic return to low speed upon de-energization was provided in order to prevent excessive pulley slip when started. Other portions of the motor electrical system are conventional.

4.3.3 Alternators

Three alternators, mounted linearly on a common jackshaft, provided the necessary high frequency three-phase output. These alternators have been developed quite recently by the Curtiss-Wright Corporation, principally for single phase use in induction heating. However, they are suitable for polyphase operation since they are synchronous. These units are Alexandersson-type induction alternators with both field and output windings on the stator. The rotor consists only of laminated, slotted iron and the output is derived by magnetic pole switching of the D.C. field to induce a voltage in the output windings.

The unloaded harmonic content is fairly large but is considerably reduced when the machines are operated into a tuned resonant load (i.e. the interaction coil system). The alternators are 60 pole machines, hence, shaft speeds are necessarily 4500 to 9000 rpm for 3 to 6 KC output. Field control for the alternators is obtained by a separate 28 VDC power supply, carbon pile regulators, and small transformer/rectifiers for output voltage feedback.

4.4 Interaction Coil System

4.4.1 General Remarks

The interaction coils used for excitation and power extraction were designed to produce a linear traveling wave in the direction of the plasma velocity. The velocity of magnetic field propagation along the coil test section structure must be such that it is always less than the plasma velocity in order that power be extracted (i.e. the slip is negative). In the case under discussion, the plasma velocity is relatively small (about 1790 m/sec). For most efficient power transfer the slip becomes -1 as has been shown in the theoretical report. Hence, it becomes necessary to provide a traveling wave magnetic field with a group velocity of 895 m/sec for maximum output. This group velocity depends on the mechanical wavelength of the coil segments and the operating frequency

$$v_b = (\lambda_b)(f_o) \quad (4.1)$$

Due to the compact geometry required, and the necessity for water cooling, the mechanical wavelength of the coil segment was limited to a practical maximum of 6.0 inches, (0.152 m), in order to obtain a channel length of 3 electrical wavelengths. Likewise the upper operating frequency was limited to a maximum of about 3 KC at full power to prevent excessive core heating in the laminated iron substrate. Thus an operating group velocity of only about 460 m/sec was obtained,

corresponding to a slip of approximately -3. It can be shown theoretically (see reference 1) that the extracted power from the plasma at the lower frequency would be 0.75 times the maximum value corresponding to a slip of -1. For practical considerations, the slip of -3 was selected as a working value.

4.4.2 Construction

The coil laminated substrates were constructed of 8 mil hypersil strips, approximately 22 inches long, 4.5 inches wide and 2.5 inches deep. Shallow slots were transversely milled and special water-cooled conductors made of OFHC copper 0.25 inch diameter and a wall thickness of 3/64 inch, were bonded to the substrate. The conductors were arranged in a typical three-phase spatial geometry; a simplified schematic of this conductor arrangement is shown in Figure 26. Each coil segment consisted of three turns, and represented a half wavelength of one phase. The return loops were made outside of the iron and test section vicinity in order to minimize fringing flux. For the same reason, the lateral conductors of the coils were extended with a 1.5 inch overlap on each side of the active area of the test section.

Two bars were constructed to fit above and below the test section, the winding on one coil being of course, a mirror image of the winding on the other. The resultant gap is thus as small as possible in order to maintain a minimum reluctance to the magnetic field.

It is interesting to note that it is allowable to have complete physical separation of the two coil sections without a return magnetic path since the algebraic sum of the flux entering and leaving each section is at all times zero.

4.4.3 Cooling

The cooling water system for the coils was optimized with maximum practical manifolding and flow rates. With the flow rate thus obtained (approximately

6 gpm) a maximum input power of 13.5 KW was considered allowable without excessive water temperature rise. The iron core was not cooled, and did exhibit a temperature rise of approximately 20°C over ambient, at 3 KC and full power. This core loss was larger than anticipated but not unreasonable for 3 KC operation. Operation at significantly higher frequencies would be possible with reduced power input.

4.4.4 Operation

In operation, each coil section was tied in series with its counterpart on the opposite side of the test section, and tuned to resonance with special high frequency capacitors. A loaded Q of between 3 to 5 was obtained for the three phases, and for a line current of 30 amperes, resulted in a traveling magnetic field strength of 157 gauss (typical). The large discrepancy between calculated and measured Q was ascribed to core loss.

4.4.5 Instrumentation Facilities

Determination of circulating current in each phase was made with standard Weston transformers operating at a 100:1 current ratio. The output terminals of the transformers were attached to a non-inductive 1.00 ohm resistor in order to obtain an output voltage proportional to the coil current.

A tertiary winding of fine wire was bonded to the top of each phase winding of the upper coil section, for use with the power monitoring matrix described in Section 6.2.

5. MECHANICAL DESIGN OF GENERATOR

5.1 Introduction

The equipments which were largely of a mechanical nature are discussed in this section, with emphasis placed upon performance capabilities tailored to the requirements of this program. Mechanical and electrical design of the generator are complimentary. Additional capabilities for flexible or increased operating performance are inherent, as will be described.

5.2 Motor/Alternator Set for Three Phase Coil Power

The requirement for three-phase coil power was met by the design and construction of a high speed motor/alternator set. This set is capable of 5 kilowatts per phase at frequencies up to 6000 cycles per second.

Three separate synchronous induction alternators were modified for through shaft, in line coupling and mounted co-linearly with a jack shaft which was connected by flexible couplings. The jack shaft was driven through a V-belt drive consisting of 10 parallel belts, by a 25 horsepower variable speed, electric motor drive. The alternator shaft speed has usually been held at 4500 rpm, which corresponds to an alternator frequency of 3000 cps. However, the machine has been tested as high as 8200 rpm or approximately 5500 cps.

Although this machine is relatively straightforward, a major vibration problem arose during its design. A shafting configuration such as the one employed is a spring-mass system. This should be investigated for lateral and torsional resonant frequencies, since the shaft complex has a number of inertias (the alternators, drive pulley and reflected inertia from the drive motor) with a number of compliant shafts connecting the inertias. A cursory check usually indicates that the resonant frequencies are considerably out of the operating

range of the machine. This was the case for lateral vibrations. However, in the initial layout of the machine, it was determined that two of the three torsional resonances occurred at approximately 6000 rpm. The sequence of this in line arrangement (from left to right) was as follows: Alternator number one (inertia J_1) was connected by a shaft (with stiffness K_1) to the driven pulley (inertia J_2). This pulley was in turn, connected by a second shaft (with stiffness K_2) to alternator number two (inertia J_3), and finally, the third shaft (stiffness K_3) was connected to alternator number three (inertia J_4). It was determined that J_1 , K_1 and J_2 , J_3 and J_4 combined, were torsionally resonant at 6000 rpm. A second system, also resonant at 6000 rpm, was the result of the combined inertias of alternators J_3 and J_4 connected to the pulley J_2 through shaft K_2 .

In practice, a good design solution to this problem would be to simply stiffen the alternator shafts by increasing their diameters. This would decrease inertias so as to raise resonant speeds above the operating range of the machine. In this case, the alternator units could not be economically redesigned for larger rotor shafts. Instead, couplings were designed soft and a small flywheel was added, thus pulling the two 6000 rpm resonances down to about 3200 rpm. The result is a mild shudder as the machine comes up to speed, but extremely smooth operation occurs in its normal running range.

Operating frequencies up to 15 KC are practical at reduced loads with the present machine. Additional capabilities (to 30 KC) may be attained by the use of newer alternators, which have been recently developed. These units can be readily substituted on the existing machine.

5.3 Cooling Water System

This system was designed to meet cooling water requirements for the torch and generator components and provides a continuously rated delivery of 400 gpm

at two operating pressures of 100 and 200 psia, respectively. The closed water supply system utilizes a 550 gallon surge tank and is driven by a 75 HP water pump. Flow meters and metering valves are provided for regulation at all quick disconnect attachment points to the torch, plenum and mixing chamber, supersonic nozzle, power extraction coils, arc starter leads, and main input D.C. power leads. High pressure flexible hose connections are made in all cases.

5.4 Vacuum Dump System

The vacuum tank used for the blow-down system is eight feet in diameter by forty-eight feet long with a volumetric capacity of 2400 cubic feet, at atmospheric conditions. The time required to evacuate it to 0.05 atmospheres is seventeen minutes with its 25 HP vacuum pump, which is shown in Figure 7. A 3' diameter extension flange projects into the laboratory proper, to which the exit flange of the test section is attached. The tank material is steel and it is of combined welded and riveted construction. A second or standby vacuum tank of 2000 cubic feet capacity is available, which would nearly double the system capacity.

5.5 Gas Supply System

The dry nitrogen gas supply system has a storage capacity of 20,000 cubic feet at atmospheric conditions and is housed in a separate services shelter. Six nitrogen cylinders are manifolded through a special high flow rate reducer to provide a surge source of gas, which is controlled through the console. Oxygen is provided in a similar manner to provide the required mass flow rates. This gas supply system provides a mixture of 80% N_2 at 300 psia and 140 scfm, and 20% O_2 at 300 psia and 40 scfm to simulate operation of the facility on air. The equipment is shown by Figure 4.

5.6 Test Section

Four test section configurations have been designed and built for this operation. The first unit constructed was made entirely of fused quartz at a working length of 22", with a constant rectangular 1.095" high by 2.612" wide internal dimensions by 24" overall length at a nominal $\frac{1}{8}$ " slab thickness. The seven inch diameter flanges were fused to this section at both ends. The second type which is expendable, utilized transite as the basic material and was machined from rectangular slabs. These were in turn, bonded at all joints to provide vacuum seal. Re-usable aluminum flanges were incorporated at the entrance and exit sections. Three versions of this transite section were designed. The first unit was of constant cross-sectional area, whose physical dimensions were similar to those of the quartz section. The second version maintained the constant vertical height of 1.095" and its width at the entrance remained 2.612", but a straight taper was maintained along the 24" length to an exit width of 3.40 (see Figure 21). The upper and lower slabs were built in two thicknesses, which were $\frac{1}{2}$ " and $\frac{3}{4}$ " respectively. The purpose of the thicker version was to provide increased running time due to additional wall material, prior to burn-out or destruction of the section.

6. INSTRUMENTATION

6.1 Introduction

The instrumentation developed for this program has been designed to provide initial calibration of the active equipment prior to operation and to record the variable parameters which occur during experimental testing.

6.2 Recorded Test Data

The instrumentation read-out methods selected for recording essential information during a test run combines the use of a recording oscillograph for electrical measurements, and a time synchronized photographic recording of manometric measurements.

6.2.1 Electrical Measurements

The electrical measurements taken during a typical test run consisted of (1) plasma torch voltage (1000 volts full scale), (2) plasma torch current (4000 amperes full scale), (3) circulating current, I_L in phase I (typical) of power extraction coils (1000 amperes full scale), (4) unnullled voltage component (e_g) due to MHD action as described in Section 6.5 (sensitivity adjustable from approximately 100 millivolts full scale for a qualitative run; to 100 volts full scale, quantitative; the minimum quantitative sensitivity obtained being 1.0 volt full scale), (5) electrical measurement of torch, nozzle, and plenum cooling water differential temperature, obtained from back-to-back chromel p-alumel thermocouples (full scale 1.5 millivolts corresponding to a differential temperature of 37.5°C), (6) phase angle measurement of the phase angle between I_L and e_g derived from a metering output of a commercial precision phase meter (full scale 180°). The recording oscillograph used for the six measurements above was a Sanborn model 350 with high gain plug-in amplifiers. The phase meter was an Advance Electronic Corp. model 405.

In addition to the recorded data, visual monitoring was made of the constant excitation frequency, which was displayed on a digital counter. Pre-test nulling of the phase monitoring matrix was simplified by the use of an oscilloscope.

6.2.2 Manometric Measurements

Four mercury manometers connected to measure plenum pressure, test section entrance and exit pressure, and dump tank pressure were photographed with an automatic 35 mm camera at one to two second intervals during the test run. See Section 6.4 for results.

The sweep second hand of a standard electric clock was synchronized with the timing marker of the recorder. It was placed next to the manometer board in order to appear in the photographs. Gas flow measurements and the oscilloscope trace of the phase monitoring matrix were included in the photographic record.

6.3 Stagnation Enthalpy Measurements

6.3.1 Introduction

The method used in obtaining the stagnation enthalpy of the plasma was to measure the rate of temperature rise at the stagnation point of an axi-symmetric calorimeter-type probe, then compare the experimental heat transfer rate thus obtained with corresponding theoretical predictions which involve the stagnation enthalpy, and thus deduce the latter.

Assume the calorimeter to be made of good thermally conducting material and to be sufficiently small so as to always have essentially uniform temperature. If the calorimeter, assumed to be cylindrically shaped, is embedded concentrically in an axi-symmetric larger body with one end flush with the surface of the larger body at its stagnation region, then the rate of heat transfer to the calorimeter per unit cross-sectional area of the cylinder is given by

$$q = \rho_e C_{p,e} \tau \frac{\partial T_e}{\partial t} \quad (6.1)$$

where $\frac{\partial T_e}{\partial t}$ is the measured temperature rise per unit time (all symbols are defined in NOMENCLATURE). This relation assumes that none of the heat absorbed by the calorimeter from the plasma is given off, thus pointing to the need of selecting a good insulating material from which to fabricate the larger axis-symmetric body.

6.3.2 Theoretical Heat Transfer Rate To Calorimeter

The problem of stagnation point heat transfer at high temperature on a body of revolution at zero angle of attack was treated by Fay and Riddell (reference 14). Their equation for stagnation point heat transfer, for a Lewis number of one, is

$$(q)_{LE^*=1} = \frac{.76}{(\bar{P}_R)^{.6}} \left(\frac{\rho_w \mu_w}{\rho_e \mu_e} \right)^{.4} \left(\rho_e \mu_e \frac{du_e}{ds} \right)^{1/2} (h_{se} - h_w) \quad (6.2)$$

where (\bar{P}_R) is the average Prandtl number evaluated for conditions at the wall and at the edge of the boundary layer.

For Lewis number other than one

$$\frac{q}{q_{LE^*=1}} = 1 + \left[(LE^*)^{\Phi} - 1 \right] \frac{h_D}{h_{se}} \quad (6.3)$$

where $\Phi = .52$ for equilibrium flow

$\Phi = .63$ for frozen flow with recombination at the wall

The quantity h_D is the average atomic dissociation energy times the atom mass fraction in the external flow:

$$h_D = \sum_{\text{atoms}} C_{i,e} (-h_i^0) \quad (6.4)$$

where h_i^0 is the heat evolved in the formation of oxygen or nitrogen atoms at

zero degrees absolute per unit mass, and $C_{1,e}$ is the mass fraction of oxygen or nitrogen atoms.

Velocity gradient along a generator of an axi-symmetric body at the stagnation point is found from the relation (reference 15)

$$\frac{du_e}{ds} = \frac{u_\infty}{R} \sqrt{\frac{\rho_\infty}{\rho_{e,s}} \left(2 - \frac{\rho_\infty}{\rho_{e,s}}\right)} \quad (6.5)$$

where (u_∞) and (ρ_∞) are the velocity and density of the free stream ahead of the detached shock wave, respectively, and R is the radius of curvature of the body at the stagnation point.

6.3.3 Stagnation Enthalpy Probe

A perspective cut-away view of the probe used in measuring the stagnation enthalpy of the plasma is shown in Figure 27. A (.100) inch diameter (.200) inch long cylindrical calorimeter was embedded in a Boron Nitride adaptor, which in turn, was fitted in a stainless steel housing as shown in Figure 28.

Probe and housing were cooled by injecting nitrogen through a series of 1/16 inch diameter holes drilled through to a common supply line. The rod to which the probe was fastened could be moved in-and-out of the plasma-jet by a simple, spring actuated, mechanism.

The procedure of obtaining data with this probe involved the following steps:

- 1) Cool probe in retracted position until steady state operation of the plasma-jet is obtained;
- 2) Insert probe into plasma-jet, keeping the (nitrogen) coolant on until calorimeter reaches a steady temperature;

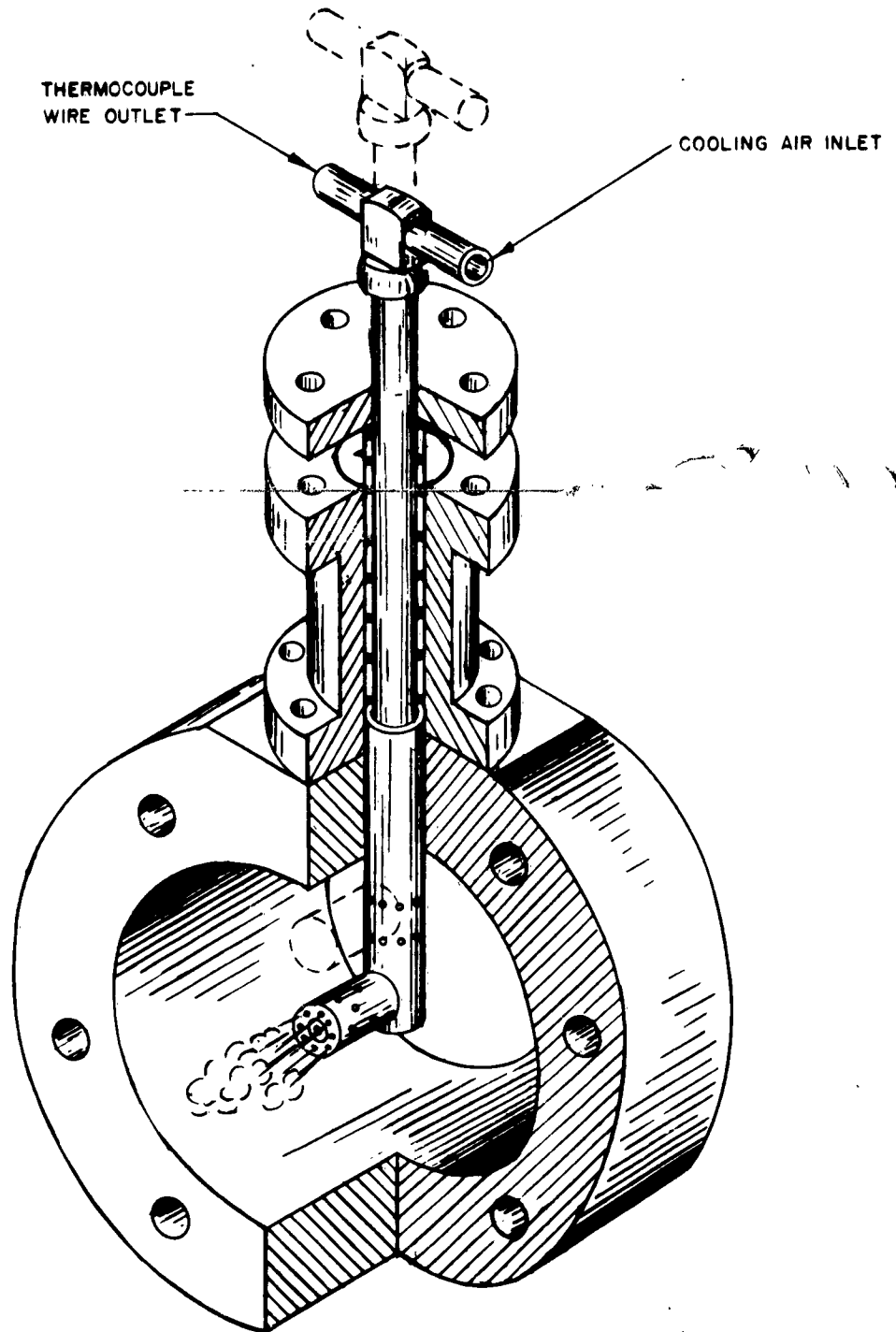


Figure 27. Perspective Cut-Away View of Stagnation Enthalpy Probe Assembly

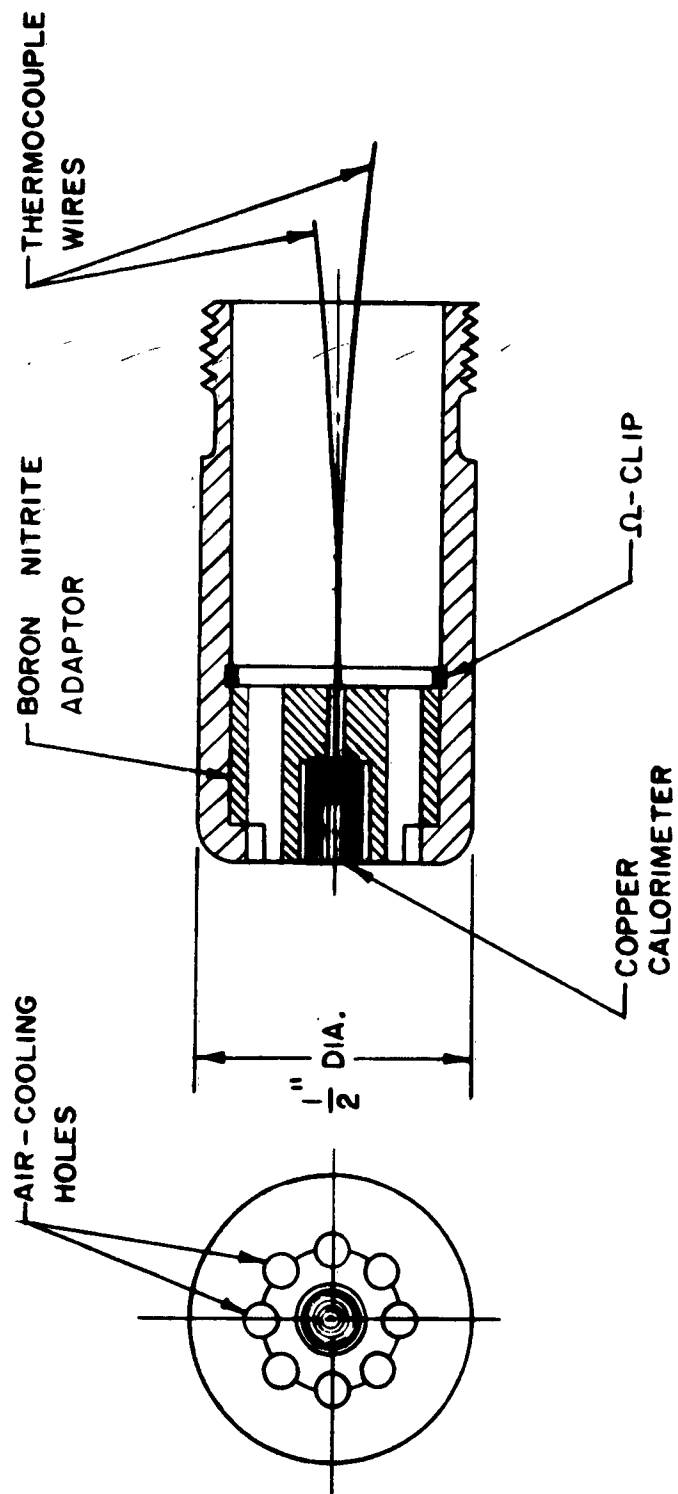


Figure 28. Calorimeter-Type Stagnation Enthalpy Probe

- 3) Shut coolant off for a brief period of time during which the temperature is permitted to rise to some level below the melting point of the copper calorimeter;
- 4) Turn coolant on and retract probe from main plasma-jet.

6.3.4 Sample Computation of Stagnation Enthalpy

Suppose the probe reaches a steady temperature of 700°R when inserted into the plasma-jet with the coolant on. Also, suppose the measured stagnation pressure is 1.0 atmospheres. Then,

$$h_w = c_p T_w = \left(.24 \frac{\text{BTU}}{\text{lb}_m^{\circ}\text{R}} \right) (700^{\circ}\text{R}) = 168 \frac{\text{BTU}}{\text{lb}_m}$$

With the aid of Reference 6, $Z = 1.0$; hence

$$\rho_w = \frac{P_w}{RT_w Z} = \frac{(1 \text{ atm}) \left(68,200 \frac{\text{lb}_m}{\text{ft}^2 \text{ sec}^2 \text{ atm}} \right)}{\left(1715 \frac{\text{ft}^2}{\text{sec}^2 \text{ }^{\circ}\text{R}} \right) (700^{\circ}\text{R}) (1)} = .057 \frac{\text{lb}_m}{\text{ft}^3}$$

Also, with the aid of Equation 68 and Figure 8 of reference 9

$$\mu_w = 1.505 \times 10^{-5} \frac{\text{lb}_m}{\text{ft-sec}}$$

It is next necessary to assume a value for the stagnation enthalpy and proceed to evaluate the heat transfer rate with the aid of Equations (6.2) and (6.3). The result obtained will then be compared with the measured heat transfer rate as evaluated with the aid of Equation (6.1). If the two answers disagree, other values for the stagnation enthalpy will have to be selected until agreement is reached.

Assuming the design value to be the true value of the stagnation enthalpy,

$$h_{s,e} = 2925 \frac{\text{BTU}}{\text{lb}_m}$$

(see Table II), hence

$$\rho_e = .0053 \frac{\text{lb}_m}{\text{ft}^3}$$

and with the aid of Reference 9 (since $T_e = 6750^\circ\text{R}$, see Table II),

$$\mu_e = 5.84 \times 10^{-5} \frac{\text{lb}_m}{\text{ft-sec}}$$

From Figure 10, Reference 9, Prandtl number for the average condition between the wall and the edge of the boundary layer is

$$\overline{(Pr)} = .77$$

For a flat-faced circular cylinder whose axis is parallel to the free-stream velocity, a good approximation for the radius of curvature at the stagnation point for purposes of evaluating $\frac{du_e}{ds}$ from Equation (6.5) is (reference 16)

$$R = 4r \quad (6.6)$$

where (r) is the radius of the cylinder. Substituting the free-stream values from Table II into Equation (6.5), there is obtained, with the aid of Equation (6.6) and Figure 29

$$\begin{aligned} \frac{du_e}{ds} &= \frac{5440}{(4 \times \frac{1}{4} \times 1/12)} \sqrt{\frac{.00182}{.0053} \left(2 - \frac{.00182}{.0053} \right)} \\ &= 49,500 \text{ sec}^{-1} \end{aligned}$$

Stagnation point heat transfer for a Lewis number of unity can next be evaluated by substituting the above quantities into Equation (6.2). Thus,

$$\begin{aligned} (q)_{LE} &= \frac{.76}{(.77)} \cdot .6 \left[\frac{(.057) (1.505 \times 10^{-5})}{(.0053) (5.84 \times 10^{-5})} \right]^{.1} \sqrt{(.0053) (5.84 \times 10^{-5}) (49,500) \times (2925-168)} \\ &= 338 \frac{\text{BTU}}{\text{ft}^2\text{sec}} \end{aligned}$$

Correction for Lewis number different from unity is obtained with the aid of Equations (6.3) and (6.4). For the stagnation condition given in Table II there is obtained from Figure 11, Reference 9,

$$L_E \# = 1.25$$

Also, for the same stagnation condition, essentially only oxygen is present in dissociated form (reference 6), and has a mass fraction ratio of

$$C_{o,e} = \frac{.13}{1.991} = .0655$$

The heat of formation of oxygen atoms is (p. 1704, reference 17)

$$h_1^o = \frac{59,200}{16} \frac{\text{grcal}}{\text{gr}} \times 1.8 \frac{\text{BTU/lb}_m}{\text{grcal/gr}} = -6680 \frac{\text{BTU}}{\text{lb}_m}$$

Substituting into Equation (6.4)

$$h_D = .0655 \times 6680 = 435 \text{ BTU/lb}_m$$

Hence, for flow in thermodynamic equilibrium

$$\frac{q}{q_{LE\#=1}} = 1 + (1.25)^{.52} - 1 \times \frac{435}{2925} = 1.0183$$

and

$$q = 1.0183 \times 338 = 343 \frac{\text{BTU}}{\text{ft}^2\text{sec}}$$

The correction due to Lewis number not equal to unity is seen, in this case, to be less than 2 percent.

Referring back to Equation (6.1) for comparison with measured rate of heat transfer, and assuming the calorimeter to be of pure copper for which

$$C_{p,c} = \text{specific heat of copper} = .106 \frac{\text{BTU}}{\text{lb}_m^{\circ}\text{R}}$$

$$\rho_c = \text{density of copper} = 540 \frac{\text{lb}_m}{\text{ft}^3}$$

there is obtained

$$q = .860 \frac{\partial T_c}{\partial t} \quad \frac{\text{BTU}}{\text{ft}^2 \text{sec}}$$

($\frac{\partial T_c}{\partial t}$ in $\frac{^{\circ}\text{R}}{\text{sec}}$), where it was assumed that the height of the cylindrically-shaped calorimeter is $\tau = .015$ ft (.180 inches).

The anticipated rate of temperature rise in the copper calorimeter is, therefore, for the above case,

$$\frac{\partial T_c}{\partial t} = \frac{343}{.860} = 400 \frac{^{\circ}\text{R}}{\text{sec}}$$

Assuming this rate to be more or less constant until the calorimeter reaches approximately 1700°R (the melting point of copper is 2440°R) then, since the initial temperature of the calorimeter prior to shutting off the cooling gas was assumed to be 700°R , the allowable running time is, approximately,

$$\Delta t = \frac{1700-700}{400} = 2.5 \text{ seconds.}$$

6.3.5 Total Enthalpy of a Perfect Gas in Isentropic Flow

If the plasma jet could be regarded as a thermally and calorically perfect gas flowing isentropically through the converging-diverging nozzle, the following simple analysis could be employed to find its total enthalpy: the mass flow rate is given by

$$m = m^* = \rho^* u^* A^*$$

where superscript (*) refers to conditions at the throat. Now

$$u^* = a^* = \sqrt{\gamma R T^*}$$

$$p^* = p_{\text{total}} \left(\frac{2}{\gamma+1} \right)^{\frac{\gamma}{\gamma-1}}$$

and

$$T^* = T_{\text{total}} \left(\frac{2}{\gamma+1} \right)$$

where subscript (total) refers to stagnation condition. Substituting above, there

is obtained, with the aid of the equation of state $P^* = \rho^* RT^*$.

$$\frac{m}{A^*} = \frac{P^*}{RT^*} \sqrt{\gamma RT^*} = P_{\text{total}} \left(\frac{2}{\gamma+1} \right)^{\frac{\gamma}{\gamma-1}} \sqrt{\frac{\gamma}{RT^*}}$$

Hence

$$\frac{m}{A^* P_{\text{total}}} = \left(\frac{2}{\gamma+1} \right)^{\frac{\gamma}{\gamma-1}} \sqrt{\frac{\gamma(\gamma+1)}{2 RT_{\text{total}}}}$$

or

$$\frac{m}{A^* P_{\text{total}}} = \left(\frac{2}{\gamma+1} \right)^{\frac{\gamma+1}{2(\gamma-1)}} \left(\frac{\gamma}{RT_{\text{total}}} \right)^{\frac{1}{2}}$$

Thus, by measuring the pressure in the plenum chamber and the total mass flow rate through the nozzle (both of these quantities can be measured rather accurately), stagnation temperature can be computed as shown above and the stagnation enthalpy evaluated from the relation $h_{\text{total}} = C_p T_{\text{total}}$. Numerical values thus obtained can merely serve as approximations and as a guide to the results obtained by the probe described in Sections 6.3.3 and 6.3.4. This is so because of the stringent conditions imposed in the above analysis and also because of the uncertainty in the proper choice of numerical values for γ and C_p .

6.4 Pressure Measurements

In the runs carried out to date, pressure measurements were taken at the following four locations:

- 1) In the plenum chamber (P_{total})
- 2) At the entrance to the test section ($P_{\text{T.S. entr.}}$)
- 3) At the exit from the test section ($P_{\text{T.S. exit}}$)
- 4) In the large vacuum tank ($P_{\text{vac. Tank}}$).

With these pressure measurements, it was possible to

- a) Ascertain that $M \approx 1.53$ was established at the entrance to the test

- section (from P_{total} and $P_{\text{T.S. entr.}}$) prior to collection of data;
- b) that no shocks occurred in the test section (from $P_{\text{T.S. entr.}}$ and $P_{\text{T.S. exit}}$), and
 - c) evaluate the maximum available running time from the driving pressure-gradient point of view (from P_{total} and $P_{\text{Vac. Tank}}$).

It might be added here that structural failure of the uncooled test section, rather than limitations in the vacuum tank capacity is what has governed the maximum available running time to date.

6.5 Power Monitoring Matrix

6.5.1 General Discussion

The power monitoring matrix was designed to allow the measurement of a small extracted power in the presence of a much larger excitation power. In order to accomplish this, a technique was evolved to permit the nulling of voltage components due to incident power, and thus permit a high recording sensitivity.

6.5.2 Theoretical Considerations

In an equipment of this type extracted power may be measured at the coil terminals by the method explained below. Let the generator impedance per phase in the quiescent state,

$$Z_L = R_L + j X_L \quad (6.7)$$

NOTE: Standard engineering sign and symbol conventions are used here.

An additional component occurs when a moving fluid (the plasma) is added

$$Z_g = R_g + j X_g \quad (6.8)$$

where the sign of R_g is negative for negative slip (a generator).

In the case at hand no net power is produced, and in fact

$$R_L \gg R_g \quad (6.9)$$

Hence, an excitation device producing net power is necessary, such that

$$I_L (Z_L + Z_g) = E_T \quad (6.10)$$

where $E_A = 0$

We wish to measure the power extracted from the plasma

$$P_g = I_L^2 (R_g + j X_g) = I_L^2 Z_g \quad (6.11)$$

in the presence of driving power

$$P_D = I_L^2 (R_L + j X_L) = I_L^2 Z_L \quad (6.12)$$

where $\text{Re}(P_g) < \text{Re}(P_D)$

Referring to Figure 29 consider the total terminal voltage (e.g. phase 1 to ground in a three-phase star)

$$E_{T1} = I_{L1} R_{L1} + j \omega [I_{L1} L_1 + I_{L2} M_{2,1} + I_{L3} M_{3,1}] + E_{p1} \quad (6.13)$$

the complex power extracted in this phase may be determined simply since

$$P_{g1} = I_{L1} (E_{p1}) \quad (6.14)$$

the problem now becomes one of eliminating the undesirable terms from E_T .

$$-j \omega (I_{L1} L_1 - I_{L2} M_{2,1} - I_{L3} M_{3,1})$$

the term may be synthesized simply by introducing appropriately phase-shifted and amplified voltage components derived from the various phase currents. It might likewise, be supposed that a synthetic term $-I_{L1} R_{L1}$ could be introduced; however, in the practical case R_L does not remain constant and large errors would result by assuming that it does.

A technique to avoid this limitation has been utilized in the final device. Here a tertiary winding wound directly on the primary coils of each phase with a 1:1 relationship is connected to an infinite impedance detector. Since a potential only is detected in this winding, the terminal voltage is given by

$$E_{T1}^i = E_{T1} - I_L R_L \quad (6.15)$$

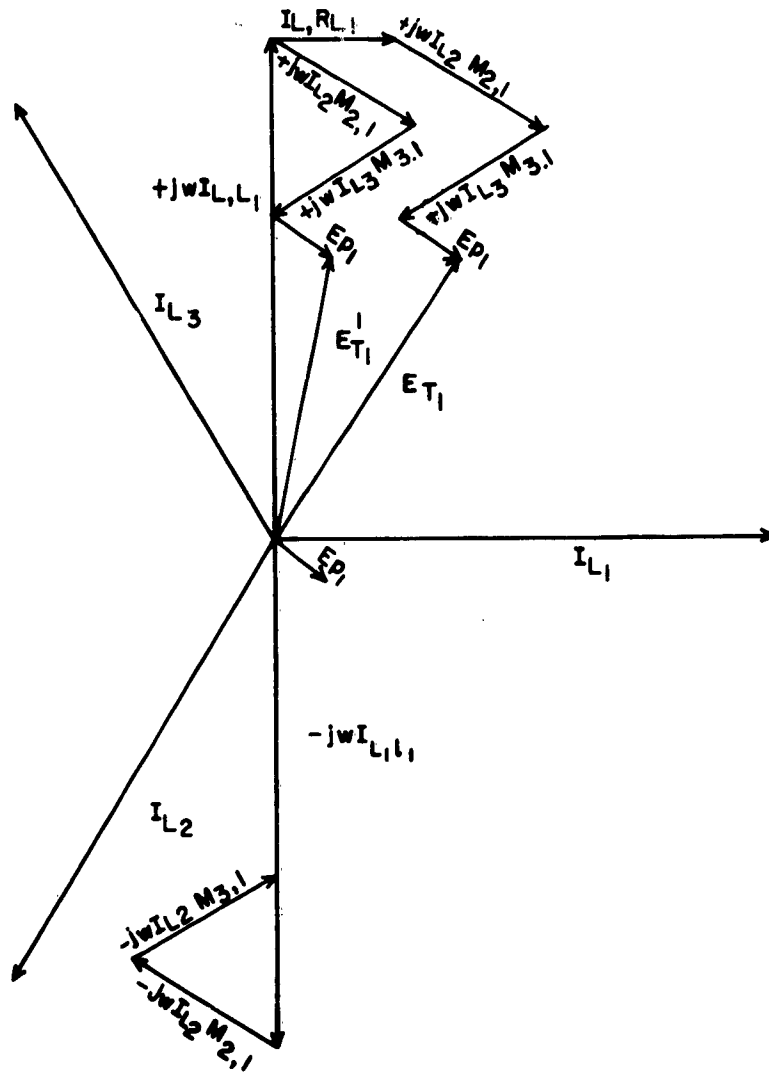


Figure 29. Phasor Diagram - Phase I of Power Monitor Matrix

and by the addition of the synthesized $-j\omega e_{x1}$, only $e_{gr} + j e_{gx}$ remain.

A phasor diagram of the monitoring system is shown in Figure 29. Note that an arbitrary direction and magnitude is given for the extracted voltage component, which is not necessarily that actually obtained.

6.5.3 Construction

The voltage components proportional to phase current, $-j\omega I_L L$ or $-j\omega I_L M$ were derived from current transformers of 100:1 ratio with 1.00 ohm resistors across the output terminals, thus measuring the current of each phase. This voltage component was then given a 90 degree lagging phase shift and a gain adjustment to provide a multiplicable factor proportional to ωL or ωM when the nulling procedure was performed. The voltage component E_{T1} developed across the tertiary winding was placed across a cathode follower with a high input impedance (approximately 10 megohms). An output voltage exactly 10^{-3} times the input was obtained through a preset gain control. This allowed a convenient reference for quantitative measurements of null displacements due to extracted voltage components which would then be 10^{-3} times the actual voltage.

6.5.4 Adjustment

The adjustment procedure consists of energizing one phase winding at a time and adjusting the phasing and gain controls for that phase until an output null is obtained. This procedure is repeated as the second and third phase winding are energized in turns.

6.6 Field Strength Measurements

Figure 30 is a graph of measured magnetic field strength in gauss along the coil/test section as a function of distance along the major axis. The magnetic probe used for these measurements was a 10 turn coil 0.5 inch diameter oriented

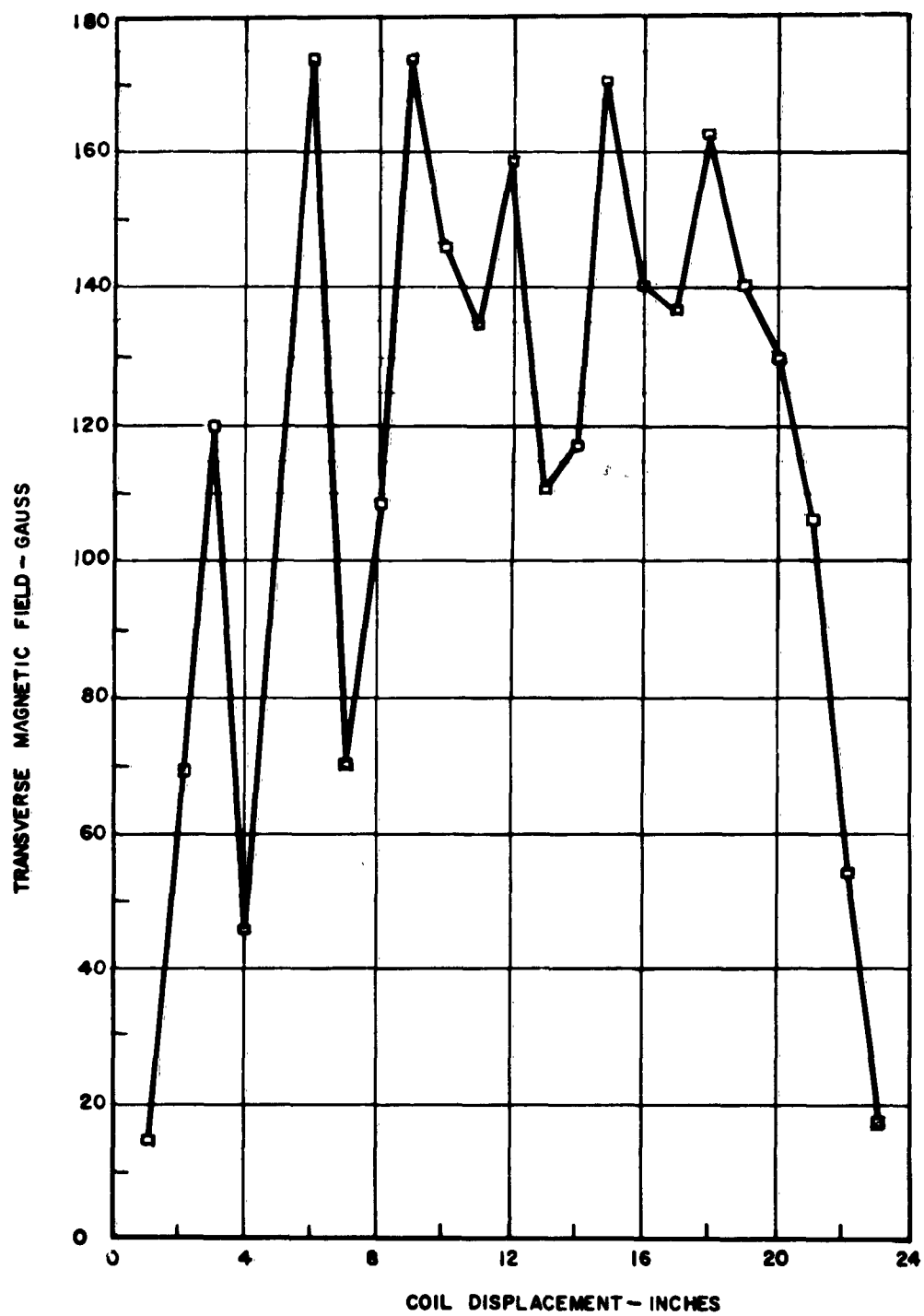


Figure 30. Field Strength Measurements Along Interaction Channel

such that its axis was normal to the plane of the coil. Using the expression

$$B = e \left(\frac{\sqrt{2}}{n \omega A} \times 10^4 \right) \text{ gauss}$$

Field strength normal to the axis as a function of probe voltage was calculated at 5.04×10^2 gauss/volts RMS at a frequency of 3066 cps. Considering that a traveling field is obtained, a forward traveling field strength of 157 gauss (typical) at the center of the channel is calculated. It should be noted that the three-phase currents are not equal, being 157 amps, 85 amps, and 150 amps for phases I, II and III respectively. This is the principal cause of the space variations in field strength. Note also that the method of measurement does not measure the field components parallel to the axis. These are not negligible since the distance between top and bottom coil sections is not small compared to a one-half space wavelength. Because of this and departures from non-ideal conditions, the deviation from the calculated field strength of 2.36 gauss/ampere RMS (see Appendix I) results.

The direction of the forward magnetic field cannot be obtained from the field strength plot. A linear form of a drag cup was made from a small piece of folded aluminum foil which was placed between the excited coils and the direction of movement noted.

7. EXPERIMENTAL RESULTS

7.1 Introduction

A total of 15 test runs were completed during the experimental program. The initial four tests did not include complete instrumentation but were useful in obtaining information relative to the overall performance of the plasma arc torch and complete system. The next six runs were conducted on the basis of an anticipated power flow in excess of 100 watts, assuming a field strength of 1000 to 1200 gauss and a reasonable conductivity of 100 mhos per meter. While electrical measurements could not be achieved during these runs, an extracted power of 860 watts was inferred from the aerodynamic measurements using the assumed values of field strength and conductivity. Since it was known that the electrical measuring system would readily detect this level of power flow, the field strength and conductivity values were very suspect. When the field strength measurement was repeated, the correct value of 160 gauss was obtained. It then became obvious that further consideration would be required of the electrical instrumentation system. At the new level of expected power, noise from many parts of the system was found to interfere with the measurements of power flow between the plasma and the travelling field system. Corrective measures were taken to overcome this difficulty and are outlined briefly in the next section. After completion of these changes to the system, five additional test runs were performed. The first two of these tests were made using single phase operation, and the latter three were performed with normal three phase excitation.

7.2 Modification of Electrical Instrumentation

Electrical measurement techniques as originally developed have been

described in section 6.2.1. Due to the necessity for measuring a lower power level than originally expected, several changes were made in the instrumentation. One technique considered used the correlation resulting from the utilization of an XY scope, with a 3000 cycle sine wave applied to one input and the output from the phase nulling circuit to the other input. With proper calibration, this technique should enable the measurement of magnitude and phase of the generated voltage. This approach was found to be not sufficiently sensitive for the necessary tests due to low frequency modulation which caused some distortion of the wave form.

Considerable effort was then expended to determine all sources of noise in the system and take corrective measures to eliminate them. Over the course of experimentation, four primary sources of noise were detected: 1) Amplitude modulation of the high frequency alternator outputs, 2) Phase modulation of the alternator outputs, 3) Induced voltages in connecting leads between current transformer and metering equipment due to mechanical vibration in the vicinity of the field coils, and 4) Amplifier noise. It was established that the modulation effects were of the order of 1% and that they were inherent in the design and construction of the alternators. The field behavior was checked by using batteries in place of rectifier power supplies, but no desirable change occurred in the alternator output when this substitution was made. No reduction of the first two noise effects was therefore able to be accomplished. It was, however, possible to overcome the noise from the remaining two sources quite effectively. This resulted in a noticeable increase in sensitivity, although the XY scope technique was still not satisfactory due to the low frequency modulation

components in the output of the alternators. Therefore, the following changes were made to enable a measurement of power output:

- a) The voltage signal used in the phase nulling circuit which was a function of the circulating current was increased appreciably. This enabled the utilization of the full voltage output from the tertiary winding and avoided operating at a low signal level where noise was more serious.
- b) A wattmeter measurement was employed utilizing the null voltage and the current output from an additional current transformer. Calibration of this meter was made by various levels of absorbed power in the test channel.
- c) Phase shift detection of the generated voltage signal was read on a phasemeter. In order to minimize noise interference from this reading, an integrated voltage output from the meter was also measured.

When these above changes were made in the instrumentation circuitry, the data obtained from a typical test run consisted of the following measurements:

- (1) Power reading on wattmeter.
- (2) Change in magnitude of null voltage.
- (3) Phase shift of null voltage.
- (4) Integrated voltage output for the phase shift.

Five test runs were then performed with this instrumentation system. In the three phase runs, the system was connected into Phase II.

The circuit diagram for the final instrumentation system is shown in Figure 31. The vector diagrams for the voltages and currents of interest are shown in Figure 32. The magnitudes of these vectors are not scaled, but are used to indicate the proper direction of power flow which was obtained by inserting absorbing load into the test channel and by operating the plasma arc torch with a slip of -3 with respect to the phase velocity of the travelling magnetic field. Records were obtained for the data during the test runs by two 16 mm movie cameras. One camera recorded all electrical measurements and the other covered the pressure readings used for the aerodynamic measurements.

7.3 Electrical Results

The electrical measurements obtained on film are plotted as a function of time in Figures 33 and 34 for two of the test runs. This includes the power from the test generator, phase angle between E_N and I_ϕ , and the magnitude of null voltage, (E_N). Also plotted is the power into the plasma arc torch during the run.

The readings for power output indicate the level of power which was extracted by the interaction of the magnetic field and the plasma. From the vector diagrams shown in Figure 32, one can obtain the explanation for the power change for generated power and absorbed power cases. From the diagram, a change in phase and amplitude of E_N is indicated. This change shows a generated voltage in the tertiary winding and when it is transposed as a change in the primary circuit (E_G and I_G), the direction indicates the change in power supplied to the circuit. For the absorbed power case, additional power is indicated and for the generated case, a reduction in power supplied is indicated.

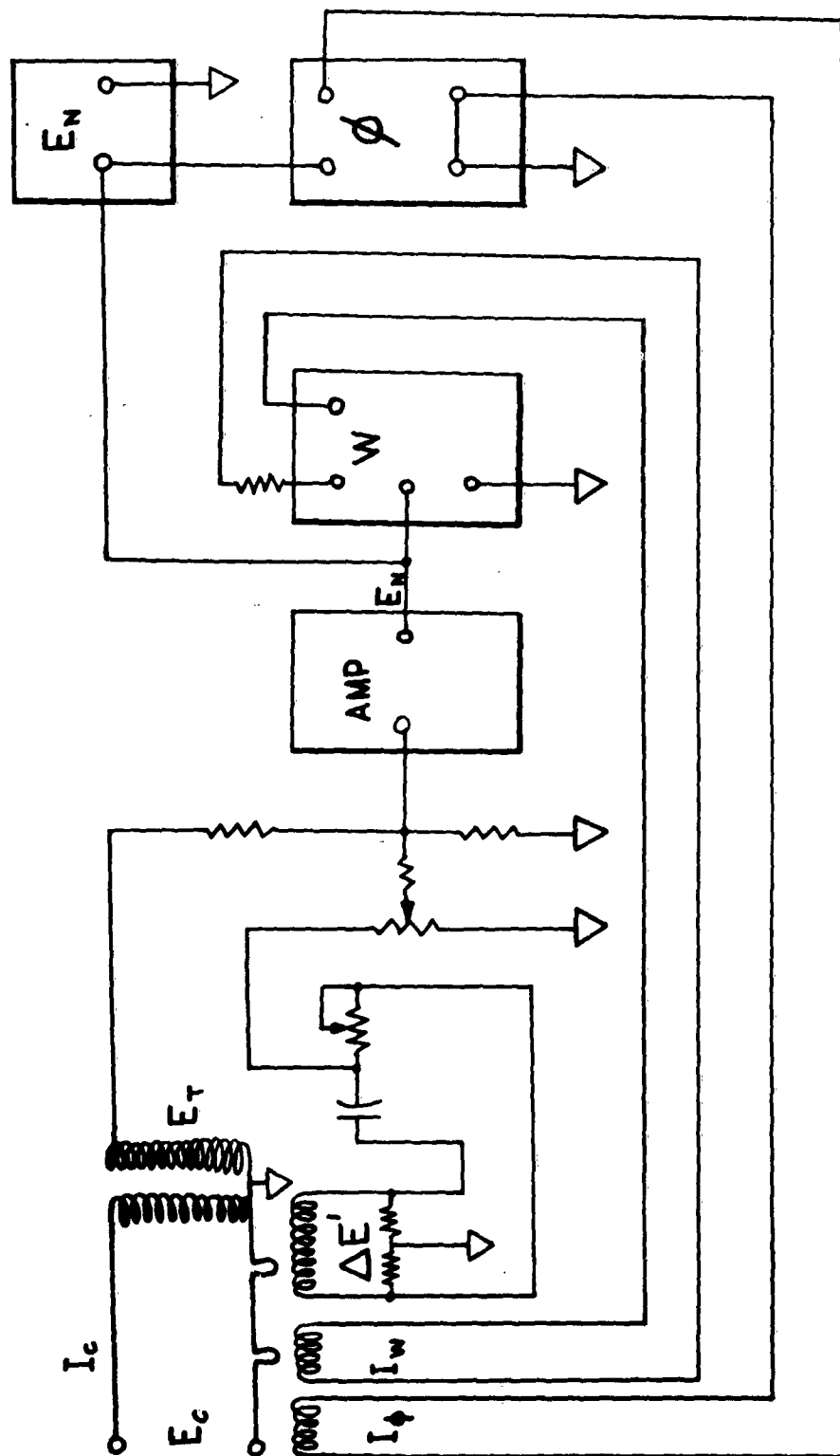


Figure 31. Circuit Diagram Final Instrumentation System

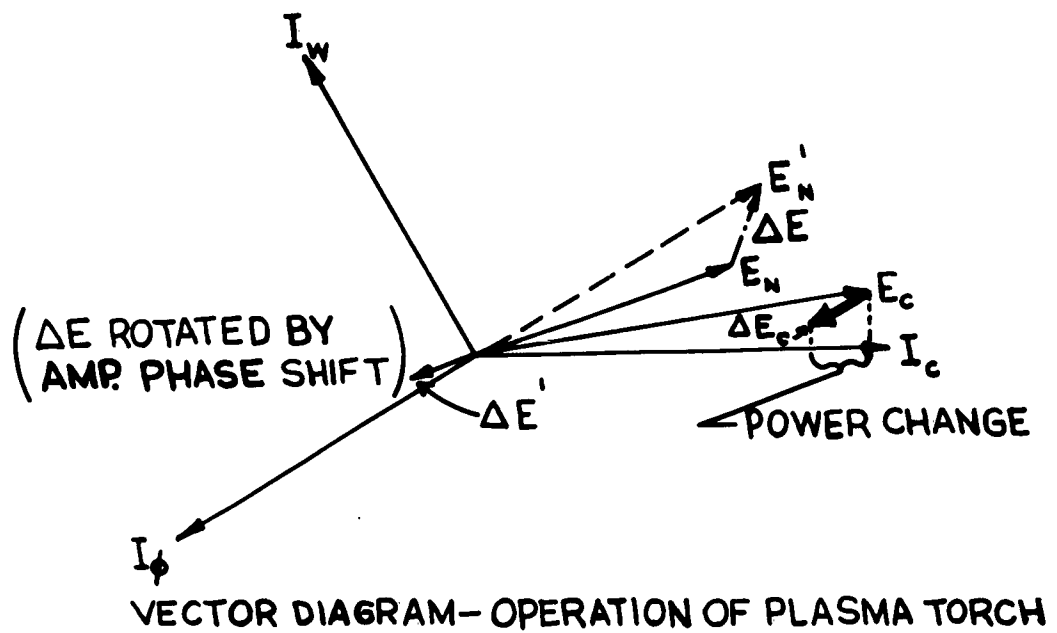
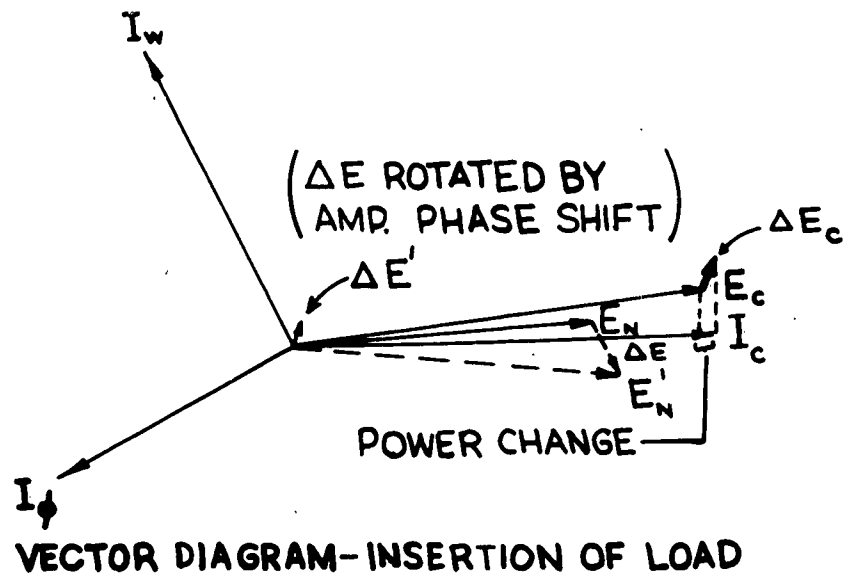


Figure 32. Vector Diagrams - Voltage and Current

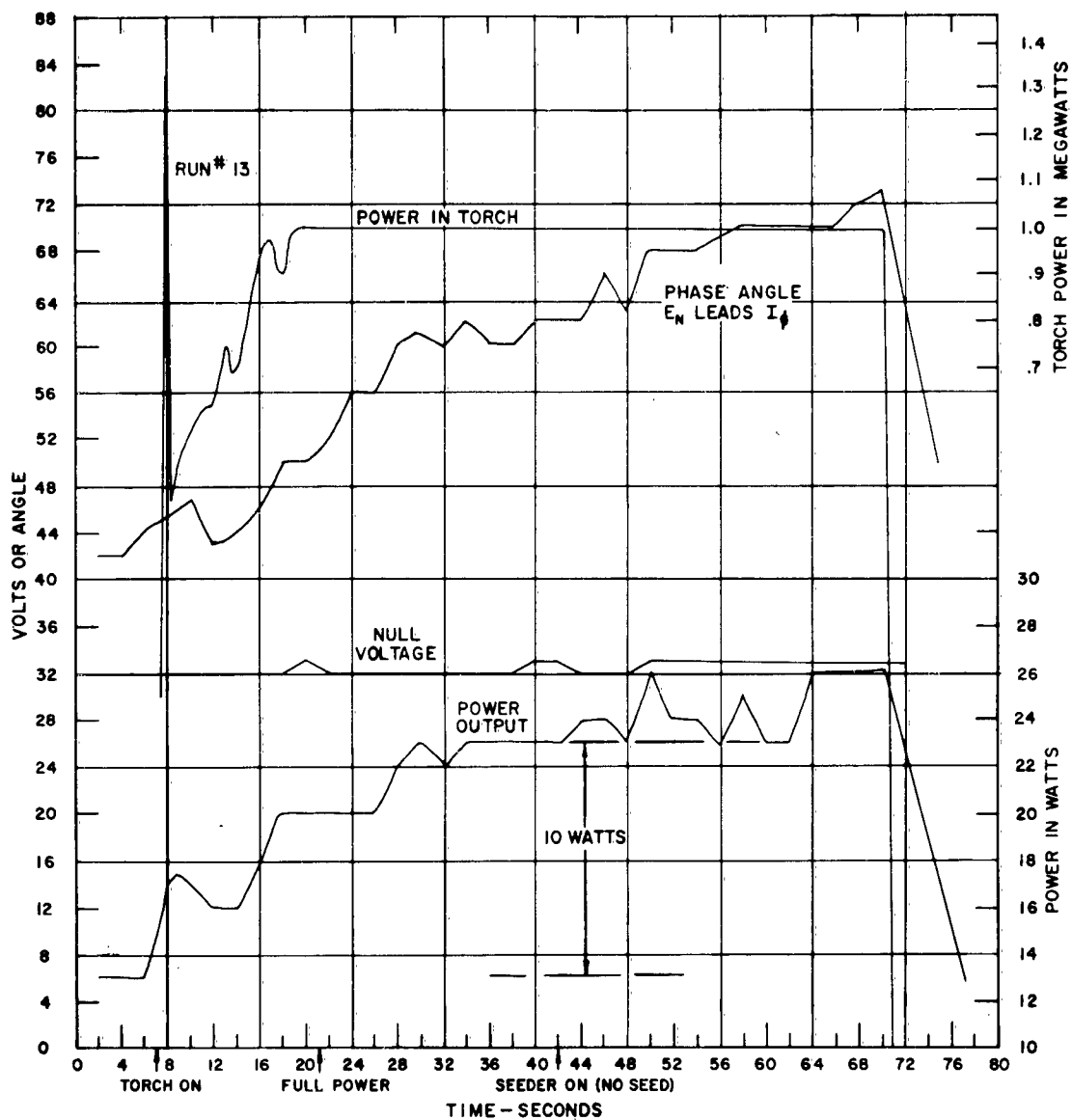


Figure 33. Electrical Measurements From Motion Picture Film Data - Run #13

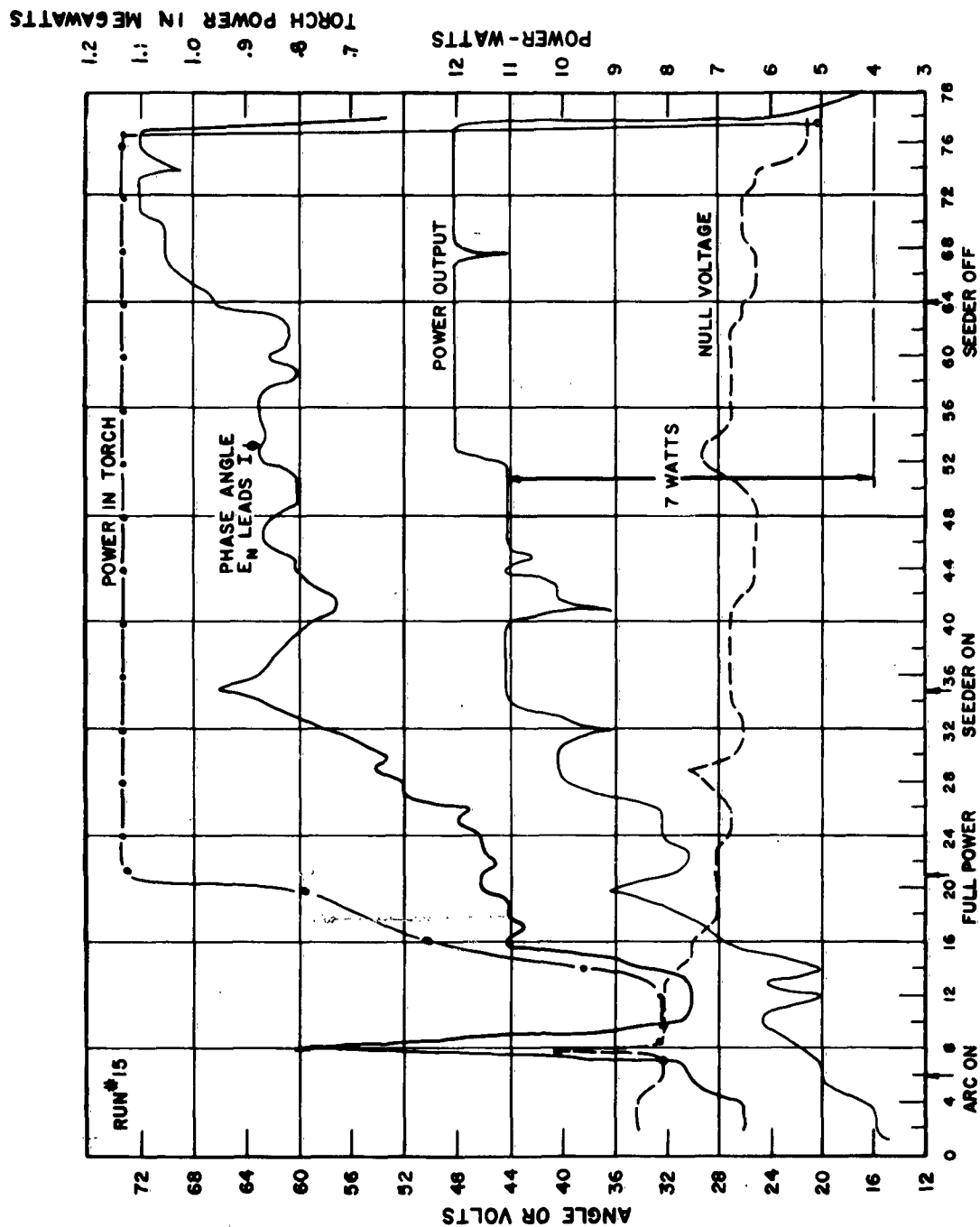


Figure 34. Electrical Measurements From Motion Picture Film Data - Run #15

The magnitude of power generated by the plasma is indicated to be between 7 and 10 watts. This value corresponds closely to the calibration of the wattmeter performed by the insertion of load into the channel. The value also correlates closely with the power which is expected by theoretical considerations employing Equation (3.31) of Part I (Theoretical Analysis). When the magnetic field strength of 160 gauss is used in calculations for generated power, a conductivity would be required in the order of 30 mhos per meter. This figure appears to be slightly high when considering the evidence obtained during the tests which indicated practically no effect from the seeder. However, the results obtained from these tests have been quite repeatable and should be considered as a reliable check on the theoretical calculations.

The experimental results obtained in later test runs were reduced from the instrumentation filmed during operation. Two typical sequences are shown by the photographs in Figure 35.

7.4 Aerodynamic Results

Pressure measurements for runs No. 13 and 14 are shown in Figures 36 and 37 respectively. For run No. 13, the ratio of static pressure at the test section entrance to total (or plenum) pressure decreased from 0.23 to 0.14 during the time for which pressure data were recorded. For isentropic flow of air (considered as an ideal gas) this would correspond to an average Mach number of 1.76.

Real gas effects have little influence, in the present case, in altering ($M_{T.S. \text{ entrance}}$) since the compressibility factor is only slightly greater than unity; this was also pointed out in Section 3.2.3. As is suggested by Figure 13, heat losses to the nozzle walls would tend to reduce the velocity at the exit of the nozzle; but then, the velocity of sound will also decrease, thus suggesting that the Mach number at the exit of the nozzle (or the entrance to the test

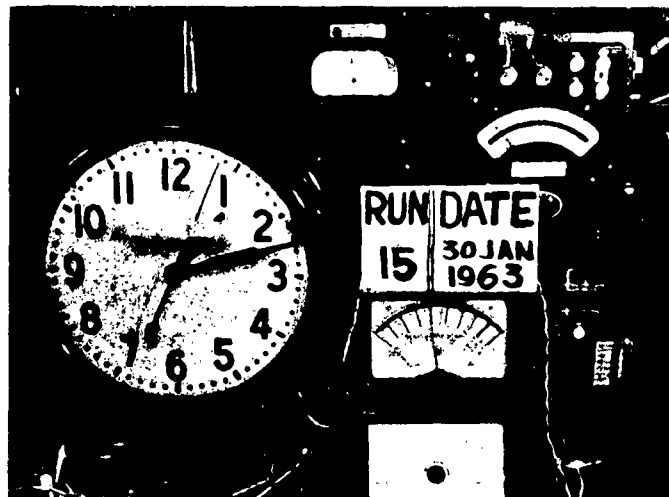
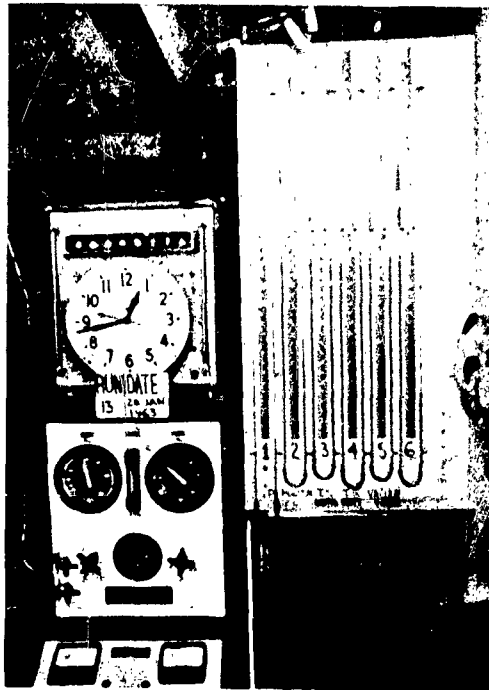


Figure 35. Typical 16mm Motion Picture - Recorded Test Data 93

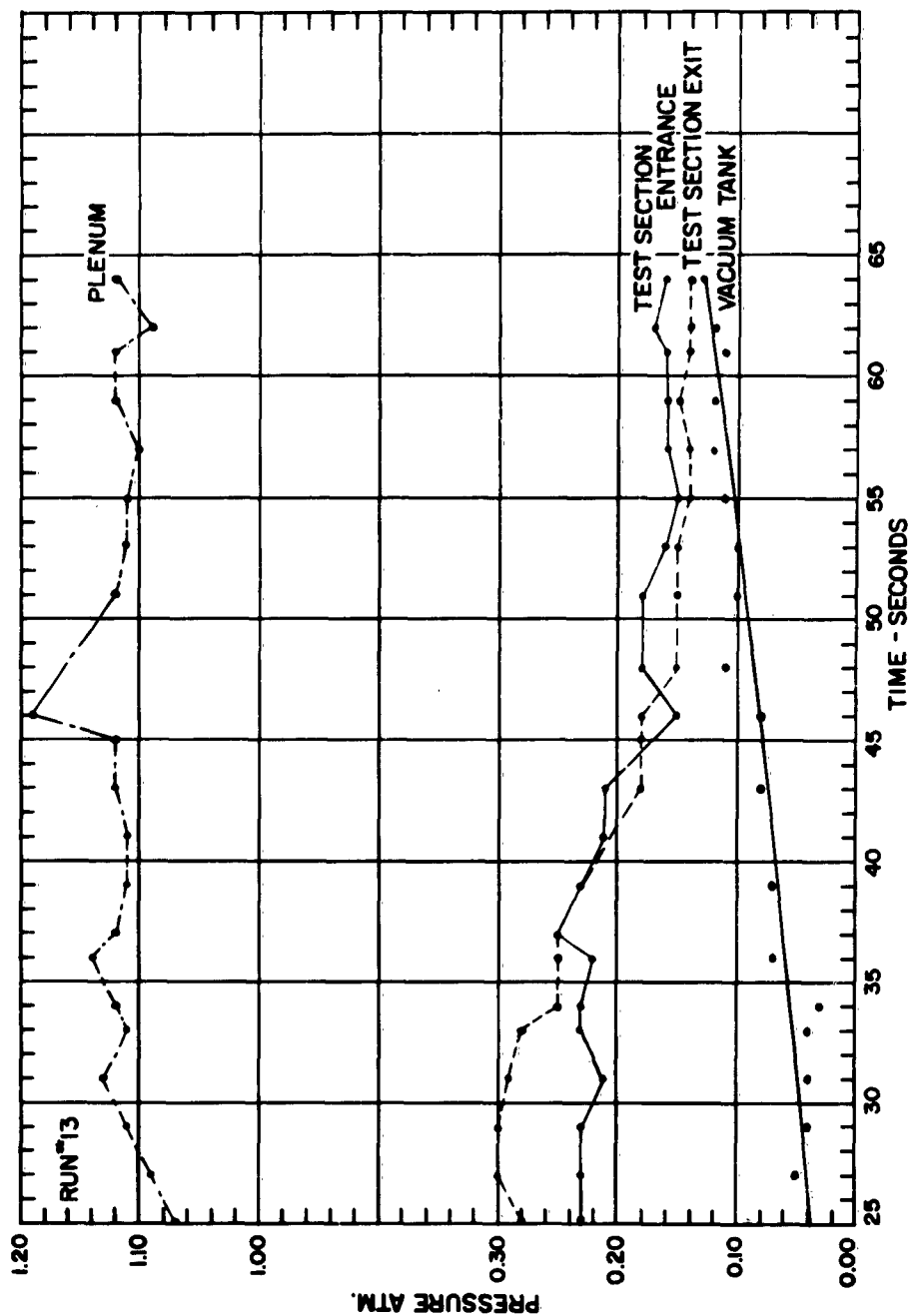


Figure 36. Aerodynamic Measurements From Motion Picture Film Data - Run #13

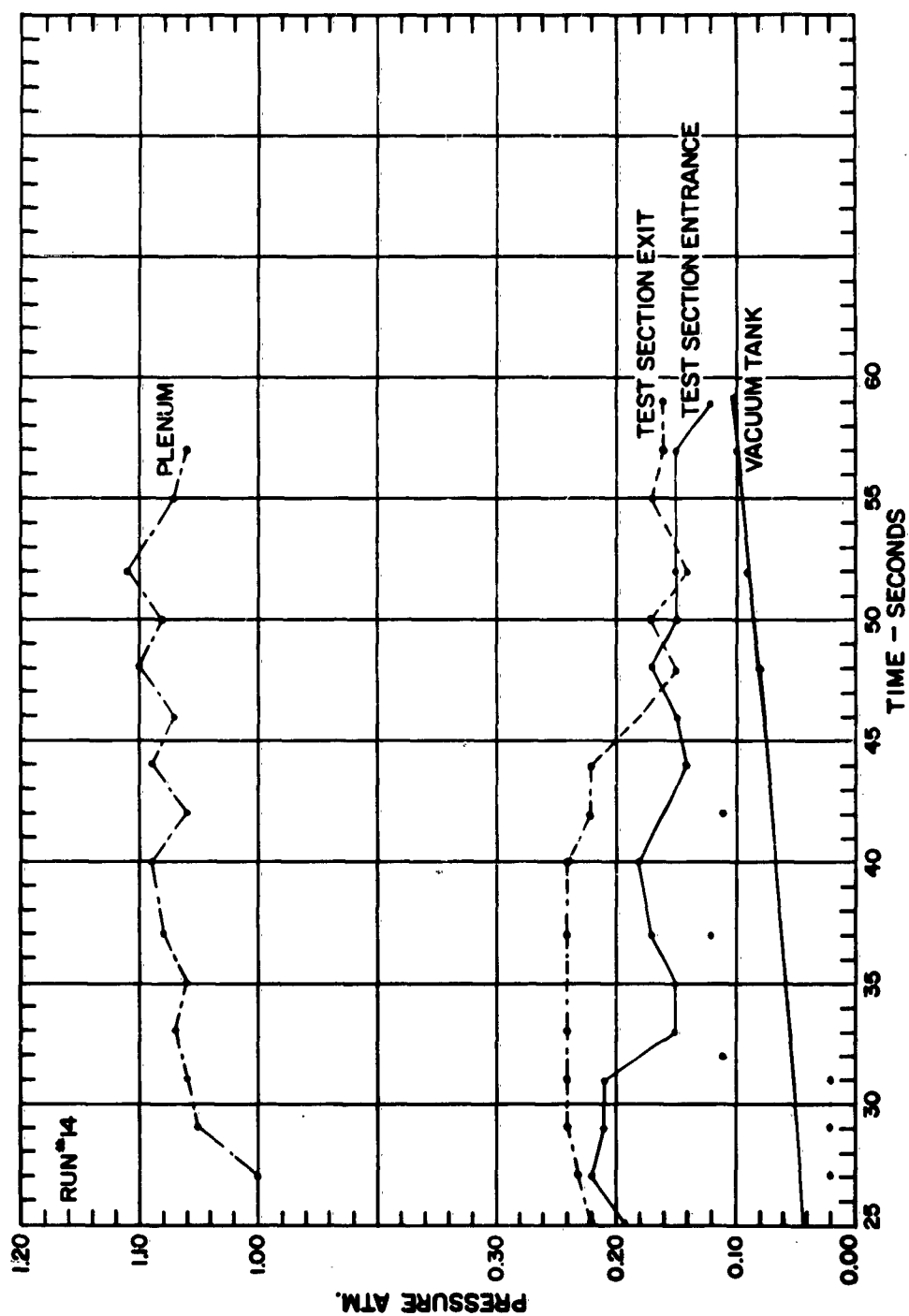


Figure 37. Aerodynamic Measurements from Motion Picture Film Data - Run #14

section) is not very sensitive to heat losses. Thus, although a precise value for ($M_{T.S.}$ entrance) cannot be deduced from the data shown in Figure 36, it is felt quite certain that the supersonic flow which was established during the run had a Mach number at the exit of the nozzle which was not too far off the design value of 1.53.

Static-pressure ratio across a normal shock at $M = 1.53$ is (Reference 4) $P_2/P_1 = 2.564$. Had a normal shock existed anywhere in the test section, the pressure at the exit of the test section would have been $2.564 \times .2$ atm., or approximately half an atmosphere. Since the measured pressure at the exit of the test section is much less than that value (see Figure 36) it is concluded that the test section was shock-free, at least during the interval shown in that figure.

The fact that the static pressure at the exit of the test section was higher than at the entrance during part of the runs (see Figures 36 and 37) indicates that part of the kinetic energy of the plasma was converted to increase static pressure along the test section. Hence, in order to maintain constant velocity flow in the test section, as is desired (on theoretical grounds) in the present case, it will be necessary to increase the ratio of exit-to-entrance cross-sectional area of future test sections beyond the value of 1.3 previously chosen (see Section 3.3).

An estimate of the total enthalpy of the plasma for a typical run (at which time a steady state was reached) can be obtained from an overall energy balance measurement as follows:

Measured power input to arc:

$$680 \text{ volts} \times 1960 \text{ amp} = 1.33 \text{ MW}$$

Heat absorbed by cooling water:

circulating water mass flow rate = 45 lb_m/sec

temperature difference between outlet and inlet = 15.4°F

$$\begin{aligned}\text{heat absorbed by water } 45 \times 15.4 &= 694 \frac{\text{BTU}}{\text{sec}} \times \frac{1.054 \text{ KW}}{\text{BTU/sec}} \\ &= 730 \text{ KW} = .73 \text{ MW}\end{aligned}$$

Stagnation enthalpy

measured mass flow of air = .225 lb_m/sec

$$\begin{aligned}\text{enthalpy added to flow} &= \frac{(1.33 - .73) \text{ MW}}{.225 \text{ lb}_m/\text{sec}} \times \frac{(948 \frac{\text{BTU}}{\text{lb}_m}) (1 \frac{\text{lb}_m}{\text{sec}})}{(1 \text{ MW})} \\ &= 2525 \text{ BTU/lb}_m\end{aligned}$$

hence, stagnation enthalpy = 2525 + 125 = 2650 BTU/lb_m (compare with the design value of 2925 BTU/lb_m, see Table II).

From the above data, the overall efficiency of the arc as a converter of electrical power input to heat energy added to the flow of air is

$$\text{arc efficiency} = \frac{1.33 - .73}{1.33} \times 100 = 45\%$$

8. CONCLUDING REMARKS

The following observations may be made based on the experimental program described in this report:

- a) A measurement of extracted power has been made from the test generator which agrees quite well with the predicted values from a theoretical investigation.
- b) An improved seeding technique is necessary to increase the conductivity to an expected magnitude of 100 mhos per meter.
- c) The magnetic field strength for the generator was considerably lower than desired due to excessive loss in core material.
- d) The results of this program are very encouraging when considering the region of operation. The feasibility of AC power extraction has been indicated from the interaction of a flowing plasma in a travelling magnetic field. It should be definitely possible to obtain useful electrical power by an increase in scaling of a generator which would give much higher values for the important parameters such as magnetic field and conductivity.

9. RECOMMENDATIONS

The following recommendations are presented for continuation of an experimental and analytical program:

- a) Continued experimental investigation is required to fully explore the inter-related parameters which affect operation.
- b) Efforts are necessary to increase magnetic field strength and improve seeding techniques during future experimental tests.

- c) Further experimental work is indicated, to more fully define a number of investigative areas such as heat protection of the generator walls by transpiration cooling techniques, the use of shading magnetic fields to decrease fringing losses, heat transfer to the walls and viscous effects in the gas, and other related considerations described in Part I of this report.
- d) An experimental program should be undertaken which would investigate the feasibility of superconductivity to power extraction coil system. Such a program would employ the existing model facility.
- e) Consideration should be given to the investigation of non-equilibrium techniques to increase the conductivity of the plasma.
- f) Consideration should be given to the substitution of liquid metal in place of a gaseous plasma as the moving conductive material. This could result in an increase in conductivity by orders of magnitude, but the velocity would of course be decreased considerably.

APPENDIX I

Calculations of theoretical coil field strength per ampere of excitation current:

The following assumptions are made:

1. The permeability of the ferromagnetic substrate is infinite.
2. All flux passes in lines normal to the substrate from pole to pole (i.e. no leakage flux).

From elementary considerations

$$L = \frac{n\phi}{I} \quad (\text{henrys, webers, amperes})$$

for an air gap of length

$$B = \frac{\mu_0 nI}{l}$$

and for a pole of area A

$$\phi = BA = \frac{\mu_0 nI A}{l}$$

which gives

$$\frac{B}{I} = 4\pi \frac{n}{l} \times 10^{-3} \quad \text{gauss/ampere}$$

for the coil under consideration

$$l = 2.5" = 0.0636$$

$$n = 6$$

$$\frac{B}{I} = 1.18 \text{ gauss/ampere/phase}$$

$$= (1.18)(1.14) = 1.35 \text{ peak gauss/ampere rms/phase}$$

$$= (1.35)(1.73) = \underline{2.36} \text{ peak gauss/ampere rms}$$

in a three-phase balanced system.

REFERENCES

1. "Electrodeless MHD Generator Research" Technical Documentary Report ASD-TDR-62-411, Part I, Flight Accessories Laboratory Wright-Patterson Air Force Base, Dayton, Ohio, March 1962.
2. Rosa, R. J. and Kantrowitz, A. R.: "Magnetohydrodynamic Energy Conversion Techniques" AVCO Research Lab, Research Report 86 April, 1959.
3. Shapiro, Ascher H.: "The Dynamics and Thermodynamics of Compressible Fluid Flow" The Roland Press Co., 1953.
4. Ames Research Staff: "Equations, Tables, and Charts for Compressible Flow" NACA Report 1135, 1953.
5. Low, George M: "Simplified Method for Calculation of Compressible Laminar Boundary Layer with Arbitrary Free-Stream Pressure Gradient" NACA TN 2531, October 1951.
6. Moeckel, W.E., and Weston, Kenneth C.: "Composition and Thermodynamic Properties of Air in Chemical Equilibrium" NACA TN 4265.
7. Moeckel, W. E.: "Oblique-Shock Relations at Hypersonic Speeds for Air in Chemical Equilibrium" NACA TN 3895, January 1957.
8. Chapman, Dean R., and Rubesin, Morris W.: "Temperature and Velocity Profiles in the Compressible Laminar Boundary Layer with Arbitrary Distribution of Surface Temperature" Jour. Aero, Sci., Vol. 16, No. 9, September 1949, pp. 547-565.
9. Hansen, Frederick C.; "Approximations for the Thermodynamic and Transport Properties of High-Temperature Air" NASA TR R-50, 1959.
10. Schlichting, H.: "Boundary Layer Theory" McGraw-Hill Book Co., 1955.

11. Breene, R. G., et al: "Electromagnetic Effects Associated with Hypersonic Vehicles" Aerosciences Lab., G.E. Co. Philadelphia, May 15, 1959.
12. Churchill, R.V.: "Modern Operational Mathematics in Engineering" McGraw-Hill Book Co., 1944.
13. Fused Quartz Catalog, G.E.Co., Willoughby, Ohio
14. Fay, J.A., and Riddell, F.R.: "Theory of Stagnation Point Heat Transfer in Dissociated Air" Jour. Aero/Space Sci., Vol. 25, No. 2, Feb. 1958.
15. Li, Ting-Yi, and Geiger, Richard E.: "Stagnation Point of a Blunt Body in Hypersonic Flow" Jour. Aero. Sci., Vol. 24, No. 1, January 1957.
16. Donaldson, D. DuP. (Private communication).
17. Handbook of Chemistry and Physics, Chemical Rubber Publishing Co., 38th Edition, 1956-7.
18. Ness, Nathan, and Fanucci, Jerome B.: "An Analytical Solution for the Electron Density of High Temperature Equilibrium Air" Physics Technical Memo. No. 6, RCA Moorestown, N.J., June 27, 1960.

SYMBOLS

A	Area
a	Velocity of sound.
B _f	Forward traveling magnetic wave
B _{Max}	Magnetic field of peak
B _{Min}	Magnetic field of minimum
B _r	Reverse traveling magnetic wave
C	Defined by Equation (3.9)
C _i	Mass fraction of specie (i)
C _p	Specific heat
e	Voltage
E _p	Complex voltage component due to plasma motion and conductivity.
E _T	Complex terminal voltage of excitation coil per phase
E _{T'}	Complex terminal voltage of current-free coil per phase
f	Frequency (sec ⁻¹)
g	Gravitational acceleration
h	Enthalpy; also heat transfer coefficient
h _D	Defined by Equation (6.4)
h _i [°]	Heat of formation of atoms of specie (i)
j	Conversion factor $j = 778 \frac{\text{ft-lb}}{\text{BTU}}$; also $\sqrt{-1}$
k	Diffusivity of solid material Equation (3.20)
L	Inductance
LE [#]	Lewis number
M	Mach number

M_{AB} Mutual inductance from phase A to phase B.

\dot{m} Mass flow rate

N Number of turns

P Pressure, also power

Pr^* Prandtl number

q Heat transfer rate

R Radius of curvature of stagnation point;
also universal gas constant

r Radius of cylindrically shaped calorimeter

R_e Real part of

R_g Resistance due to plasma motion and conductivity per phase

R_L Resistance of load per phase

S Distance along a generator of an axi-symmetric body.

S Sutherland's constant $S = 198.6^\circ R$; also entropy; also standing
wave ratio.

T Temperature

t Time

u Velocity

x Distance along centerline

X_g Reactance due to plasma motion and conductivity per phase

X_L Reactance of load per phase

Z Compressibility factor.

Z_L Complex impedance of load per phase

Z_p Complex impedance due to plasma motion and conductivity
per phase

γ Ratio of specific heats

δ Boundary layer thickness

δ^* Boundary layer displacement thickness

ϵ See equation (3.20)

θ Inclination of velocity vector to x-axis

λ Thermal conductivity

μ Viscosity (Section 6.3)

μ Mach angle (Section 3.2)

ν Prandtl Meyer angle;
also kinematic viscosity

ρ Density

τ Length of cylindrically shaped calorimeter

Φ Defined in connection with Equation (6.3)

ϕ Defined by Equations (3.6) and (3.7) ; also magnetic field
strength-gauss

ω $2\pi f$ (angular velocity, rad-sec^{-1})

I_c	Circulating current in primary field coil.
I_w	Current component derived from C.T. to drive wattmeter current coil.
I_ϕ	Voltage component derived from C.T. to drive phasemeter.
E_c	Voltage across primary field coil.
E_N	Amplifier output obtained from nulling circuit.
ΔE	Change in E_N due to plasma or load.
E_N'	New value of E_N due to plasma or load.
$\Delta E'$	ΔE rotated by amplifier phase shift.
ΔE_c	Effective change in primary field coil voltage due to plasma or load.

NOTE: All symbols above are in reference to Figure 32.

Subscripts

- C Pertaining to calorimeter material
- e Pertaining to conditions at the outer edge of the boundary layer.
- exit Pertaining to conditions at the exit of the nozzle.
- S Evaluated at the stagnation point.
- (t) or (total) Pertaining to the stagnation value.
- w Pertaining to conditions at the wall.
- 1 Upstream of normal shock.
- 2 Downstream of normal shock.
- ∞ Pertaining to free-stream conditions, ahead of detached shock.

Superscripts

- * Pertaining to conditions at the throat.

**TABLE I: COORDINATES OF SUPERSONIC
PART OF NOZZLE (INCHES)**

X	±Y	X	±Y
0.000	1.010	1.800	1.205
0.100	1.013	1.900	1.215
0.200	1.019	2.000	1.225
0.300	1.026	2.100	1.234
0.400	1.035	2.200	1.242
0.500	1.045	2.300	1.250
0.600	1.056	2.400	1.258
0.700	1.068	2.500	1.264
0.800	1.080	2.600	1.271
0.900	1.093	2.700	1.277
1.000	1.106	2.800	1.282
1.100	1.119	2.900	1.287
1.200	1.133	3.000	1.291
1.300	1.146	3.100	1.295
1.400	1.158	3.200	1.299
1.500	1.171	3.300	1.302
1.600	1.182	3.400	1.305
1.700	1.194	3.418	1.306

- Notes:**
- (i) Nozzle throat is at $X = 0$.
 - (ii) Nozzle exit is at $X = 3.418$.
 - (iii) Y = distance from ϕ to wall.

Aeronautical Systems Division, Dir/Aeronautics, Flight Accessories Lab, Wright-Patterson AFB, Ohio.
 Rept No. ASD-TDR-62-411, Pt II. ELECTRODELESS MHD GENERATOR RESEARCH: Laboratory Facility and Experimental Results. Final report, Mar. 63, 109p. incl illus. tables, 18 refs.
 Unclassified Report

The problem was to experimentally determine the feasibility of AC Electrodeless Magneto-hydrodynamic Power Generation, utilizing a model generator. The analysis, development, and test model operation involved the design, construction, and testing of the component units which comprise the plasma arc lab

(over)

facility. This report includes the lab facilities provided for the conduction of the experimental investigation and the design of the generator (resulting from theoretical studies given in Part I) test model, which involved Plenum and Mixing Chamber, Seeder, Supersonic Nozzle, Test Section, Diffuser, Power Extraction Coils, Coil Power Supply, Phase Nulling Network, and other instrumentation. Electrodeless AC MHD power generation has been experimentally observed, and extracted power from the plasma has been recorded during test operation of the model.

1. Electrodeless MHD Generator

- I. AFSC Proj 8173, Task 817306
- II. Contr No. AF 33 (616)-7913
- III. RCA Defense Electronic Products; Missile & Surface Radar Div., Moorestown, N.J.
- IV. Aval fr OTS
- V. In ASTIA collection.

Aeronautical Systems Division, Dir/Aeronautics, Flight Accessories Lab, Wright-Patterson AFB, Ohio.
 Rept No. ASD-TDR-62-411, Pt II. ELECTRODELESS MHD GENERATOR RESEARCH: Laboratory Facility and Experimental Results. Final report, Mar. 63, 109p. incl illus. tables, 18 refs.
 Unclassified Report

The problem was to experimentally determine the feasibility of AC Electrodeless Magneto-hydrodynamic Power Generation, utilizing a model generator. The analysis, development, and test model operation involved the design, construction, and testing of the component units which comprise the plasma arc lab

(over)

facility. This report includes the lab facilities provided for the conduction of the experimental investigation and the design of the generator (resulting from theoretical studies given in Part I) test model, which involved Plenum and Mixing Chamber, Seeder, Supersonic Nozzle, Test Section, Diffuser, Power Extraction Coils, Coil Power Supply, Phase Nulling Network, and other instrumentation. Electrodeless AC MHD power generation has been experimentally observed, and extracted power from the plasma has been recorded during test operation of the model.

1. Electrodeless MHD Generator

- I. AFSC Proj 8173, Task 817306
- II. Contr No. AF 33 (616)-7913
- III. RCA Defense Electronic Products; Missile & Surface Radar Div., Moorestown, N.J.
- IV. Aval fr OTS
- V. In ASTIA collection.